DEVELOPMENT OF CAPACITIVE SENSOR TO DETERMINE VOID FRACTION IN HORIZONTAL AND VERTICAL TUBES

BY

HONGLIANG QIAN

THESIS

Submitted in partial fulfillment of the requirements
for the degree of Master of Science in Mechanical Engineering
in the Graduate College of the
University of Illinois at Urbana-Champaign, 2017

Urbana, Illinois

Adviser:

Professor Predrag S. Hrnjak

ABSTRACT

This study first presents flow regimes and void fraction in horizontal and vertical tubes with R134a in the adiabatic condition and low mass flux range. Visualization results of horizontal flow patterns are compared to Wojtan-Ursenbacher-Thome flow regime map and have a good agreement. Both void fraction results for horizontal and vertical tubes are compared to some widely used correlations. Influences of tube orientation and mass flux on void fraction are discussed. At the same vapor quality condition, void fraction of horizontal tubes is larger than that of vertical tubes. Higher mass flux also results in larger void fraction compared that of lower mass flux.

A new capacitive sensor aimed to measure void fraction is designed and built. With this capacitive sensor, characterizing flow patterns appear in low mass flux range and measuring void fraction for horizontal and vertical tubes can be achieved. Signal characterization for each flow pattern is proposed. To apply this sensor to more applications in HVAC&R systems, electrodes with different axial lengths are built together to be compared. The comparison of signals from them show the signals are independent on axial length. Due to the non-uniformity of the electric field between the electrodes of the sensor, a calibration procedure of void fraction measurement must be finished before utilizations. An experiment based (quick closing valves (QCV)) calibration procedure is conducted. Two calibrated curves for measuring void fraction in horizontal and vertical tubes are proposed. With calibrated curves, sensors with similar configurations can be directly utilized to measure void fraction in further studies.

ACKNOWLEDGMENTS

First of all, my great gratitude goes to my adviser Professor Predrag S. Hrnjak. Without his support, guidance and trust, I cannot have the opportunity to start my research in Air Conditioning and Refrigeration Center (ACRC). His foreseeing insights and earnest research attitude inspire me a lot and encourage me to go further.

I would like to thank my colleagues Huize Li and Jiange Xiao, who gave me the introduction of this researching area and help me with solving many difficulties. Also, I really appreciate Professor Elbel, Professor Wang, Neal Lawrence, Shenghan Jin, Lili Feng, Amir Chavoshi, Xuan Liu, Jun Li, Jingwei Zhu, Houpei Li, Bill Davis, Bruno Yuji Kimura de Carvalho, Abdel Rahman D Khaleel Farraj, Yueming Li, Wenzhe Li, Yu Kang, Cheng-min Yang, Ce Shi and Yingyue Zhang for their research suggestions and help in the lab. They are excellent colleagues as well as friends. It is my pleasure to work with so many outstanding peers in ACRC. I would love also thanks to the sponsors of ACRC for their support and trust of my work.

Also, I want to thank my girlfriend Yufang Yao. Her accompany, help and support encourage me to embrace every single day.

Last but not least, I want to express my deepest gratitude to my parents Feng Qian and Wei Wang. Their unreserved love and unconditional support are always my most reliable backing.

TABLE OF CONTENTS

LIST OF FIGURES

LIST OF TABLES

NOMENCLATURE

A	Cross-sectional area	m^2
C	Capacitive signals	pF
C_0	Distribution parameter	
g	Mass flux	kg/m^2s
gravity	Acceleration of gravity	m/s^2
L	Length	m
M	Refrigeration retention with liquid nitrogen recovery	kg
Q	Volumetric flow rate	m^3/s
S	Slip ratio	
T	Temperature	K
t	Time	s
u	Mean velocity	m/s
U_M	Two-phase mixture velocity	m/s
U_{SG}	Superficial vapor velocity	m/s
U_{SL}	Superficial liquid velocity	m/s
U_{GM}	Drift velocity	
V	Test section volume	m^3
X	Lockhart-Martinelli parameter	
x	Vapor quality	
α	Void fraction	
ρ	Density	kg/m^3
μ	Dynamic viscosity	kg/m s
σ	Surface tension	N/m

Subscripts

$_V$	Vapor phase
$_L$	Liquid phase
$_{NORM}$	Normalized
sat	Saturation

CHAPTER 1 INTRODUCTION

Two-phase flows are widely encountered in practical applications in industry. In air conditioning and refrigeration industry, refrigerant two-phase flows play the crucial role in both components and systems. Flow regime and void fraction are important parameters to characterize two-phase flows, which effect pressure drop, heat transfer coefficient and refrigerant charge quantity.

To characterize two-phase flow patterns and measure void fraction in round tubes with R134a, some methods including optical visualization, photography, X-ray photography and capacitance measurement can be utilized. Optical visualization through transparent wall is intrinsically easy for two-phase flows because of the difference in reflectivity and refractivity for vapor and liquid. High-speed video processing techniques has been used widely by Hurlburt and Newell [1], Scott and Hrnjak [2], Xu and Hrnjak [3] and Li and Hrnjak [4]. Keska et al. [5, 6] suggested that capacitive signals showed very good potential to recognize flow patterns. Some research [7-16] used capacitive method to measure phase percentage or characterize flow patterns. However, their working media were non-refrigerant flows whose electrical properties were quite different from those of refrigerants. And most of the studies focused on measuring volumetric void fraction. However, cross-sectional void fraction is crucial to determine heat transfer coefficient and pressure drop in HVAC applications. In microchannel heat exchangers, for example, local void fraction along the headers will influent refrigerant charge and distribution in heat exchangers. A new capacitive sensor based on the sensor Canière et al. [17] developed are further designed and built to characterized flow patterns and measure void fraction.

Chapter 2 will present void fraction and flow regimes in horizontal and vertical round tubes with R134a in adiabatic conditions and low mass flux range. Several flow patterns observed in this mass flux range will be discussed. The void fraction results are compared with some wide-used correlations and the comparison results are given for both horizontal and vertical flows. In Chapter 3, a capacitive sensor aims to characterize two-phase flow patterns and measure void fraction is designed and built. Due to the difference between electric properties of water-air flows and refrigerant flows, some existed designs which focus on non-refrigerant flows are modified. To apply smaller sensor with shorter axial length, three pairs of electrodes with different axial lengths are built side by side. Singles from these three pairs of electrodes can thus be compared. A

commercially available transmitter which is cheap and easy to use is proposed at last. The capacitive signals are discussed in Chapter 4. The flow patterns and void fraction results are from Chapter 2. The results of characterizing of flow patterns and calibration procedure of measurement of void fraction are discussed. Chapter 5 present the summary of this study and future work.

CHAPTER 2 VOID FRACTION AND FLOW REGIMES IN HORIZONTAL AND VERTICAL ROUND TUBES WITH R134A IN ADIABATIC CONDITIONS AND LOW MASS FLUX RANGE

2.1 Void fraction

Two-phase flows, two phases of one or more substances, are widely encountered in practical applications in industry. For HVAC&R industry, liquid-vapor flow of refrigerant acts the crucial role in both components and systems. Void fraction, which is one of the most important parameters in characterizing two-phase flow of refrigerant has gained wide attention. Two-phase mixture densities, two-phase mixture viscosities and average velocities are all influenced by void fraction. It thus effects models for predicting flow regime transition, pressure drop, heat transfer coefficient and refrigerant charge quantity.

For different applications, various definitions of void fraction regarding to certain geometries are proposed [18]:

1. Local void fraction
2. Chordal void fraction
3. Cross-sectional void fraction
4. Volumetric void fraction

The schematic drawing for each definition is shown in Figure 1.

Local void fraction represents liquid or vapor appears at a point: α_{local}=0 refers liquid and α_{local}=1 refers vapor. It is typically time-averaged and defined as in Equation (1). $P_k(x,y,t)$ shows whether liquid or vapor appears at point (x,y,z) at time t. $P_k(x,y,t)$=0 when liquid appears and $P_k(x,y,t)$=1 when vapor appears.

$$\alpha_{local}(x,y,t) = \frac{1}{t}\int_{t} P_k(x,y,z,t)dt \quad (1)$$

Chordal void fraction is determined in one dimensional geometry like microchannel tubes with two-phase flows inside. Shown in Equation (2), it is defined as the length of vapor (L_V) over the total length (L_V+L_L).

$$\alpha_{chordal} = \frac{L_V}{L_V + L_L} \tag{2}$$

Cross-sectional void fraction is defined as the ratio of cross-sectional area that is occupied by vapor phase to the entire cross-sectional area (shown in Equation (3)). It is crucial for local heat transfer modeling and predictions. This kind of void fraction is typically measured by optical or electrical methods.

$$\alpha_{cross-sectional} = \frac{A_V}{A_V + A_L} \tag{3}$$

Volumetric void fraction is defined in Equation (4). In a container, the ratio of the volume of vapor phase over the total volume of the container. It is usually obtained by quick-closing valves (QCV). By quacking closing valves located at two ends of test section and recovering the two-phase mixture trapped inside, volumetric void fraction can be calculated.

$$\alpha_{volumetric} = \frac{V_V}{V_V + V_L} \tag{4}$$

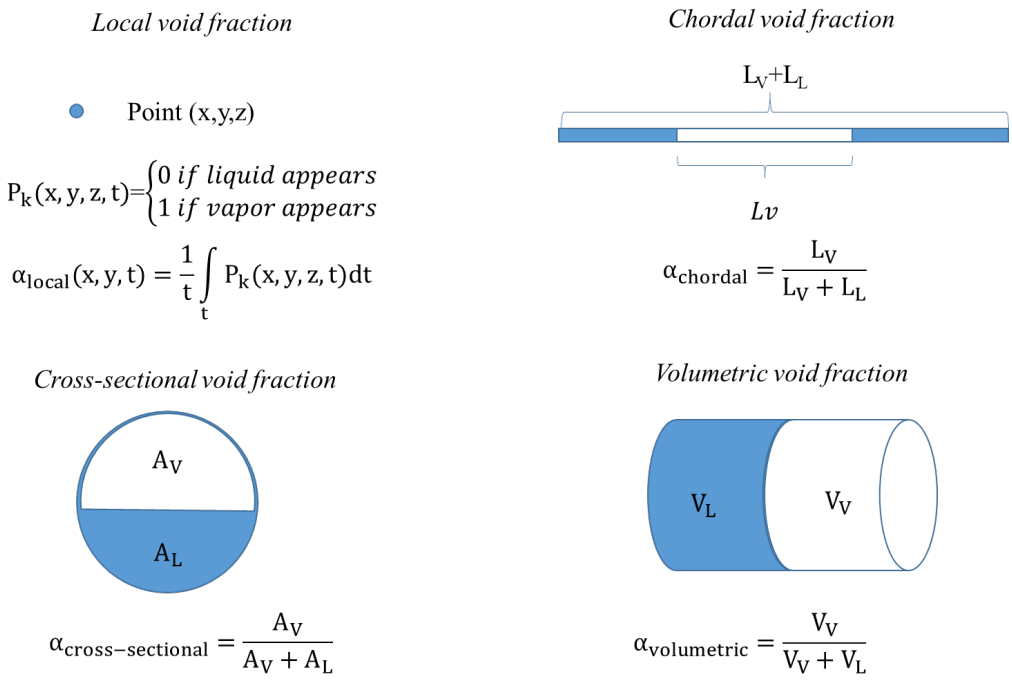

Figure 1 Schematic drawing for each definition of void fraction

Void fraction is different from the vapor quality which is the ratio of weight of vapor phase to total weight of two-phase flow. For a certain mixture of two-phase flow, like refrigerant R134a which is commonly used in HVAC&R applications, the density of vapor phase of R134a is much smaller than that of liquid phase. This results that for very little mass of vapor appears in the tube, void fraction can increase dramatically.

Void fraction is crucial to determine heat transfer coefficient, pressure drop and refrigerant charge in various applications. It is an indispensable parameter for studying two-phase flow not only in tubes, but also in headers which connect adjacent tube passes of a heat exchanger. Local void fraction in a header will determine quality-induced misdistribution, thus influencing the heat transfer performance of a heat exchanger. Flow visualization has been used quantitively to study void fraction in headers and dramatic change of void fraction along the header has been observed [4, 19, 20].

Void fraction correlations are widely used to predict void fraction in certain test conditions. Different types and definitions are discussed in next section.

2.2 Void fraction correlations

Void fraction correlations can be classified into four major categories [21, 22]:

1. Slip ratio correlations
2. $K\alpha_H$ correlations
3. Drift flux correlations
4. General empirical correlations

2.2.1 Slip ratio correlations

Slip ratio is defined as the ratio of mean vapor phase velocity to mean liquid phase velocity:

$$S = \frac{u_V}{u_L} \tag{5}$$

and

$$u_V = \frac{\dot{Q}_V}{A\alpha} = \frac{g}{\rho_V}\left(\frac{x}{\alpha}\right) \tag{6}$$

$$u_L = \frac{\dot{Q}_L}{A(1-\alpha)} = \frac{g}{\rho_L}\left(\frac{1-x}{1-\alpha}\right) \tag{7}$$

where Q is volumetric flow rate, A is the cross-sectional area, g is mass flux and x is vapor quality. Slip ratio correlations is as following:

$$\alpha = \left[1 + \left(\frac{1-x}{x}\right)\left(\frac{\rho_V}{\rho_L}\right)S\right]^{-1} \tag{8}$$

When the slip ratio come to unity, i.e. S=1, the correlation becomes homogeneous void fraction model. It means mean velocity of both vapor phase and liquid phase are equal. They are acting as a homogeneous mixture with the same velocity. Homogeneous model can only predict void fraction in a limited range of situations.

Butterworth [23] indicated a general void fraction correlations in this category is a function of three ratios: liquid quality to vapor quality, vapor phase density to liquid phase density and liquid phase dynamic viscosity to vapor phase viscosity. Equation (9) shows the expression.

$$\alpha = [1 + A\left(\frac{1-x}{x}\right)^{p}\left(\frac{\rho_V}{\rho_L}\right)^{q}(\frac{\mu_L}{\mu_V})^{r}]^{-1} \tag{9}$$

Where A, p, q, and r are constants, which are different for various correlations and models.

2.2.2 $K\alpha_H$ correlations

This category of correlations is a constant or function multiple homogeneous correlation, α_H. Some widely used correlations in this category were proposed by Bankoff [24], Hughmark [25] and Arman [26]-Massena [27].

2.2.3 Drift flux correlations

Zuber and Findlay [28] developed the basics for this approach while other researchers like Ishii [29] helped build this model. Zuber and Findlay [28] indicated void fraction was a function of the distribution parameter C_0 and the drift velocity U_{GM}. The superficial vapor velocity (U_{SG}) and two-phase mixture velocity (U_M) act important parts in this model as well. The general form of correlations of this category is given in Equation (10). Distribution parameter reflects the non-uniformity and drift velocity shows the velocity difference between liquid phase and vapor phase. In addition, this category of correlations shows void fraction is a function of mass flux. Various correlations in this category offer different U_{GM} and C_0.

$$\alpha = \frac{U_{SG}}{C_0 U_M + U_{GM}} = \frac{x}{\rho_V}[C_0\left(\frac{x}{\rho_V} + \frac{1-x}{\rho_L}\right) + \frac{U_{GM}}{g}]^{-1} \tag{10}$$

and

$$U_{SG} = \frac{\dot{Q}_V}{A} = \frac{g}{\rho_V}x \tag{11}$$

$$U_{SL} = \frac{\dot{Q}_L}{A} = \frac{g}{\rho_L}(1-x) \tag{12}$$

$$U_M = U_{SG} + U_{SL} \tag{13}$$

2.2.4 General empirical correlations

Correlations in this category mostly are empirical correlations, which do not belong to the categories mentioned above. Lockhart-Martinelli X parameter [30] which is defined as the ratio of frictional pressure gradient of liquid phase flowing alone along the pipe to vapor phase is an important parameter and X_{tt} is used in some of the correlations. Lockhart-Martinelli X and X_{tt} are shown in Equation (14) and (15).

$$X = \sqrt{\frac{(dP/dz)_l}{(dP/dz)_v}} \tag{14}$$

$$X_{tt} = \left(\frac{1-x}{x}\right)^{0.9} \left(\frac{\rho_V}{\rho_L}\right)^{0.5} \left(\frac{\mu_L}{\mu_V}\right)^{0.1} \tag{15}$$

Woldesemayat and Ghajar [22] compared 68 void fraction correlations for different flow orientations. In addition, Godbole et al. [31] studied 52 correlations in upward vertical two-phase flow. Hence, correlations studied in this project are based on their recommendations. For horizontal flows, Woldesemayat and Ghajar [22] suggested Rouhani I [22, 32], Armand [26]-Massena [27] and the correlation proposed by Woldesemayat and Ghajar [22] performed good predictions. For vertical flows, Woldesemayat and Ghajar [22] recommended Dix [33] and Rouhani I [22, 32] correlations. In addition, Godbole et al. [31] suggested Nicklin et al. [34] had a good performance. For both horizontal and vertical flows, homogeneous correlation is the upper limit of void fraction and added to the plots for comparison. Correlations studied in this project are list in Table 1.

Table 1 Void fraction correlations studied in this project

Reference	Correlation	Category and orientation
Homogeneous	$\alpha_H = [1 + (\frac{1-x}{x})(\frac{\rho_V}{\rho_L})]^{-1}$	Slip ratio, S=1 (H/V)
Armand [26]-Massena [27]	$\alpha = (0.833 + 0.167x)\alpha_H$	$K\alpha_H$ (H)
Nicklin et al. [34]	$\alpha = \frac{U_{SG}}{(C_0 U_M + U_{GM})}$ where $C_0 = 1.2, U_{GM} = 0.35\sqrt{gD}$	Drift flux (V)
Rouhani and Axelsson [22, 32]	$U_{GM} = 1.18(g\sigma\frac{\rho_L - \rho_V}{{\rho_L}^2})^{0.25}$	Drift flux (H/V)
Rouhani I	$C_0 = 1 + 0.2(1-x)$	
Rouhani II	$C_0 = 1 + 0.2(1-x)(gD\frac{{\rho_L}^2}{G^2})^{0.25}$	
Dix [33]	$C_0 = \frac{U_{SG}}{U_{SG}+U_{SL}}\left[1 + \left(\frac{U_{SL}}{U_{SG}}\right)^b\right], \quad b = \left(\frac{\rho_V}{\rho_L}\right)^{0.1}$, $U_{GM} = 2.9\left(g\sigma\frac{\rho_L - \rho_V}{{\rho_L}^2}\right)^{0.25}$	Drift flux (V)
Woldesemayat and Ghajar [22]	$\alpha = U_{SG} / [U_{SG} \cdot \left(1 + \left(U_{SL} / U_{SG}\right)^{(\rho_v/\rho_l)^{0.1}}\right) + 2.9 \cdot \left(gravity \cdot D \cdot \sigma \cdot \left(1 + \cos(\theta)\right) \cdot \left(\frac{\rho_l - \rho_v}{{\rho_l}^2}\right)\right)^{0.25} \cdot \left(1.22 + 1.22 \cdot sin(\theta)\right)^{P_{atm}/P}]$	Drift flux (H)

2.3 Experimental facility

The schematic experimental drawing is shown in Figure 2. Subcooled liquid refrigerant (R134a) is pumped through a mass flow meter with a gear pump into an electric heater where refrigerant is heated into superheated vapor. Refrigerant is mixed in the mixer and the condition of refrigerant is determined by measuring its pressure and temperature. Then superheated vapor refrigerant flows into a pre-cooler whose secondary fluid is water. Water is cooled by building chilling water. With the energy balance of the water side in pre-cooler, the condition of refrigerant after the pre-cooler is determined. The model of pressure transducers is Setra Model 204 and thermocouples are T-type thermocouples. The test section includes between two quick closing valves (ball valves, manually open and close) and a visualization part. Schematic drawing for horizontal and vertical test section is shown in Figure 3. The visualization part is a piece of schedule 80 clear PVC tube with inner diameter of 7 mm. Before the visualization section, 600mm (~86 diameters) of the same PVC tube for the horizontal configuration and 170mm (~25 diameters) for the vertical configuration is utilized to ensure the flow is fully developed. In addition, for the vertical configuration, 460mm of tube is maintained before the lower quick closing valve to eliminate liquid pools within the test section. A high-speed camera is used to capture high-speed video of flow regimes. Its resolution is 512*512 and it records 2200 frames per second. Phantom CV 2.8 from Vision Research Inc. is used to process the video. The PVC pipe and two ball valves are connected by copper tubes whose inner diameter is 7 mm. The length of test section between two quick closing valves is 1500 mm (~214 diameters) for the horizontal configuration and 750 mm (~107 diameters) for the vertical configuration. Longer test section cannot be achieved due to the space limitation. A bypass loop is parallel to the test section. After the refrigerant passes test section, after-coolers and a sub-cooler cools the refrigerant into subcooled liquid condition, which is fed into the gear pump to finish the loop.

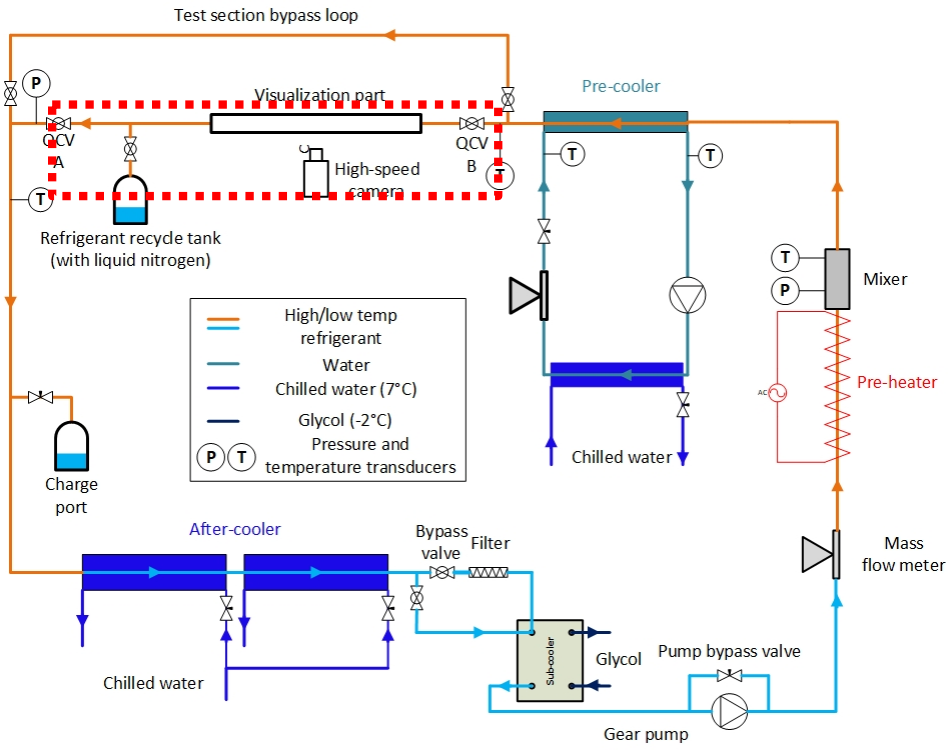

Figure 2 Schematic drawing of experimental facility, test section in the red box

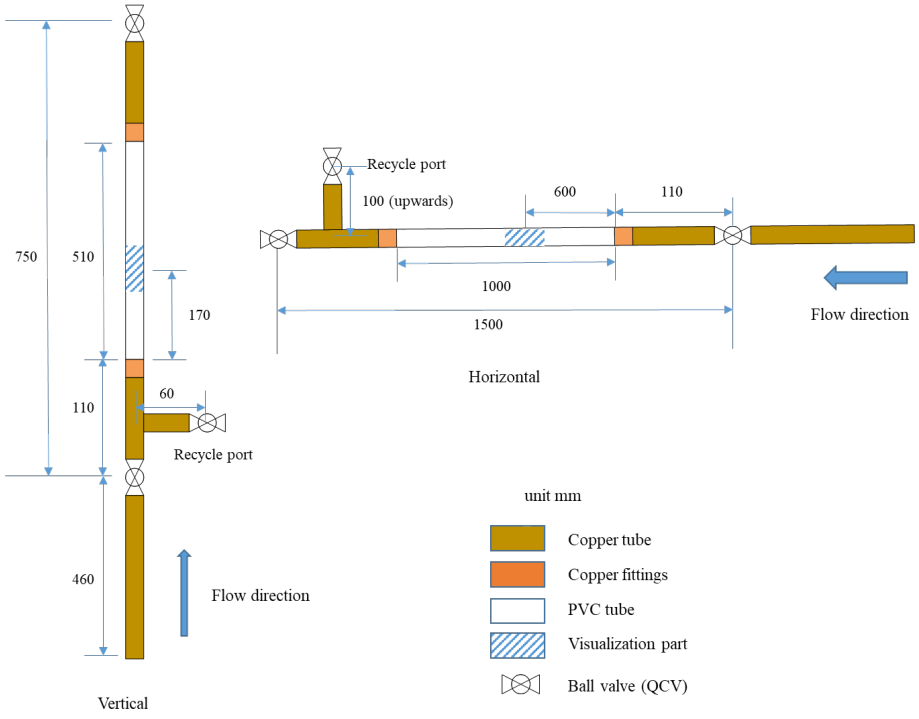

Figure 3 Schematic drawing for horizontal and vertical test section

2.4 Experimental procedure and conditions

- Set up certain mass flux by controlling the gear pump speed with a VFD.
- Superheat refrigerant with the electric heater. Superheat in the mixer is maintained at approximately 5K to guarantee the refrigerant is in vapor phase. Bulk enthalpy of refrigerant is then determined.
- The pre-cooler is then used to cool the refrigerant into a desired vapor quality condition before the test section.
- The temperature in the test section is set at 33ºC. The saturation temperature is set by the temperature of the water bath of the charge port.
- After the system becoming stable, get video footage from high-speed camera and refrigerant retention with quick closing valves (A and B) and liquid nitrogen recovery.

Table 2 lists the experimental conditions and Table 3 lists thermal properties of R134a at 33ºC.

Table 2 experimental conditions

Working media	R134a
T_r	33ºC
Test section orientation	Horizontal and vertical
Test section length	Horizontal: 1500mm (~214 diameters) Vertical: 750mm (~107 diameters)
Mass flux	Horizontal: 40, 80, 115 and 150kg/m^{2}s Vertical: 65, 80 and 115kg/m^{2}s
Quality	0.05-0.9

Table 3 Thermal properties of R134a at 33 ºC

Properties	Value
Liquid phase density (ρ_l)	1176kg/m^3
Vapor phase density (ρ_v)	41kg/m^3
Liquid phase dynamic viscosity (μ_l)	0.000176kg/m s
Vapor phase dynamic viscosity (μ_v)	0.00001234kg/m s
Surface tension (σ)	0.006993N/m

2.5 Data reduction and uncertainty

Following equations are used to determine void fraction for a certain mass flux and quality of refrigerant in test section. With quick closing valves and liquid nitrogen recovery, total refrigerant weight is obtained:

$$M = \rho_V V_V + \rho_L V_L \tag{16}$$

Where M is total refrigerant weight in the test section. ρ_L and ρ_v are density of liquid and vapor refrigerant; V_L and V_v are volume of liquid and vapor refrigerant.

Total volume of the test section is the sum of volume of vapor phase and liquid phase:

$$V = V_V + V_L \tag{17}$$

Where V is the total volume of the test section.

Void fraction is defined as vapor volume over total volume:

$$\alpha = \frac{V_V}{V_V + V_L} \tag{18}$$

Hence, average void fraction in the test section is determined by

$$\alpha = \frac{\rho_L V - M}{(\rho_V + \rho_L)V} \tag{19}$$

To get void fraction with the equation, total volume of the entire test section between two quick closing valves must be obtained. Firstly, subcooled liquid refrigerant is filled into the whole system after the fully evacuation of air. The sauce refrigerant cylinder is in a water bath being heated to a relatively higher temperature to make sure any possible vapor in the system can be condense into liquid phase again due to the relatively lower ambient temperature. When the whole system is stable, as well as the temperature and pressure before and after the test section do not change, quick closing valves A and B are closed spontaneously. Density of refrigerant is determined by the temperature and pressure:

$$\rho = f(T, P) \tag{20}$$

It is determined by functions built in EES [35]. Refrigerant retention (M_{full}) is obtained with liquid nitrogen recycling. Total volume of the test section is:

$$V = M_{full}/\rho \tag{21}$$

This procedure is repeated twice for both horizontal and vertical conditions and the results are taken average to get V.

Two types of uncertainties are involved in this study. First is the uncertainty from instrumentation. The measurement uncertainties are included in Table 4.

Second is from quick closing valves method. Two ball valves are closed manually at the same time with sound stimuli to get refrigerant retention to determine void fraction for each situation. Brebner and Welfor [36] indicated college-age individuals had average reaction time (Δt) of 0.16s to sound stimuli. Hence, the uncertainty of refrigerant retention by QCV is given in Equation (22).

$$u_M = g * A * \Delta t \tag{22}$$

where g is the mass flux, A is the cross-sectional area of the test section and Δt is the reaction time.

Error propagation rule is given in Equation (23). It estimates overall uncertainty based on measured values.

$$u_c = \sqrt{\sum_{i=1}^{N} \left(\frac{\partial y}{\partial x_i}\right)^2 u^2(x_i)} \tag{23}$$

Where u_c is combined standard uncertainty, y is calculated variables, x_i is measured variables and $u(x_i)$ is the uncertain of x_i. This equation is built in EES [35] where the results are obtained.

Table 4 Measurement uncertainties

Measurement point	Variable	Instrument	Uncertainty
Refrigerant and water temperature	T_r, T_w	Sheathed T-type thermocouple	±0.05 K
Absolute pressure in the mixer and after the test section	P	Absolute pressure transducer	±0.073% FS
Refrigerant mass flow rate	$\dot{m}_r$	Coriolis mass flow meter	±0.1 g s^{-1}
Refrigerant recycling weight	M	Scale (calibrated)	±0.1 g

2.6 Experimental results

Both horizontal and vertical upwards flow configurations with R134a as the working media at 33ºC are studied in this work. The inner diameter of the clear PVC tube is 7 mm. 40, 80, 115 and 150kg/m^2s are tested for the horizontal configuration. For the mass flux of 150kg/m^2s, only flow pattern visualization is studied but void fraction is not tested. 65, 80 and 115kg/m^2s are conducted for vertical configuration. Vapor qualities tested ranging from 0.05 to 0.9 (Figure 4 and Figure 5).

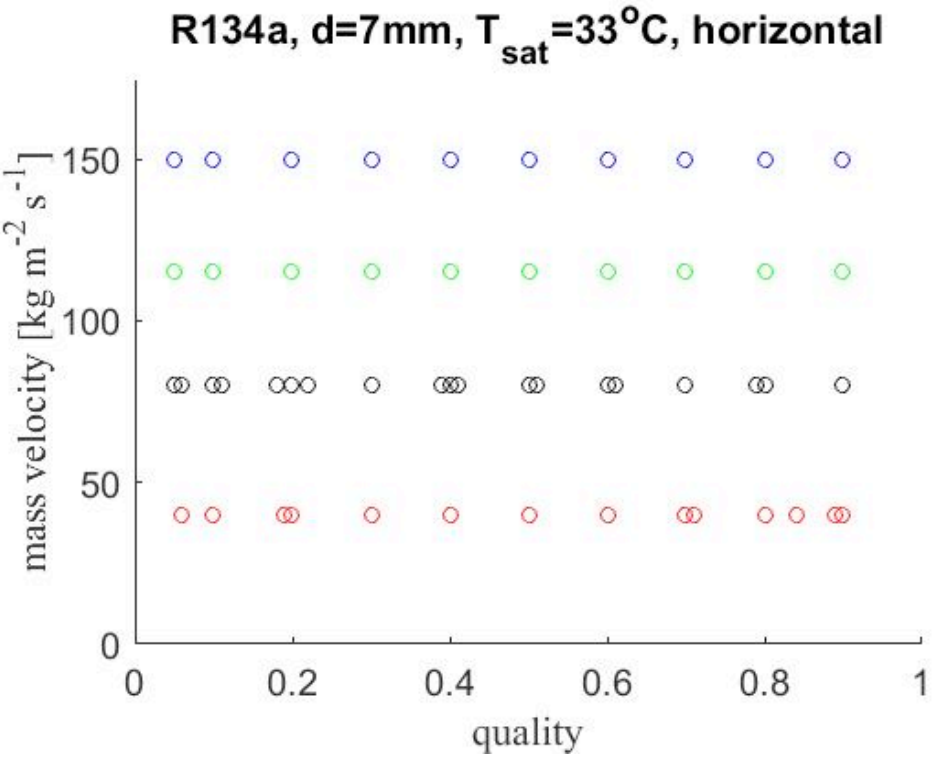

Figure 4 Flow regimes and void fraction datasets for horizontal configuration

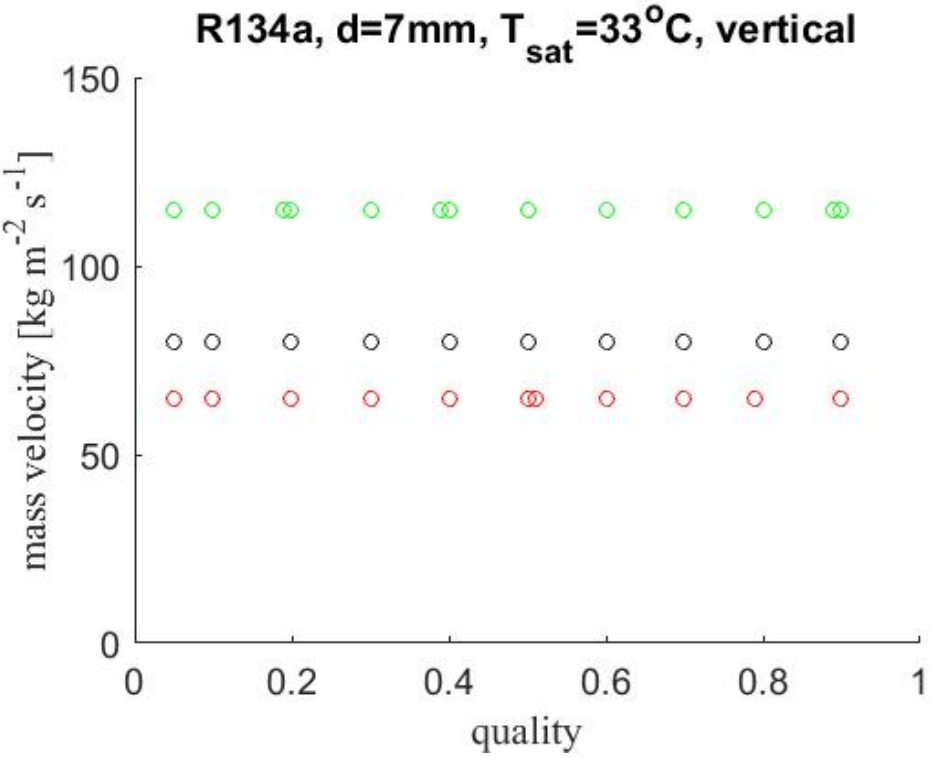

Figure 5 Flow regimes and void fraction datasets for vertical configuration

The flow patterns are determined by visual observation with a high speed camera filming two-phase flow patterns. Horizontal visualization results are compared and shown in the modified Wojtan-Ursenbacher-Thome [37] flow map.

Total experimental data set of 120 data points (60 for the horizontal configuration and 60 for the vertical configuration) are conducted and compared with some widely used void fraction correlations which are listed in Table 1.

The influences of mass flux and tube orientations on void fraction measurement will also be discussed.

2.6.1 Flow regimes and void fraction for horizontal flow

With high-speed video footages, three major flow regimes, slug flow, stratified flow and annular flow, are observed for the horizontal configuration in this mass flux range. Criteria for each flow regime is listed below:

***Slug flow*:** vapor slug appears in the upper portion of the tube periodically with liquid bridges in the middle.

***Stratified-wavy flow*:** liquid is flowing in the bottom of the tube and vapor is in the upper portion of the tube. The interface is wavy and no liquid bridges filled the entire cross section appear.

***Annular flow*:** liquid is flowing along the tube wall with vapor in the central core. Due to the influence of gravity, the liquid film is thicker at the bottom.

Visualization and classification of flow regimes is shown in Figure 6. Flow regimes for mass flux from 40 to 150 kg/m^{2}s with flow direction of right towards left are shown. Data are drawn in three geometries which represent different flow patterns: Δ-slug flow, □-stratified-wavy flow and ◊-annular flow. In this mass flux range, vapor slugs appear at relatively low qualities zone. As the vapor quality increases, the frequency of vapor slugs' appearance gets bigger. The length of liquid bridges between vapor slugs become smaller. As the quality increases to a certain range, liquid bridges break down and the liquid and vapor interface which is very wavy appears in the middle. The interface has a trend of becoming smoother as the quality increases. When the mass flux is high, liquid is flowing along the entire tube wall with vapor in the core. The liquid film at the bottom of the tube is thicker than that at upper part of the tube. When the quality equals to one, no liquid refrigerant appears in the test section.

In addition, visualization and classification of flow regimes is shown in the modified Wojtan-Ursenbacher-Thome [37] flow map. Wojtan-Ursenbacher-Thome [37] flow map was developed for flow boiling in horizontal tubes. However, in this study, the test condition is in adiabatic conditions, in which dryout and mist regimes will not appear. Hence, dryout and mist regimes in the flow regime map by Wojtan et al. [37] are omitted. They suggested two major flow patterns in this mass flux range: slug/stratified-wavy and stratified-wavy flow, which is different from this study: slug flow, stratified-wavy flow and annular flow. Some discrepancies can be explained as following:

When vapor quality is smaller than flow regimes transition line between intermittent and annular flow (x_{IA}), Wojtan et al. [37] found slug flow and stratified-wavy flow coexist with dynamic void fraction measurements. As the quality increases from 0 to x_{IA}, vapor slugs become longer and then liquid bridges breaks. These phenomena are similar to those in this study which are define as "slug" flow.

The transition between slug and stratified-wavy flow in the visualization result of this study agrees well to the transition line in the flow regime map. The flow regime map indicates higher vapor qualities as the transition line than the classification in this study. This may because classification of flow regimes dependent on subjective observation and different classification standards. In addition, it is relatively complicated to describe the transition between different flow regimes with a single line. The transition can be a certain range of vapor quality and mass flux. Some research [38, 39] proposed probabilistic mapping which indicates the flow can be described as the combination of different flow regimes.

Again, Wojtan et al. [37] flow regime map predicts flow patterns in evaporation conditions which is different from the adiabatic conditions. Hence dryout and mist zones are eliminated. In addition, the annular flow zone should be extended. With the mass flux of 150 kg/m^2s, annular flows appear at the higher vapor quality zone. Hence, under adiabatic conditions, the transition line between annular flow and stratified flow in Wojtan et al. [37] flow regime map should keep the slow decreasing trend at x=0.7 rather than increase dramatically when qualities is near unity.

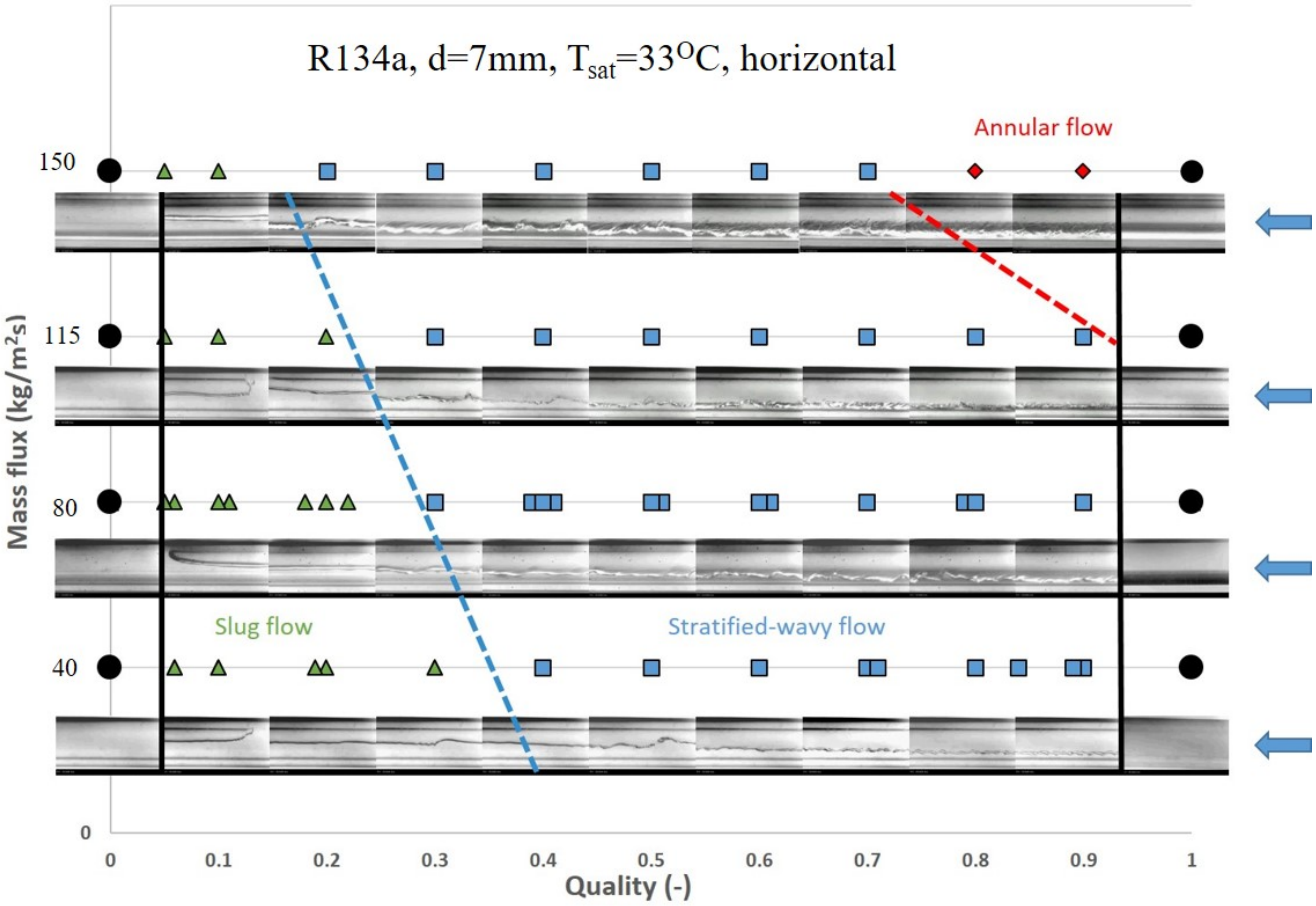

Figure 6 Visualization and classification of flow regimes for horizontal flow

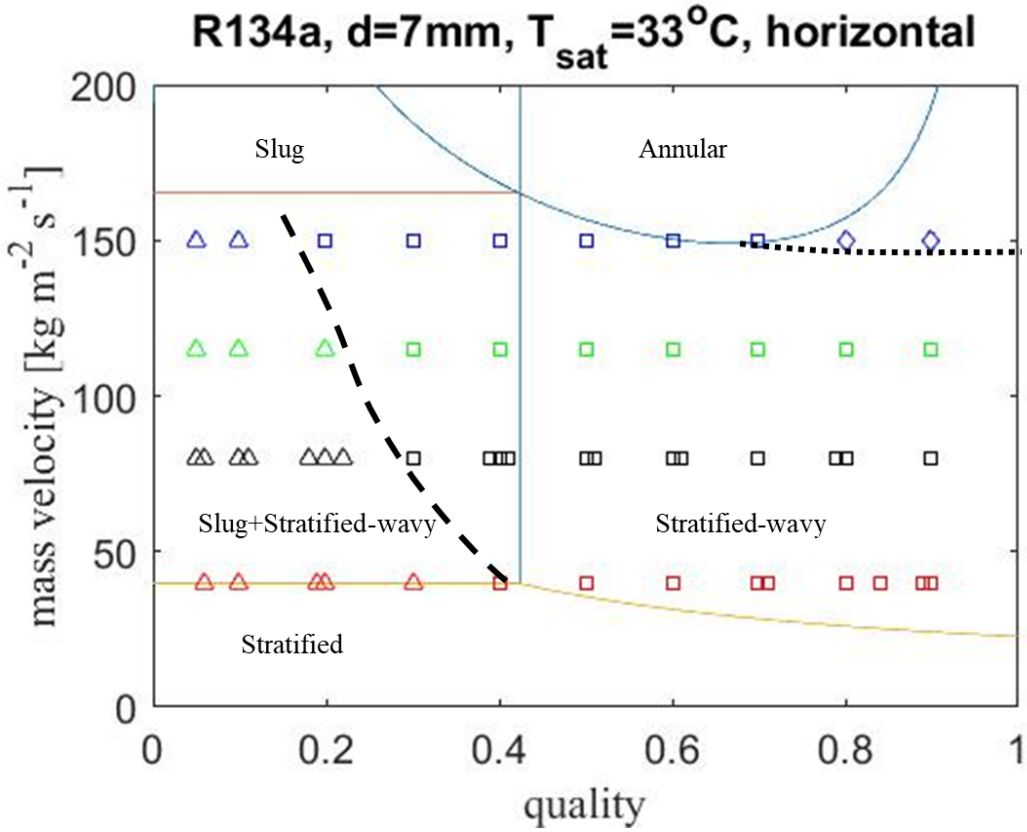

Figure 7 Visualization of R134a in the modified Wojtan-Ursenbacher-Thome [37] flow map (Δ-slug flow, □-stratified-wavy flow, − transition lines from the flow map, -- transition line between slug flow and stratified-wavy flow in this study, ··· transition line between annular flow and stratified flow in this study)

Figure 8 though Figure 10 show the results of void fraction vs. qualities compared with some correlations that Woldesemayat and Ghajar [22] recommended. Void fraction increases dramatically in low quality range ($0<x<0.15$). This is because liquid phase density is much bigger than vapor phase density, as shown in Table 3. Even small vapor quality (vapor weight ratio) in the test section requires relatively huge vapor volume.

In this mass flux range, experimental data agrees pretty well to the correlations from Woldesemayat and Ghajar [22] and Rouhani I [22, 32]. The predictions from Armand [26]-Massena [27] is larger than the experimental data. This correlation gives more precise predictions as mass flux increases. For homogeneous correlation, it gives the largest predictions and no data in this study is larger than its predictions. This obeys that homogeneous correlation predicts the upper limit of void fraction results.

This experiment is conducted in adiabatic condition with no heat transfer in the test section. No dryout or mist zone mentioned in the flow regime map from Wojtan et al. [37] in the boiling condition or condensing superheat zone from Xiao and Hrnjak [40] in the condensing condition. Hence, as vapor quality is approaching to unity, void fraction is supposed to approaching to one sharply. However, correlations from Woldesemayat and Ghajar [22] and Rouhani I [22, 32] do not show this trend. Homogeneous and Armand [26]-Massena [27] correlations predicts void fraction approaching to unity, which is suitable for adiabatic flows. Though their predictions are not as good as the former two in this mass flux range for R134a. Hence, when the vapor quality is close to one, Woldesemayat and Ghajar [22] and Rouhani I [22, 32] should be modified to show this trend. In conclusion, Woldesemayat and Ghajar [22] and Rouhani I [22, 32] correlations give pretty good predictions for adiabatic horizontal flows with R134a and this mass flux range.

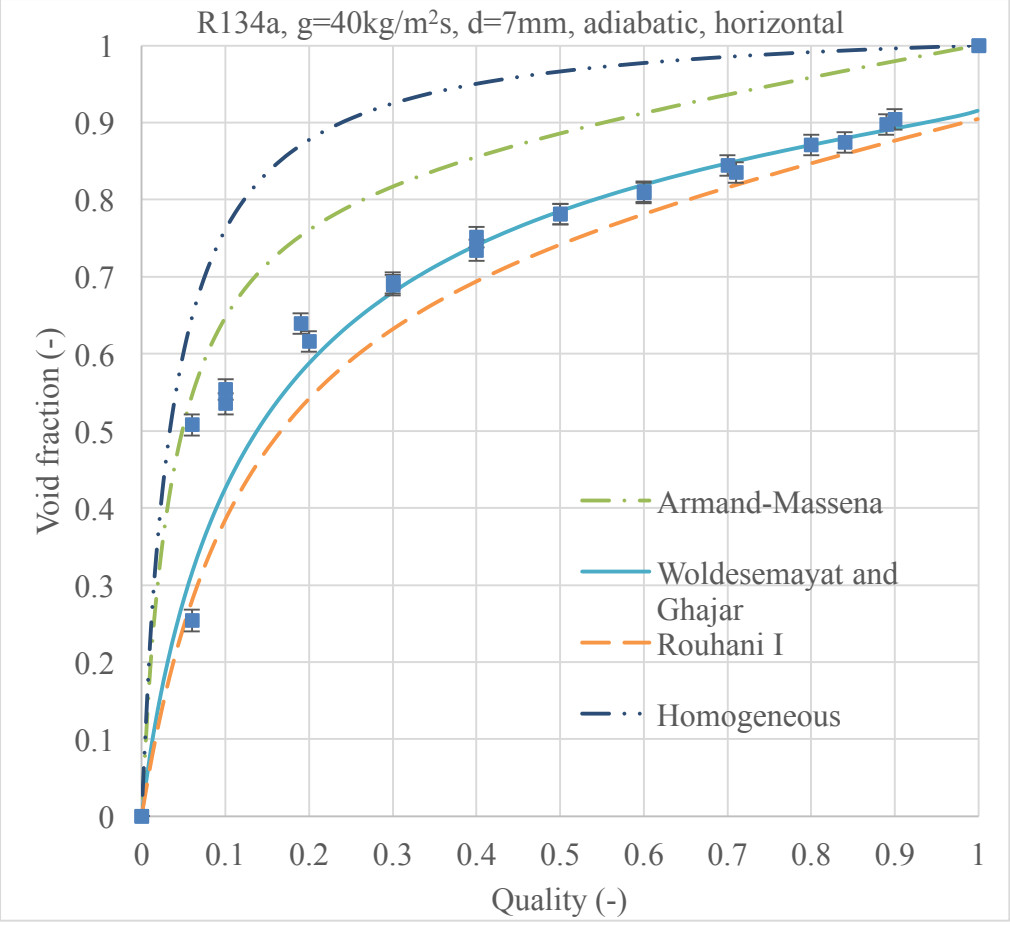

Figure 8 Void fraction vs. quality for g=40kg/m^{2}s for horizontal flows and correlations from Armand [26]-Massena [27], Woldesemayat and Ghajar [22] and Rouhani and Axelsson [22, 32]

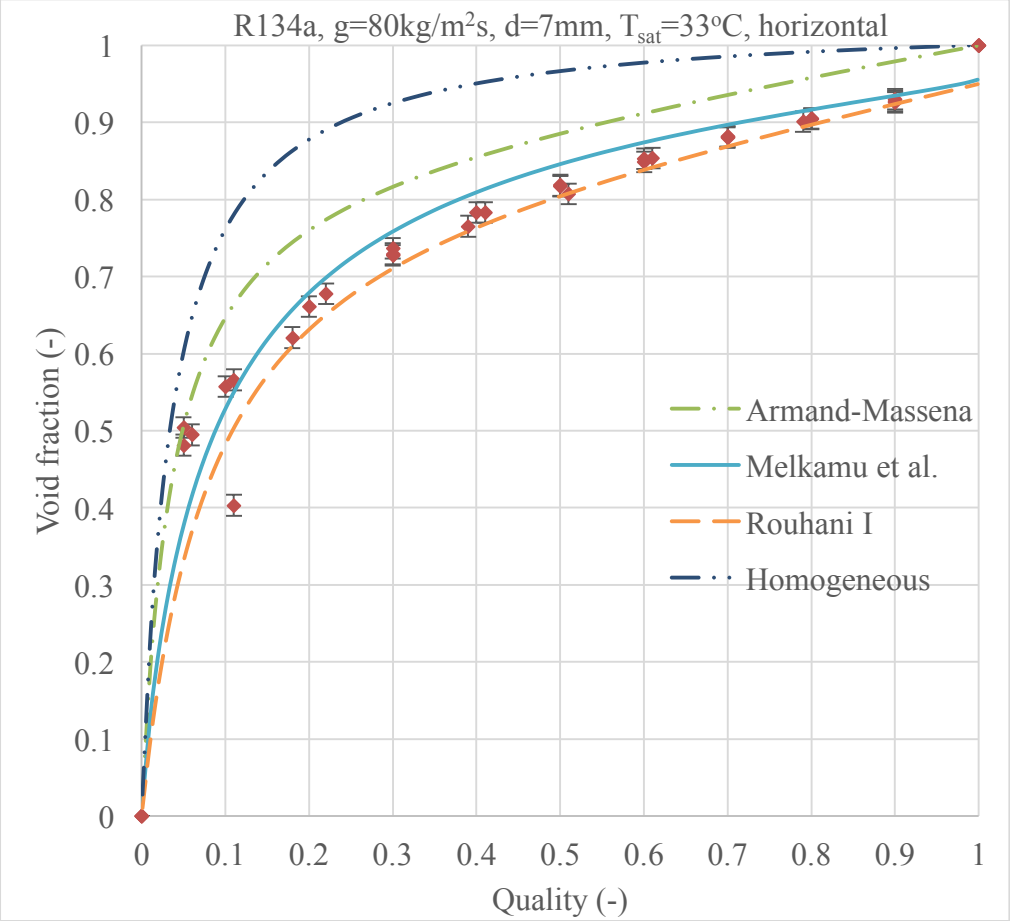

Figure 9 Void fraction vs. quality for g=80kg/m^{2}s for horizontal flows and correlations from Armand [26]-Massena [27], Woldesemayat and Ghajar [22] and Rouhani and Axelsson [22, 32]

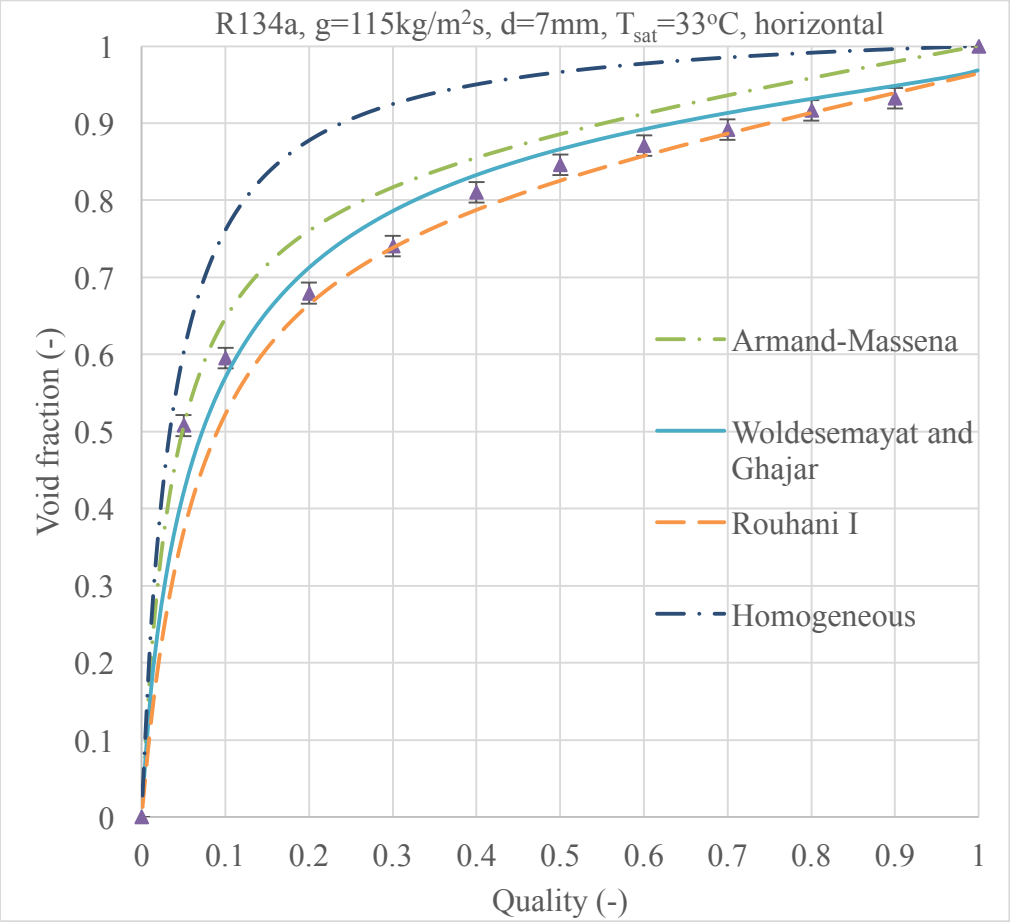

Figure 10 Void fraction vs. quality for g=115kg/m^{2}s for horizontal flows and correlations from Armand [26]-Massena [27], Woldesemayat and Ghajar [22] and Rouhani and Axelsson [22, 32]

2.6.2 Flow regimes and void fraction for vertical flow

For the upwards vertical configuration, high-speed camera is also used to capture flow patterns. Different from horizontal flows, slug flow, churn flow and annular flow are observed. Criteria for each flow regime is listed below:

***Slug flow*:** like slug flow in the horizontal flow, vapor slugs appears periodically with liquid bridge in the middle. But the slugs are in the middle of the tube and filling almost the entire cross section due to the direction of gravity to the flow is different.

***Churn flow*:** the vapor shear may near the value of gravity of liquid and pressure gradient. This results in chaos of the flow: liquid may goes up and down intermittently though the mean velocity of the two-phase mixture goes up. This flow pattern is highly agitated and the interface between liquid and vapor is hard to discriminate.

***Annular flow*:** liquid flows along the wall of the tube with vapor in the central core. It is relatively more stable and less chaotic.

Visualization and classification of flow regimes is shown in Figure 11. Flow regimes for mass flux from 65 to 115kg/m^{2}s are shown. Data are drawn in dots with three different shapes which represent different flow patterns: Δ-slug flow, □-churn flow and ◊-annular flow. Due to the limitation of experimental instruments, vapor qualities smaller than 0.05 cannot be obtained in steady states. Hence, bubbly flows which are supposed to be observed before slug flows are not captured by the high-speed camera in steady states. When the vapor quality is relatively small, vapor slugs and small bubbles appear in the test section periodically. As the quality increases, the flow pattern becomes more chaotic and the interface gets blurrier. It can be seen that liquid goes up and then sometimes down. When the vapor approaches to unity, the flow pattern becomes more stable. Vapor flows in the central core of the tube with liquid along the wall. As the vapor quality increases to one, no liquid appears in the test section.

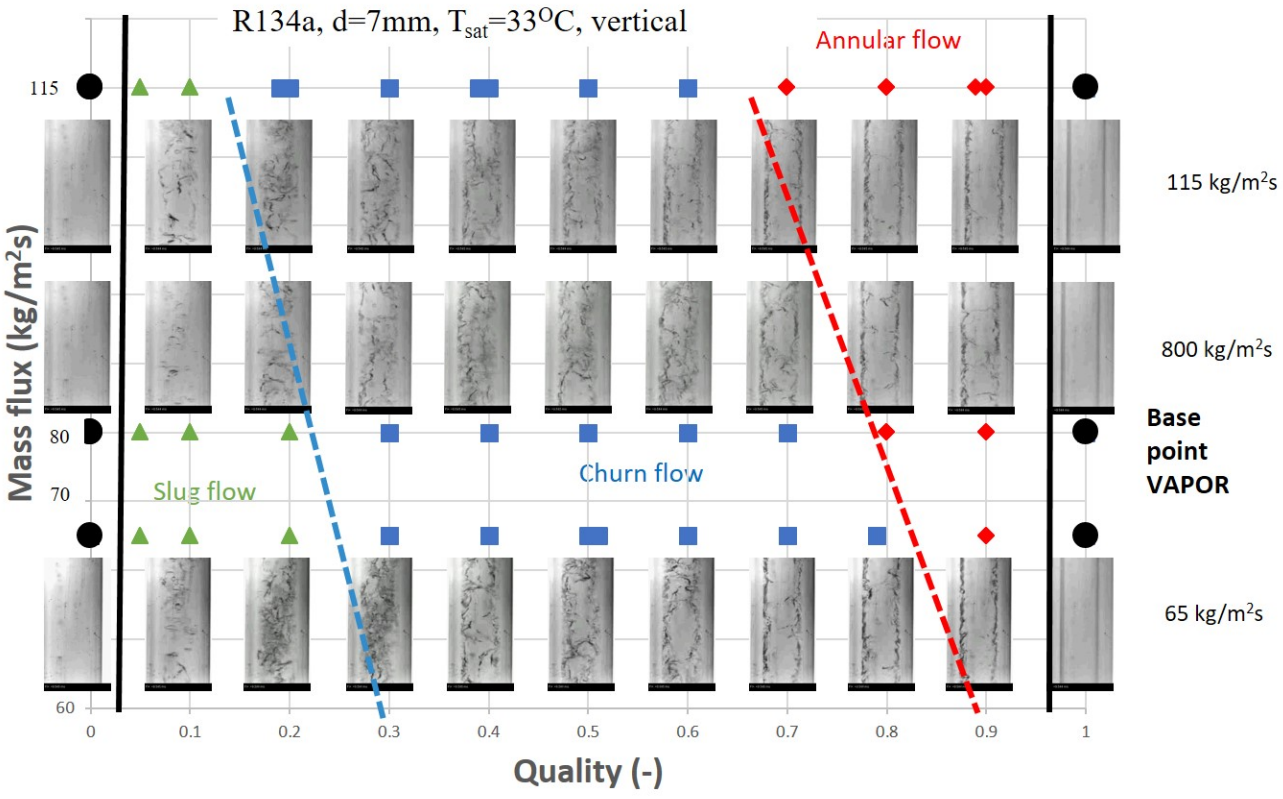

Figure 11 Visualization and classification of flow regimes for vertical flow

Figure 12 though Figure 14 show the results of void fraction vs. quality for different vapor qualities compared with Rouhani I and Rouhani II [22, 32], Dix [33] and Nicklin et al. [34] correlations. For the upwards vertical configuration, the void fraction shows similar trend to horizontal configuration. Void fraction increases dramatically at the low quality range ($0<x<0.15$) and then smoothly at the relatively high quality range ($0.15<x<1$).

In this mass flux range, experimental data agrees pretty well to the Rouhani II [22, 32] and Dix [33], follows by Rouhani I [22, 32]. Nicklin et al. [34] correlation gives larger predictions than the experimental data in the low vapor quality range and smaller predictions in the higher quality range. For homogeneous correlation, it also gives the largest prediction and no data is larger than its prediction. This obeys that homogeneous correlation predicts the upper limit of void fraction results.

Vertical configuration experiments are also conducted in adiabatic condition with no heat transfer in the test section. Hence, as vapor quality is approaching to unity, void fraction is supposed to approaching to one sharply. However, no correlations studied in this section except homogeneous correlation show this trend. Hence, when utilizing Rouhani II [22, 32], Dix [33] and Rouhani I [22, 32] correlations for adiabatic flow with R134a in this mass flux range to predict void fraction, modifications should be applied when quality is near one. In conclusion, Rouhani II [22, 32], Dix [33] and Rouhani I [22, 32] give relatively good predictions of void fraction for adiabatic vertical flow with R134a in this mass flux range.

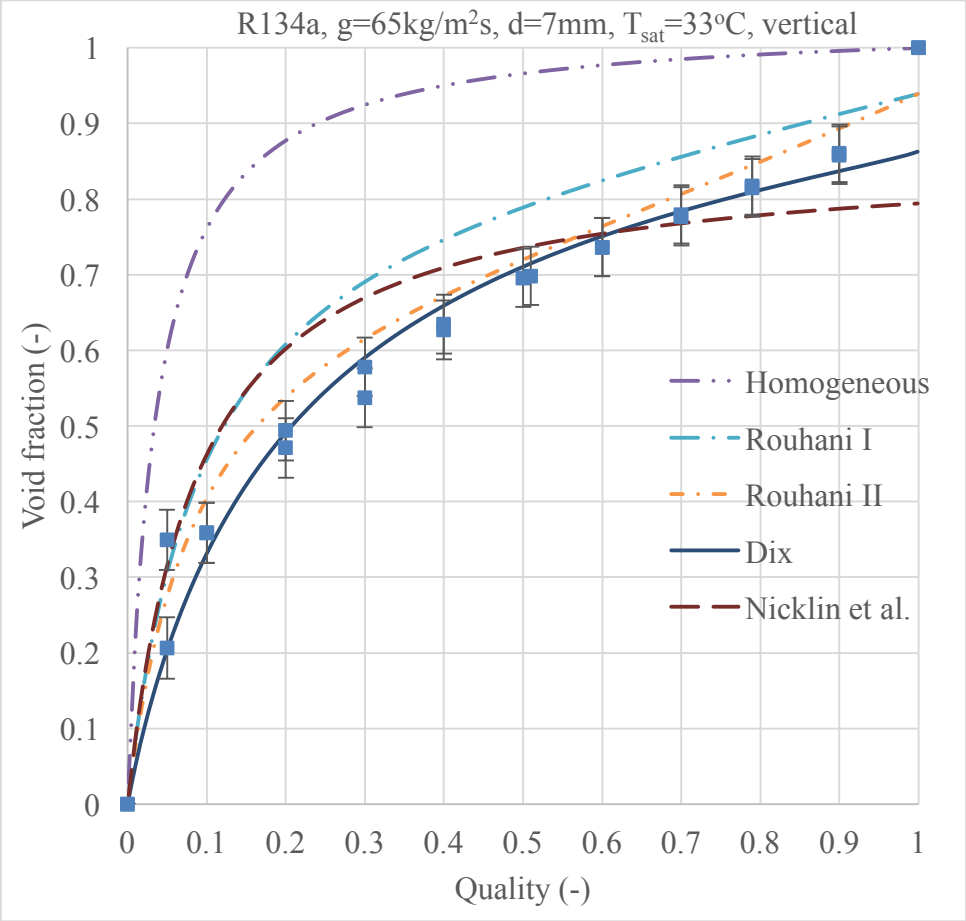

Figure 12 Void fraction vs. quality for g=65kg/m^{2}s for vertical flows and correlations from Rouhani and Axelsson [22, 32], Dix [33] and Nicklin et al. [34]

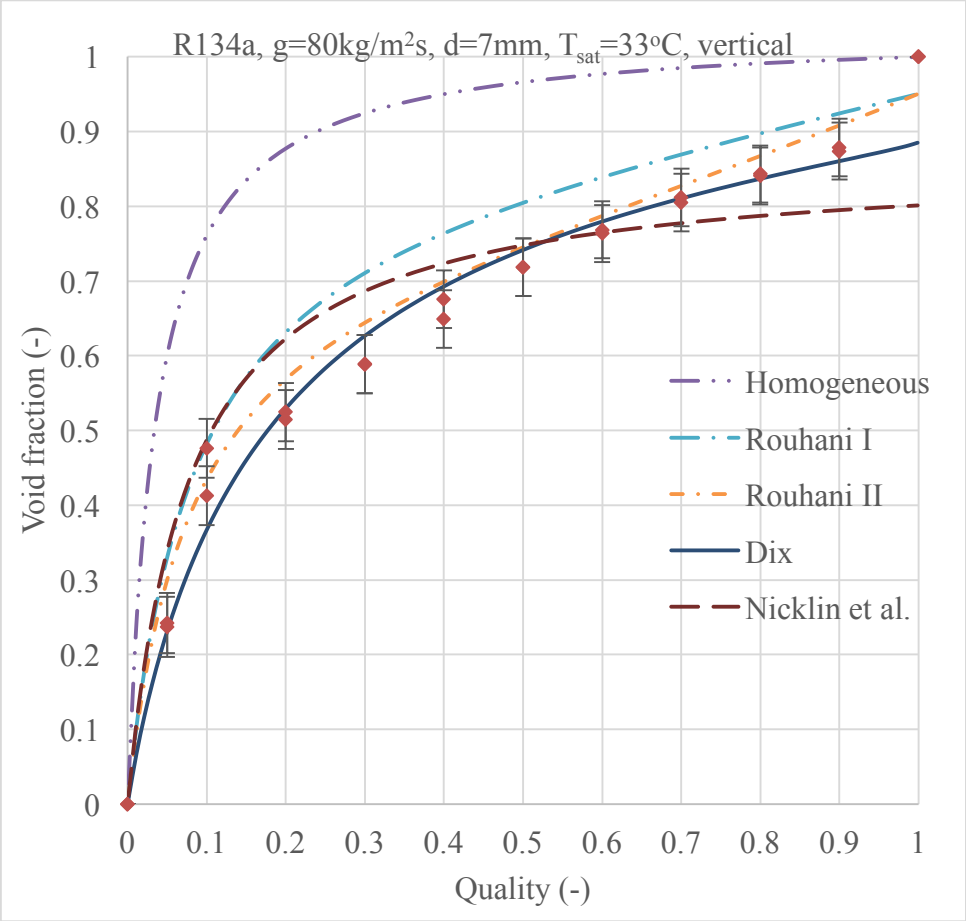

Figure 13 Void fraction vs. quality for g=80kg/m^{2}s for vertical flows and correlations from Rouhani and Axelsson [22, 32], Dix [33] and Nicklin et al. [34]

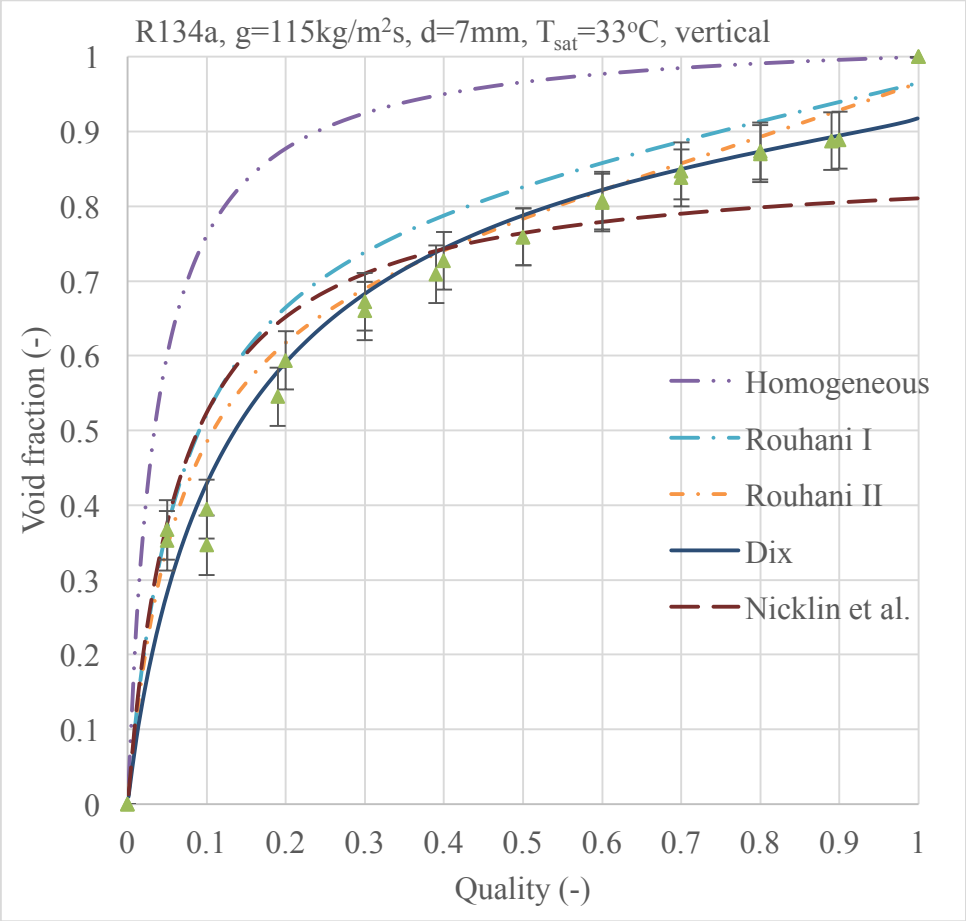

Figure 14 Void fraction vs. quality for g=115kg/m^{2}s for vertical flows and correlations from Rouhani and Axelsson [22, 32], Dix [33] and Nicklin et al. [34]

2.6.3 Influence of mass flux on void fraction

Figure 15 and Figure 16 show measured void fraction vs. vapor qualities and Rouhani I [22, 32] and Dix [33] correlations. The data shows that as mass flux increases, measured void fraction for a certain vapor quality will also increase. This can be explained that when mass flux increases, higher speed vapor may carry more liquid with it (the entrain ratio is bigger). The velocity difference between liquid phase and vapor phase is reduced and they are acting more like two-phase mixture with same velocity. This results in smaller slip ratio and more similar to homogeneous model.

Some correlations from drift flux and general empirical categories show this trend while many in slip ratio and $K\alpha_H$ categories not. Hence, when predicting void fraction with correlations for different mass flux, the former two categories are recommended. In this study, this phenomenon

agrees to the predictions from Rouhani I [22, 32] for horizontal flows and Dix [33] for vertical flows.

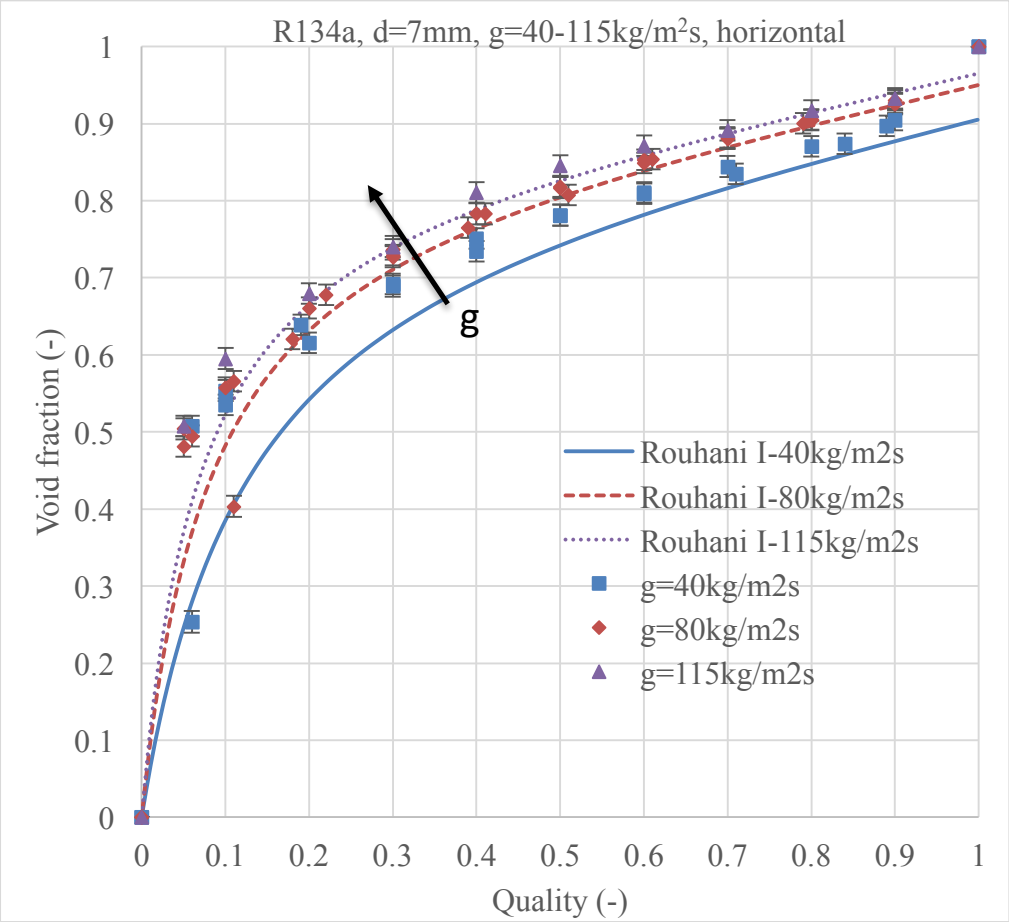

Figure 15 Void fraction comparison between different mass fluxes (horizontal) and comparison with Rouhani I [22, 32]

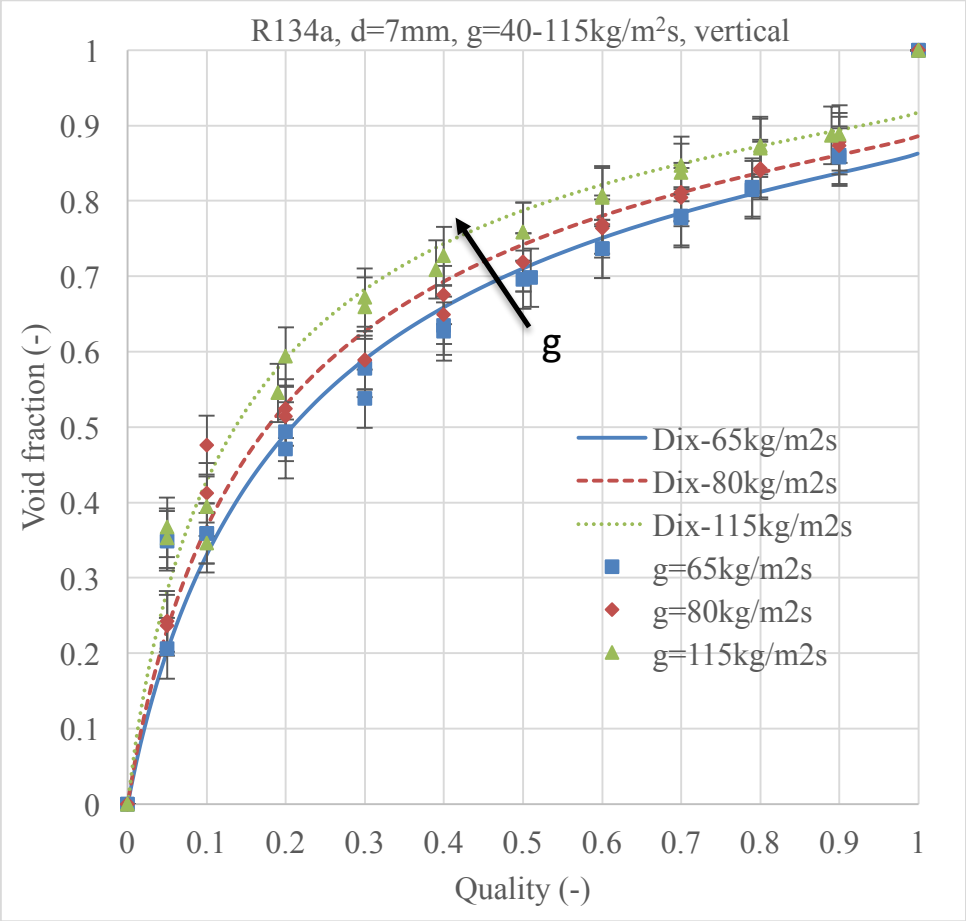

Figure 16 Void fraction comparison between different mass fluxes (vertical) and comparison with Dix [33]

2.6.4 Influence of tube orientation on void fraction

Figure 17 and Figure 18 compares the measured void fraction results in horizontal flows and vertical flows at the same mass flux. In both mass flux conditions (80kg/m^{2}s and 115kg/m^{2}s), void fraction results of vertical configurations is smaller than that in horizontal configurations. This may partially due to the slip ratio difference between the two tube orientations. In the upwards vertical flow, gravity will decrease liquid velocity and enlarge velocity difference between liquid phase and vapor phase. This results in higher slip ratio and void fraction is thus smaller.

In conclusion, tube orientations do have in influences on void fraction at the same mass flux. For different tube orientations: horizontal, upwards vertical, downwards vertical or inclined, different correlations should be chosen carefully before applying.

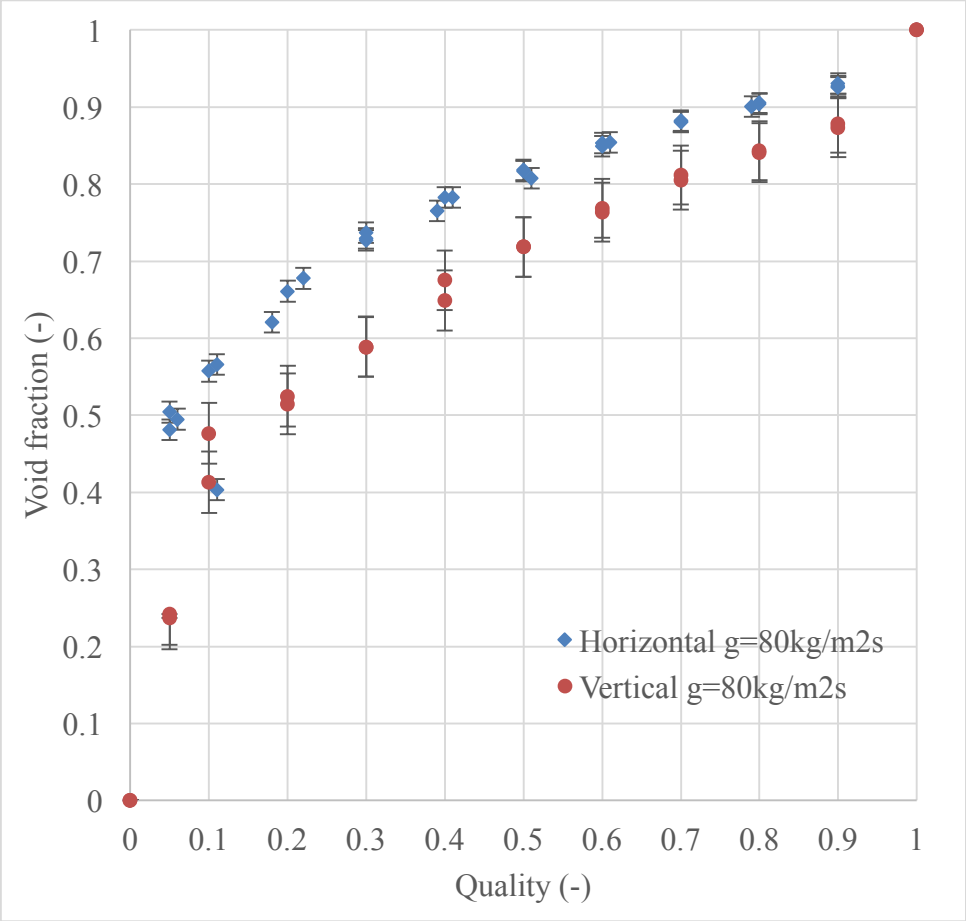

Figure 17 Void fraction results comparison between horizontal and vertical tube at g=80kg/m^{2}s

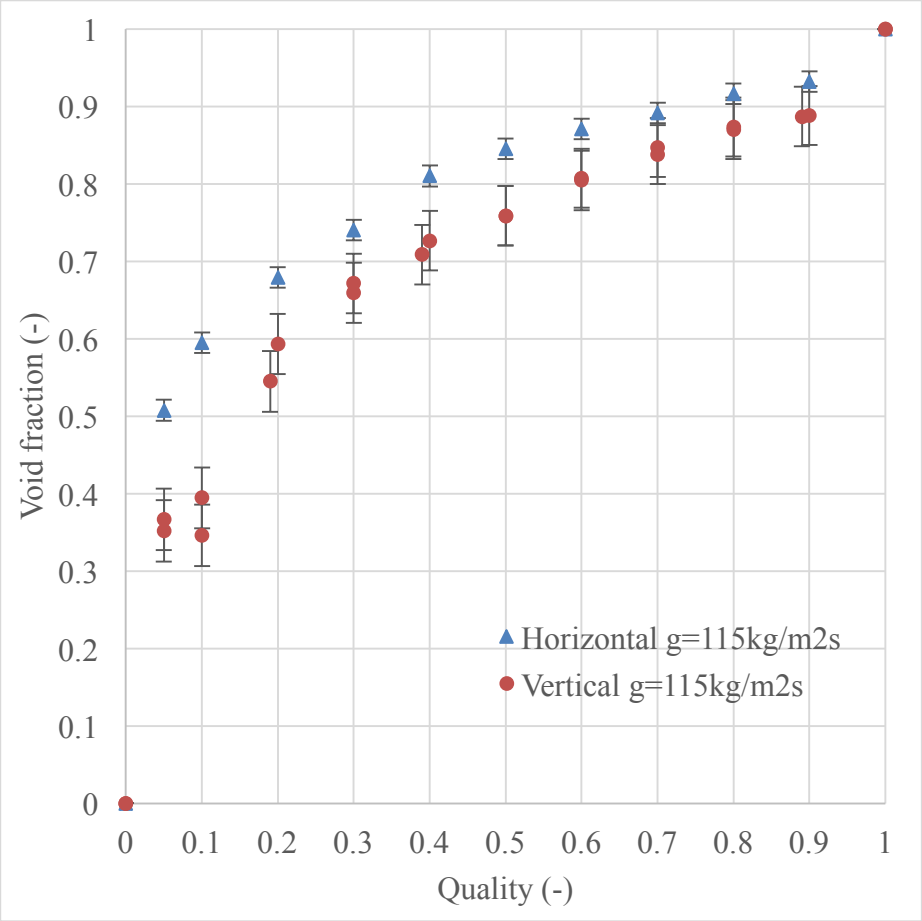

Figure 18 Void fraction results comparison between horizontal and vertical tube at g=115kg/m^{2}s

2.7 Conclusions

Flow regimes and void fraction in horizontal and vertical round tubes with R134a in adiabatic conditions and low mass flux range are studied in this chapter. In this mass flux range, three major flow patterns are observed in the test section for the horizontal configuration: slug flow, stratified-wavy flow and annular flow. This agrees well to the modified version flow pattern map proposed by Wojtan et al. [37]. Due to the influence of gravity, three major flow patterns are observed for upwards vertical flow: slug flow, churn flow and annular flow. More recent flow map for refrigerant in adiabatic upwards vertical configuration can be studied by further research.

For void fraction results, the experimental data is compared with some widely used correlations. For horizontal flows in this mass flux range, Woldesemayat and Ghajar [22] and Rouhani I [22, 32] correlations give pretty good predictions. Rouhani II [22, 32] and Dix [33], follows by Rouhani

I [22, 32] have good predictions for upwards vertical flows. Mass fluxes and tube orientations do have influences on void fraction results. Higher mass flux results higher void fraction than lower mass flux for the same vapor qualities due to higher entrain ratio and smaller slip ratio. Void fraction in horizontal flows is bigger than that in vertical ones due to smaller slip ratio. Hence, when applying correlations to predict void fraction for different mass flux or orientations, selecting a proper correlation is necessary. For the conditions similar to those in this study, Woldesemayat and Ghajar [22] and Rouhani I [22, 32] correlations for horizontal flows and Rouhani II [22, 32] and Dix [33] for upwards vertical flows are recommended.

Experiments are conducted in adiabatic conditions with no heat transfer involved in the test section. Hence, as vapor quality is approaching to unity, void fraction is supposed to approaching to one sharply. However, the correlations mentioned above failed to show this trend. Modification of these correlations when predicting void fraction for the vapor qualities close to unity may be proposed for further studies.

In the following two chapters, a capacitive sensor is proposed to characterize the flow patterns and void fraction results from this chapter.

CHAPTER 3 CAPACITIVE SENSOR DESIGN AND BUILDING

3.1 Literature review

For vapor-liquid two-phase mixtures, like refrigerant, which is commonly used in HVAC&R industry, flow regimes and void fraction are two crucial parameters that effect heat transfer coefficient and pressure drop. Drahoš and Čermák [41] made a review on different methods to determine flow regimes in two-phase flow. They proposed two categories of methods. The first one is measuring some structural parameters which are related to liquid and vapor phase. Methods in this category typically determine void fraction to characterize flow patterns. Several methods are included: *visual observation, photography, X-ray photography, optical, photon attenuation techniques, hot film anemometry and electrical method*. The second one is measuring an energetic parameter: *wall pressure fluctuations and wall shear stress fluctuations*. In this chapter, electrical impedance method is presented.

The electrical impedance method can be used to measure void fraction and detect flow regimes in two-phase flows. It utilizes different electrical properties between liquid phase and vapor phase of working media. The electrical impedance is defined as in Equation (24), where R is the resistive term and ωC is the capacitive term. For those working media with very low conductivity, the influence of resistivity can be neglect and capacitive method can thus be used.

$$Z = R + \frac{1}{j\omega C} \tag{24}$$

Keska et al. [5, 6] suggested that capacitive signals showed very good potential to recognize flow patterns. Many researchers designed capacitive sensors to measure void fraction and detect flow regime for two-phase flows. Abouelwafa and Kendall [7] applied the capacitive sensors to measure phase percentage and compared different electrodes configurations (Figure 19). After them, various sensor designs, electrodes configurations (Figure 20) and circuits to measure signals were proposed by many researches. Some researchers [8-10] directly measured the capacitance within the sensors with different electrodes configurations to determine void fraction and/or flow regimes. Elkow and Reskallah [11] utilized the measuring circuit based on charge/discharge principle with both concave and helical wound electrodes configurations to measure void fraction. Canière et al.

[15, 16] used two concave electrodes to characterize tow-phase flow in horizontal tubes with the circuit also based on charge/discharge principle. Jaworek et al. [12, 13] used senosrs with two concave electrodes with circuit measuring changes of frequency which are generated by a reference oscillator and sensors. Jaworek and Krupa [14] proposed a new measurement circuit which measured phase shift between a reference signal and a sinusoidal signal passing the sensors.

All the studies mentioned above [7-16] used other kinds of working media rather than refrigerant. Also, almost of the studies focused on measuring volumetric void fraction. However, for HVAC applications, refrigerant is the most commonly used media in systems. In addition, cross-sectional void fraction is more crucial to determine heat transfer coefficient and pressure drop. In microchannel heat exchangers, for example, local void fraction along the headers will also effect refrigerant charge quantities and distribution in heat exchangers. Canière et al. [17] utilized their sensors for refrigerant two-phase flows characterization. Their sensors are aimed to detect local refrigerant flow patterns. Kerpel et al. [42, 43] calibrated the sensor developed by Canière et al. [17] to measure void fraction based on flow regimes and capacitive signals. Olivier et al. [44] used the calibrated sensor [42, 43] to measure void fraction in a smooth tube with different inclination angle during condensation.

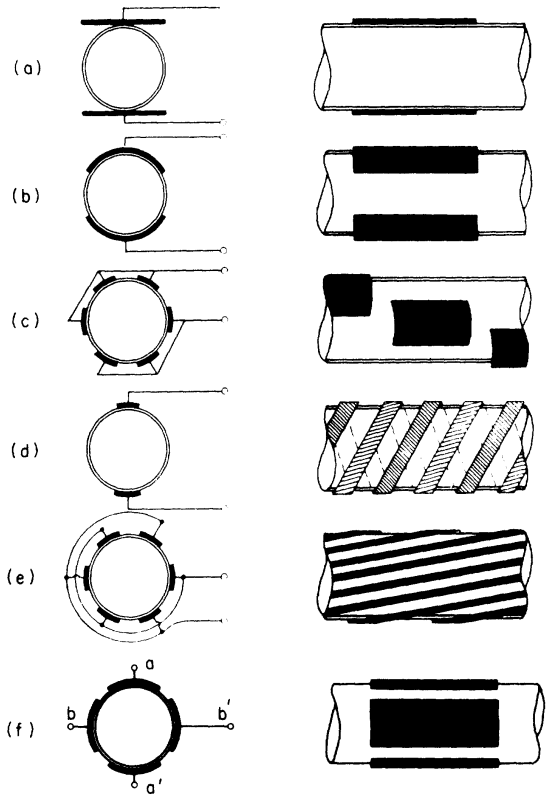

Figure 19 compared electrodes in Abouelwafa and Kendall's study. (a) Parallel plates. (b) Concave plates. (c) Staggered concave plates. (d) Double helix. (e) Multiple helix. (f) Four concave plates [7].

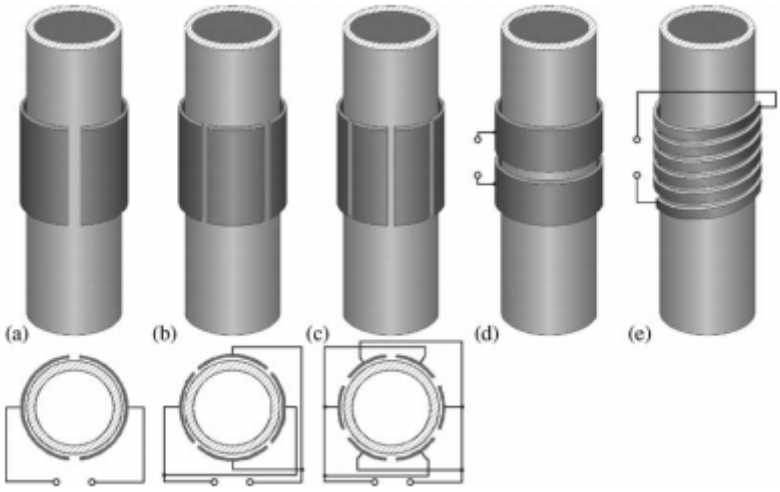

Figure 20 Some other typical electrode configurations. (a) Two concave plates. (b) Four concave plates. (c) Six concave plates. (d) Rings. (e) Double helix. [13]

The purpose of this chapter is to modify and further develop the sensor proposed by Canière et al. [17]. A procedure of calibration for the new sensors based on experimental data and characterizing flow regimes for two-phase flow is reported in next chapter.

3.2 Capacitive sensor design

3.2.1 Capacitance governing equations and dielectric constant

The capacitance (C) of a typical two-parallel-plate arranged configuration capacitor, is defined in Equation (25).

$$C = \frac{Q}{V} \tag{25}$$

where Q is the charge of the conductor and V is the voltage between two plates.

The electric field and voltage between the two plates is

$$E = \frac{Q}{\varepsilon A} \tag{26}$$

$$V = Ed = \frac{Qd}{\varepsilon A} \tag{27}$$

then

$$C = \frac{\varepsilon A}{d} \tag{28}$$

where A is the plate surface area and ε is permittivity. The permittivity is defined as $\varepsilon = \varepsilon_0 \varepsilon_r$, which is the product of vacuum permittivity ($\varepsilon_0 = 8.854 \times 10^{-12}$ F/m) and dielectric constant (ε_r). Dielectric constant is also called relative permittivity, which is a material property. It various among different materials and is temperature dependent.

When capacitors are in series, the equivalent capacitance (C_{eq}) is:

$$\frac{1}{C_{eq}} = \sum \frac{1}{C_i} \tag{29}$$

Equivalent capacitance for capacitors in parallel:

$$C_{eq} = \sum C_i \tag{30}$$

Canière [45] gave a general governing equation of capacitance:

$$C = -\varepsilon_0 \frac{\oint_S \varepsilon_r(\vec{r}) \nabla \Phi \cdot dA}{\Phi_S - \Phi_d} \tag{31}$$

where Φ_S is source electrodes electric potential and Φ_d is detector electrodes electric potentials. Φ is spatial potential distribution. Equation (31) must be solved to get analytical solution of capacitance for different sensor configurations and flow regimes. However, analytical solutions to some flow regimes appear in this study are difficult to obtain. Experimental measurement and calibration are thus preferred. Equation (31) also shows the capacitance is dependent on dielectric constant. Hence, it is important to exam dielectric constants for different working media in the literature and this study.

In this study, the working media is R134a, whose electrical conductivity is very low. Conductivity and dielectric constant for different working media is shown in Table 5. Capacitive methods which neglects impedance influence is thus used. As mentioned above, one of important electrical properties that capacitance signals dependent on is dielectric constant. The dielectric constant of water at 25ºC is much larger than that for R134a at ambient temperature. In addition, the dielectric constant difference between water and air is much bigger than that between R134a liquid phase and vapor phase. As a result, overall capacitance signal difference got between full liquid phase and full vapor phase of R134a is smaller, shown in Equation (32). The absolute capacitance signals measured from R134a two-phase mixture are also smaller than that from air-water mixture. The capability of the transducer to measure small capacitance signals (signals are typically in pF and ΔC_{R134a} is about 1 pF) is a limitation to the sensor design. Hence, to utilize capacitive sensors to refrigerant flow, some designs aimed to other working media from literature must be modified first.

$$\Delta C_{R134a} = C_{\text{full liquid}} - C_{\text{full vapor}} < \Delta C_{Water-Air} = C_{\text{full water}} - C_{\text{full air}} \tag{32}$$

The dielectric constant is a temperature dependent property. For R134a, several researches [46, 47] reported dielectric constant decreased as temperature increased. The change of dielectric constant

will effect capacitance measured from R134a two-phase flow. However, if the temperature is kept constant, this effect can be eliminated. This situation can be obtained when refrigerant is evaporating or condensing in the two-phase zone or refrigerant flows in headers of microchannel heat exchangers where no heat transfer occurs. If the temperature various and cannot be kept constant, Hewitt and Roberts [48] developed a procedure to correct the effect of fluid flow temperature variation.

Table 5 Conductivity and dielectric constant for some working media [49]

Working media	Volume Resistivity (MΩ/m)	Dielectric constant (-)
Air (0ºC)		1.00059
Pure water (25ºC) [50]	0.182	79.55
R134a liquid at ambient temperature	17700	9.51
R134a liquid at 77ºF		9.87
R134a vapor at 77ºF		1.0125
R410A liquid at ambient temperature	3920	7.78
R134a liquid at 77ºF		5.37
R134a vapor at 77ºF		1.0078

3.2.2 Key parameters determination

The capacitive sensor used in this study is firstly developed by Canière et al. [17]. Some modifications and further developments are made to this sensor so that it can be suitable for more configurations other than only horizontal tubes. Firstly, this sensor is used to characterize flow patterns in horizontal and vertical tubes. Next, a calibration procedure is proposed to measure void

fraction based on experimental data. After that, the application of this sensor will extend to measure void fraction along headers of microchannel heat exchangers in further studies.

Figure 21 and Figure 22 show the cross-sectional and side view of the capacitive sensor. Some key parameters need to be determined during the sensor design: dielectric layer thickness t, electrodes angle β, shield diameter R, orientation of the electrodes for horizontal configuration and axial electrode length L.

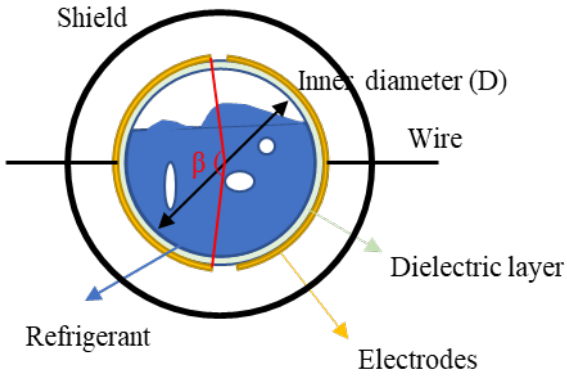

Figure 21 Cross-sectional schematic view of the capacitive sensor

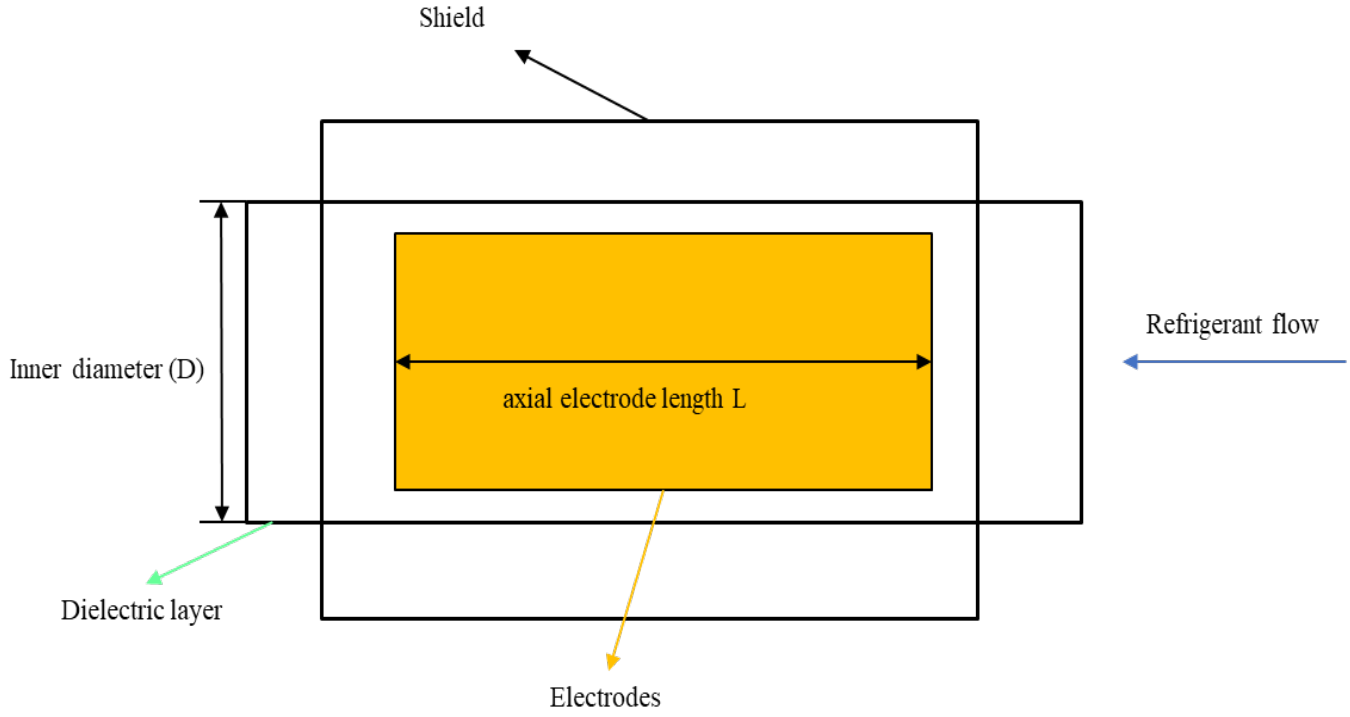

Figure 22 Side schematic view of the capacitive sensor

To obtain a higher homogeneity for the electric filed within the sensor and larger overall capacitance difference between full liquid phase and full vapor phase, Canière [45] reported *smaller shield radius, thinner dielectric layer thickness, larger electrode angle for the sensor and perpendicular towards gravity as the orientation of electrodes for horizontal configuration* should be applied.

For axial electrode length, Canière [45] selected L which equaled one inner diameter (D) and claimed it could be further reduced if the transducer could be improved. Many researches [11, 14, 51, 52] used sensors with electrodes of two-concave-plate configuration whose axial length were more than one diameter. No open literature used smaller sensors with two-concave-plate configuration and compared the signals from electrodes with different lengths. If sensors with smaller electrodes can work as functionally as ones with longer electrodes, the sensor will be more capable to measure local void fraction but also can be used in many other situations. For example, void fraction along headers in microchannel heat exchangers acts a crucial role in refrigerant charge prediction and refrigerant misdistribution improvement. Three pairs of electrodes with axial length of one inner diameter (D), 2D/3 and D/2 are tested in this study.

From the discussion above, Table 6 lists the most important parameters of the capacitive sensor.

Table 6 Dimensions of key parameters

Key parameter	dimension
Inner tube diameter, D	7 mm
Electrode axial length, L	D, 2D/3, D/2
Electrode angle, β	160º
Dielectric layer thickness, t	0.05 mm
Shield inner diameter, R	42.8 mm

3.3 Capacitive sensor building

The dielectric layer and electrodes are made up with a laminate circuit material Ultralam® 3850 from Rogers Corporation. This kind of material has following good properties which are suitable for this study [53]:

1. Extremely low moisture absorption: maintains stable electrical, mechanical and dimensional properties in humid environments.
2. High electrical volume resistivity: 10^{12} MΩ/cm. The dielectric layer and refrigerant are not conductive, the influence of resistivity can thus be neglect and capacitive method can be used.
3. Very thin. The thickness is 0.05 mm and thickness uniformity is excellent.
4. The dielectric constant is 2.9 at 10 GHz and 23 ºC.

Precise shape and location of electrodes on dielectric layer can be achieved by the etching technique. A photomask with desired pattern of electrodes is first made. After the circuit material attached to a silicon wafer, photoresist is spinning onto the surface with a programmable spinner. Then ABM Flood Exposure Model 60 is used to apply UV light onto the mask. After developing the photoresist pattern onto the surface, etching is applied to eliminate other parts of copper. Figure 23 and Figure 24 show the flexible circuit material before and after etching.

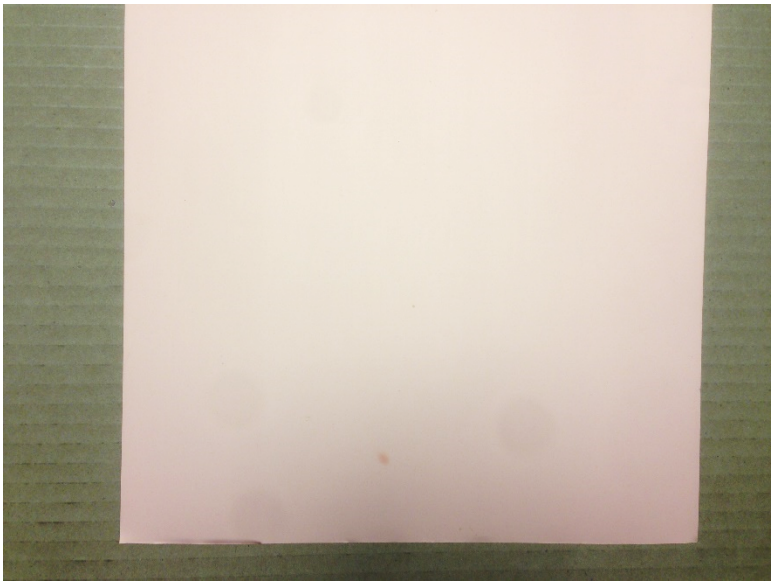

Figure 23 Flexible circuit material

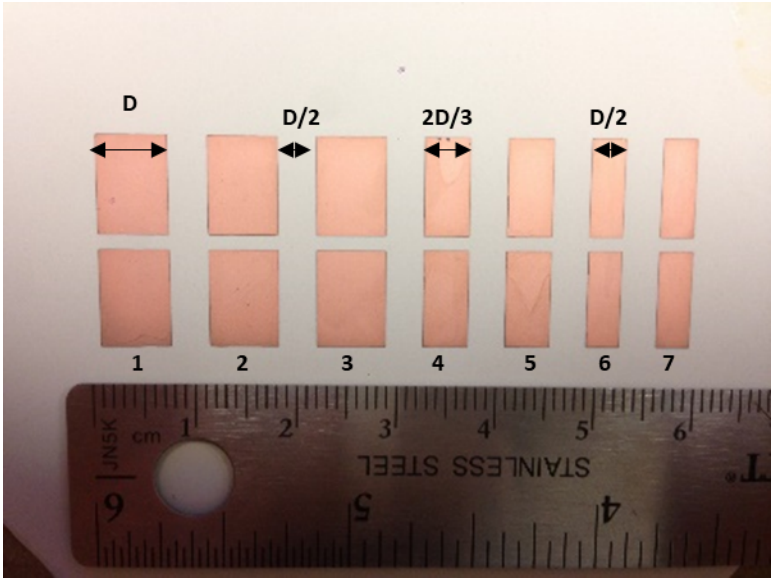

Figure 24 Electrodes after etching

Seven pairs of electrodes (1-7) with three different axial lengths locate in a row. The gap between each pair of electrodes is half diameter (D/2). First three pairs from the left (1-3) have the axial length of one diameter (D). The axial length of the two pairs of electrodes in the middle (4 and 5) is 2D/3 and the last two pairs (6 and 7) is D/2.

3D printed parts that make the dielectric layer with electrodes into a tube with diameter of 7 mm (D) is shown in Figure 25. Copper wires are then soldered onto the electrodes. Four pairs of electrodes (1, 3, 5 and 7) are connected to the ground as guarding electrodes (Figure 26). This is to reduce the fringing effect and let the electric field be kept within the electrodes. The other three pairs with different axial length measure the capacitance signal within the electric field.

More 3D printed parts are mounted outside of this tube to support the structural stability (Figure 27 and Figure 28). PVC tubes are glued on both sides of the sensor. Outside of the inner design of the sensor, a piece of aluminum tube which is connected to the ground is used as shield (Figure 29). This shield is to reduce outside influence like people moving or mobile signals. The gap between the 3D printed parts and the aluminum tube is filled with resin. The resin reduces acts also like a shield and ensure the sensor withstand higher pressure. Figure 30 shows the final schematic of the capacitive sensor.

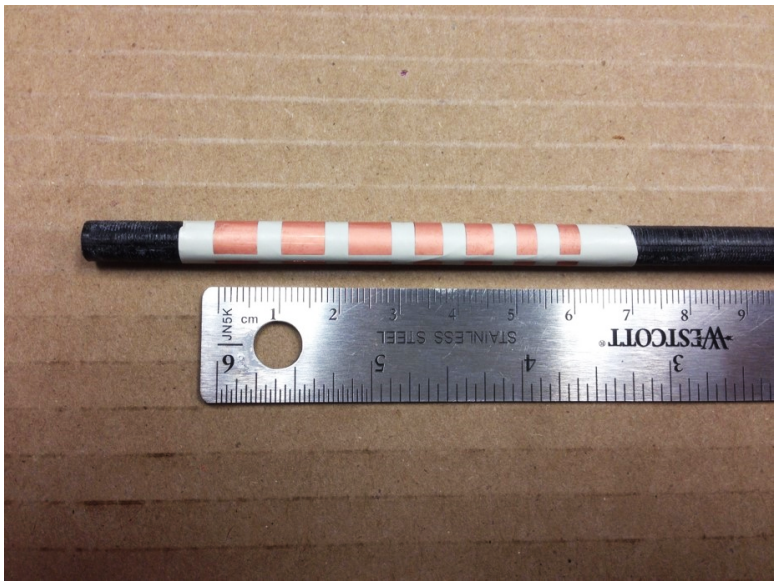

Figure 25 3D printed rode to make dielectric layer in to a tube

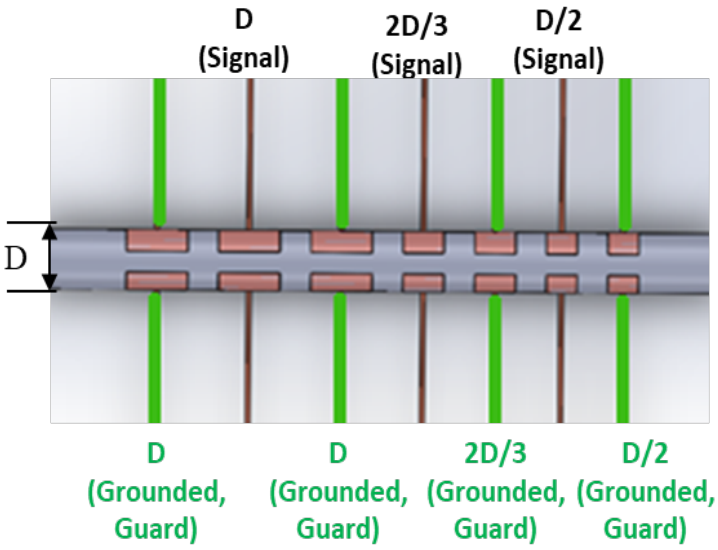

Figure 26 Schematic of the guarding electrodes

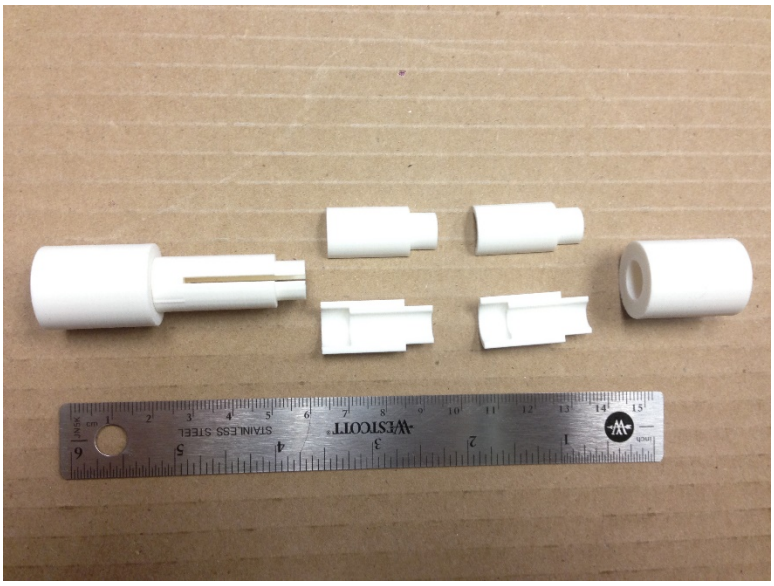

Figure 27 3D printed parts that support the structure of the tube

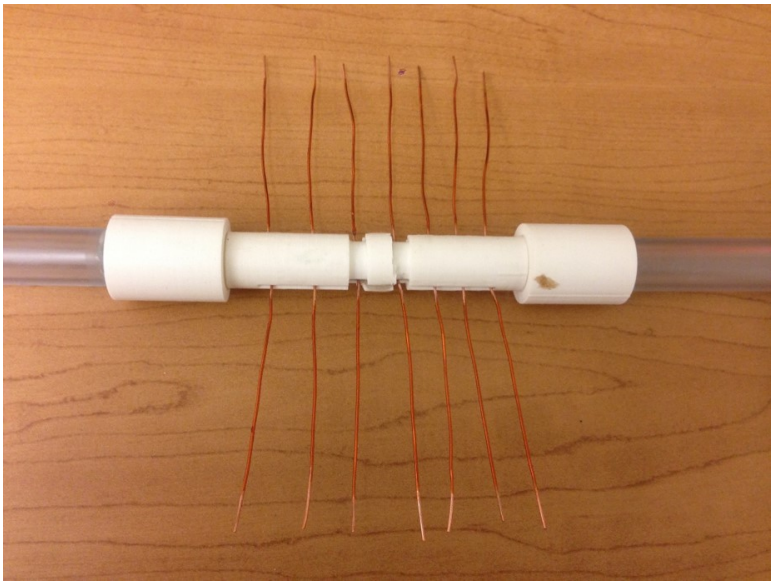

Figure 28 Inner design of the sensor

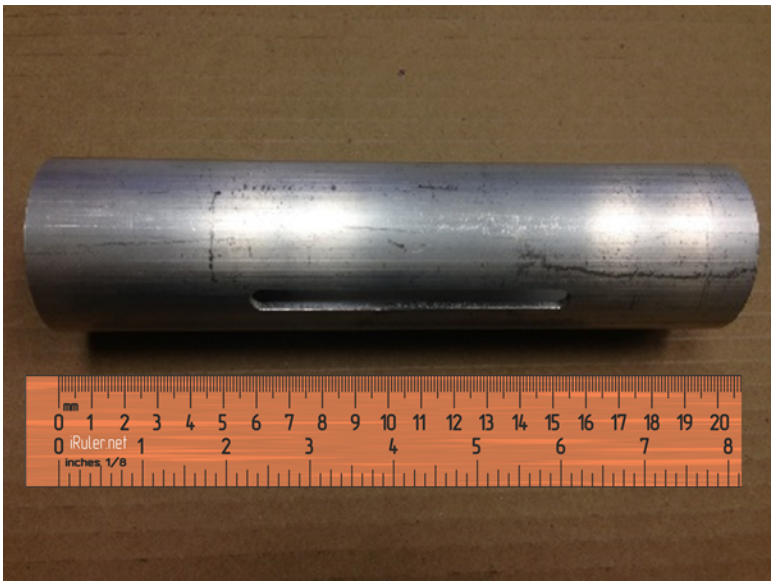

Figure 29 Aluminum tube as a shield

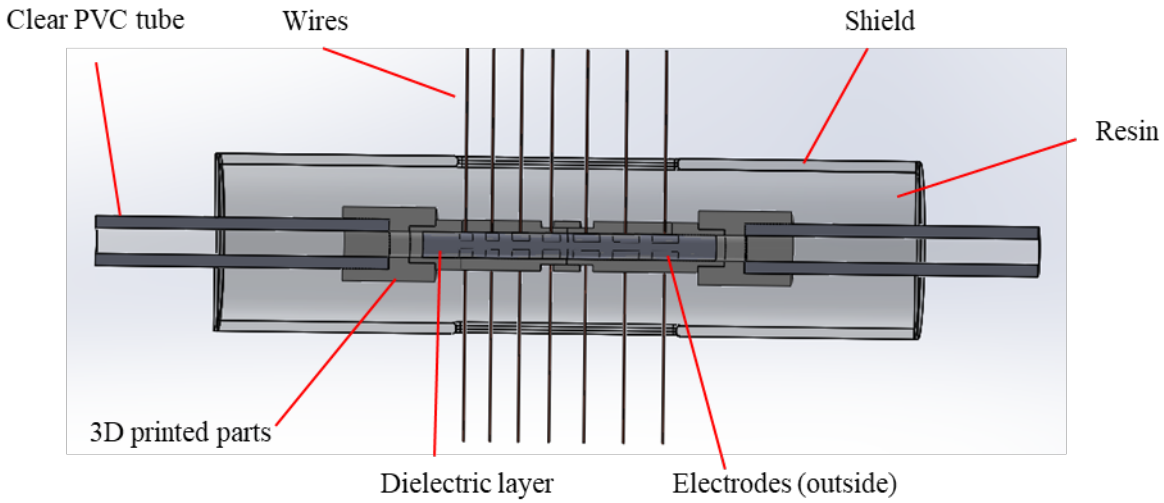

Figure 30 Schematic of the capacitive sensor

3.4 Transmitter selection

The capacitance signals that the sensor measures are in the order of pF. Hence, the transmitter must be capable to measure such small capacitance signals and have relatively high resolutions. Many research designed and built their own transducers and transmitters based on several techniques: charge/discharge technique [11, 15, 16, 45], frequency deviation [12, 13] and phase shift [14]. Some devices are designed to measure air-water two-phase mixture and may not be suitable for

refrigerant flows due to the electric property difference mentioned above. Canière [45] developed a suitable transducer for refrigerant flow that can measure capacitance signals in 0-10 pF range. However, this design is not open in the literature. In addition, this transducer is hard to be duplicated in other research and instrumental uncertainties may be introduced among different transducers. Looking for a commercially available transmitter which is suitable for this study is thus important. This can be helpful to experimental repeatability and more research can utilize the same configuration.

The transmitter used in this study is FDC2214EVM (Figure 31) from Texas instruments [54]. It is a commercially available module which can directly measure capacitive signals from custom sensors. Its features are as following:

1. Noise immune;
2. 4 available channels for costumed sensors at the same time;
3. Input capacitance range: 0 – 250000 pF (capacitance signals range for this study: 50 – 100 pF);
4. Resolution: up to 28 bits, approx. 0.001 pF;
5. Uncertainty: approx. 0.003 pF;
6. Cheap and easy to use.

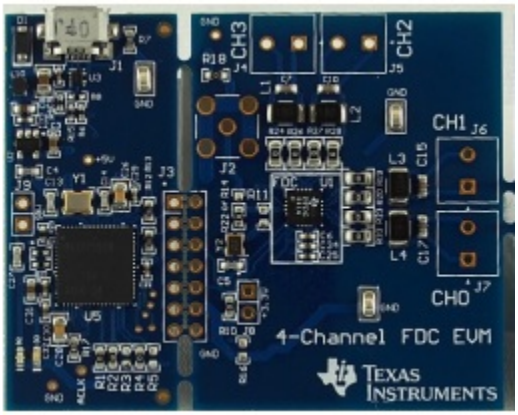

Figure 31 FDC2214EVM from TI [54]

3.5 Conclusions

The further modifications and building procedures for the capacitance sensor first proposed by Canière et al. [17] is discussed in this chapter. This sensor is built to detect flow patterns and

measure local void fraction for both horizontal and vertical flows with R134a. Some key parameters are determined to ensure higher resolutions and larger capacitance signal range. Three pairs of electrodes with different axial lengths (D, 2D/3 and d/2) locate in a row. This is to determine whether reliable capacitance signals can be read from electrodes with smaller axial length. If so, the sensor can thus be utilized in many applications, such as headers in microchannel heat exchangers where the space for sensors is limited.

FDC2214EVM from TI is selected to be the transmitter in this study. It is commercially available, easy and cheap to apply with custom sensors. In addition, the high resolution and suitable measurement range make it very proper for this study.

A procedure of calibration for the new sensors to measure void fraction based on experimental data and characterizing flow regimes for two-phase flow are reported in next chapter.

CHAPTER 4 CAPACITIVE SENSOR SIGNALS ANALYSIS AND CALIBRATION PROCEDURE FOR VOID FRACTION MEASUREMENT

4.1 Parameters for characterizing flow patterns and calibration method for void fraction measurement

The sensor developed in the last chapter is going to be used in this chapter to characterize refrigerant two-phase flow patterns as well as measure void fraction in both horizontal and vertical tubes. This sensor has a non-uniform electrical field and the signals are thus influenced by the distribution of two-phase flows. The signals not only show local void fraction, but also changes as flow pattern changes. Also, due to the non-uniform electrical field, the relation between capacitance signals and void fraction is not linear. A calibration procedure is needed before applying this sensor to measure of void fraction for different applications. Statistical signal processing parameters and calibration method for void fraction measurement is first discussed.

Drahoš and Čermák [41] had a review on statistical signal processing for characterizing flow patterns. Three domains can be utilized to characterize flow patterns: *amplitude domain, time domain and frequency domain*.

In the amplitude domain, probability density function (PDF) or probability density estimation (PDE) can be used to obtain signal amplitude distributions. In this study, probability density estimation which is to estimate the probability density in a non-parametric way is used. The estimation is based on a normal kernel function and evaluated at 100 equally-spaced points for the range of the data. Autocorrelation functions (ACF) and cross-correlation functions (CCF) are usually involved to have statistical analysis in the time domain. For the frequency domain, the signals can be described by the power spectral density function (PSDF) which using the Fourier transform.

Some researchs [15, 45] utilized the parameters mentioned above to characterize flow patterns water-air or refrigerant. In this study, few flow regimes are encountered due to the low mass flux range (40-115kg/m^{2}s). Hence, probability density estimation and time averaged signals are enough

to determine flow patterns. Further statistical signal processing can be conducted for higher mass flux range with more complex flow regimes.

To measure refrigerant two-phase flow void fraction, the capacitance must be calibrated first. De Kerpel et al. [42, 43] proposed two methods based on flow regimes or signal features to calibrate the sensor developed by Canière [45] for horizontal flows. In both methods, they calibrated FEM simulations with void fraction predicted by correlations from Rouhani and Axelsson [22, 32] rather than actual void fraction measurements in experiments. Though the correlation provides relatively good prediction, the difference between prediction and actual experimental measurements cannot be neglected. In addition, the calibration was only applied for horizontal flows. In many refrigeration and air conditioning applications, both horizontal and vertical flows are encountered. Hence, experimental measurements of void fraction should be used to calibrate for both tube orientations. In this study, quick closing valves are used to get void fraction for both horizontal and vertical configurations. Calibrated curves which can be utilized for further research are then proposed.

4.2 Experimental facility

Similar to the facility in Chapter 2.3, a gear pump system without oil is used (Figure 32). Subcooled liquid refrigerant (R134a) is pumped through a mass flow meter with a gear pump into an electric heater where refrigerant is heated into superheated vapor. Refrigerant is mixed in the mixer and the condition of refrigerant is determined by measuring its pressure and temperature. Then superheated vapor refrigerant flows into a pre-cooler whose secondary fluid is water. Water is cooled by building chilling water. With the energy balance of the water side in pre-cooler, the condition of refrigerant after the pre-cooler is determined. The model of pressure transducers is Setra Model 204 and thermocouples are T-type thermocouples. The test section includes between two quick closing valves (ball valves, manually open and close), the capacitance developed in Chapter 3 and a visualization part. Schematic drawing for horizontal and vertical test section is shown in Figure 33. The visualization part is a piece of schedule 80 clear PVC tube with inner diameter of 7 mm. Before the visualization section, 600mm (~86 diameters) of the same PVC tube for the horizontal configuration and 170mm (~25 diameters) for the vertical configuration is utilized to ensure the flow is fully developed. In addition, for the vertical configuration, 460mm

of tube is maintained before the lower quick closing valve to eliminate liquid pools within the test section. A high-speed camera is used to capture high-speed video of flow regimes. Its resolution is 512*512 and it records 2200 frames per second. Phantom CV 2.8 from Vision Research Inc. is used to process the video. The PVC pipe and two ball valves are connected by copper tubes whose inner diameter is 7 mm. The length of test section between two quick closing valves is 1500 mm (~214 diameters) for the horizontal configuration and 750 mm (~107 diameters) for the vertical configuration. Longer test section cannot be achieved due to the space limitation. A bypass loop is parallel to the test section. After the refrigerant passes test section, after-coolers and a sub-cooler cools the refrigerant into subcooled liquid condition, which is fed into the gear pump to finish the loop.

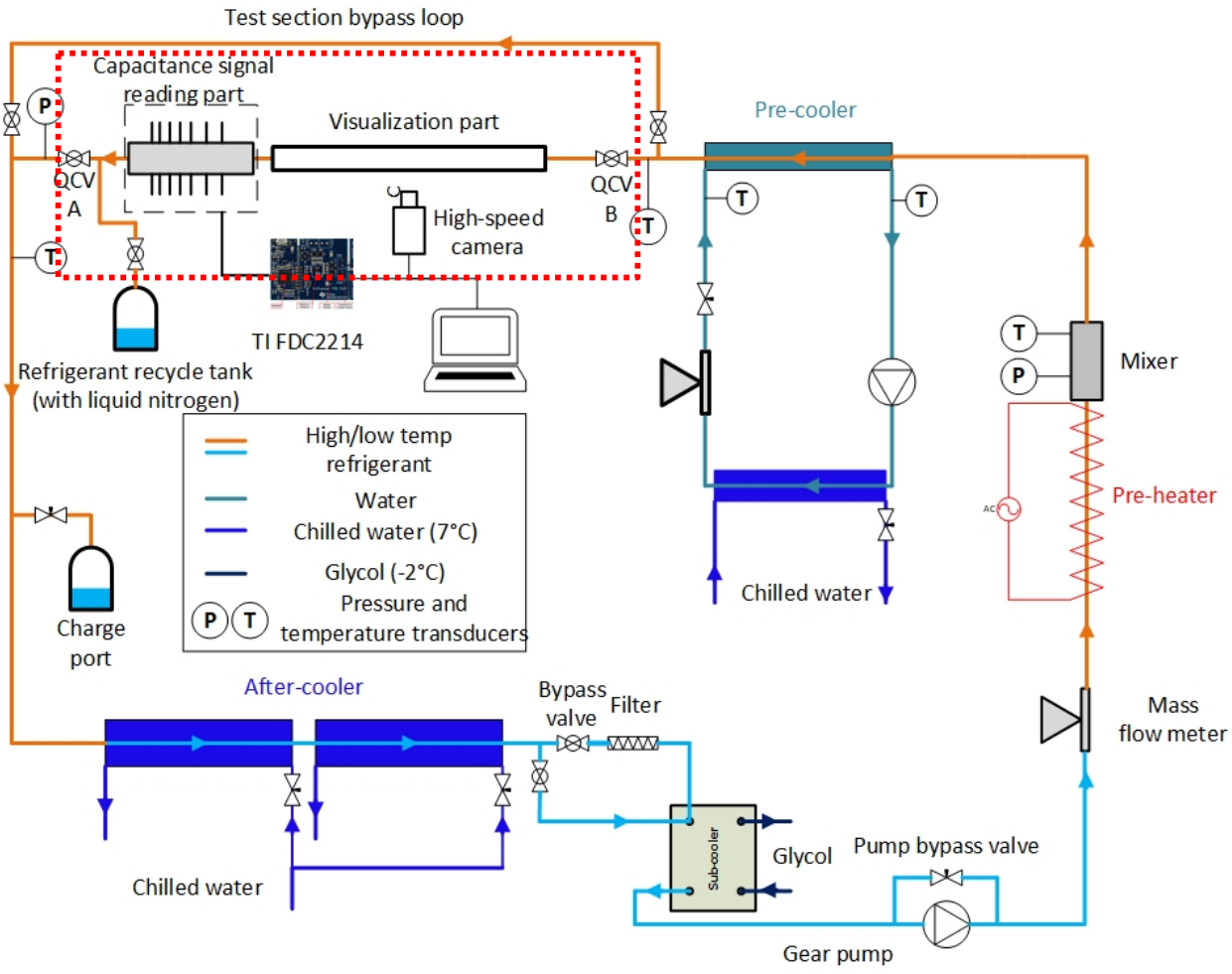

Figure 32 Schematic drawing of experimental facility, test section in red box

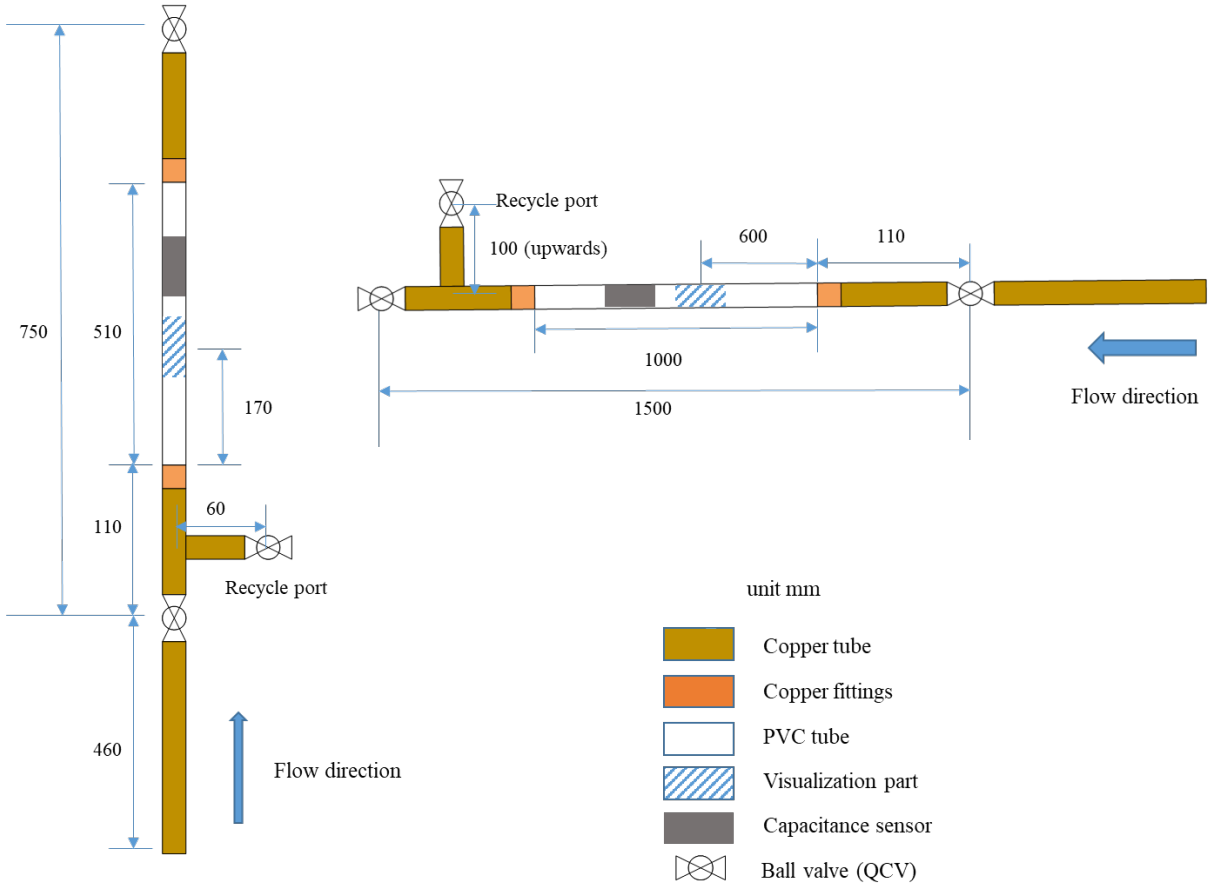

Figure 33 Schematic drawing of the test section, horizontal and vertical

4.3 Experimental procedure and conditions

- Set up certain mass flux by controlling the gear pump speed with VFD.
- Superheat refrigerant with the electric heater. The superheat of refrigerant in the mixer is maintained at approximately 5 K to guarantee the refrigerant is in vapor phase. Bulk enthalpy of refrigerant is then determined.
- The pre-cooler is then used to cool the refrigerant into a desired vapor quality condition before the test section.
- The temperature in the test section is set at 33 ºC. The saturation temperature is set by the temperature of the water bath of the charge port.
- After the system becoming stable, capacitance signals are first recorded. Then get video footage from high-speed camera and refrigerant retention with quick closing valves (ball valve A and B) and liquid nitrogen recovery.

Table 7 lists the experimental conditions. Void fraction measurement and flow regime visualization is shown in Chapter 2.6.

Table 7 experimental conditions

Working media	R134a
T_r	33 ºC
Test section orientation	Horizontal and vertical
Test section length	Horizontal: 1500mm (~214 diameters) Vertical: 750mm (~107 diameters)
Mass flux	Horizontal: 40, 80 and 115 kg/m^{2}s Vertical: 65, 80 and 115 kg/m^{2}s
Quality	0.05-0.9

4.4 Data reduction and uncertainty

The data reduction and uncertainty analyses for void fraction results are discussed in Chapter 2.5.

For every test condition, the time-averaged capacitance signals are read by FDC2214EVM in pF. Before each set of experiments was conducted, capacitance signals for two base points are measured. The first is the capacitance signals for full vapor phase (C_{Vapor}) in the test section and the second is full liquid phase (C_{Liquid}). C_{Liquid} is obtained at 33 ºC. Some researchs [48, 55] shows dielectric constant of refrigerant vapor phase is not dependent on temperature. Hence, C_{Vapor} is measured at room temperature. After the two base points are measured, the capacitance signals for other test conditions ($C_{measured}$) is obtained. Normalized capacitance is then defined as following:

$$C_{norm} = \frac{C_{measured} - C_{Vapor}}{C_{Liquid} - C_{Vapor}} \tag{33}$$

The denominator which is assumed constant for the duration of the one set of experiments shows the entire range of the one set of experiments and the numerator shows the signals is how much larger than the full vapor condition. Hence, the normalized signals are typically from 0 to 1. Though C_{Liquid} and C_{Vapor} may shift among different sets of experiments, the difference between C_{Liquid} and C_{Vapor} (ΔC_{L-V}) keeps quite constant with little fluctuations as the temperature keeps constant in this study. De Kerpel et al. [42] proposed that normalized calibration curves would not be affected if ΔC_{L-V} remained the same. ΔC_{L-V} of horizontal and vertical configurations for different axial length of electrodes is listed in Table 8.

Table 8 ΔC_{L-V} of horizontal and vertical configurations for different axial lengths of electrodes in pF

	D/2	2D/3	D
Horizontal	1.118583304±0.057	1.224118491±0.05	1.797160123±0.069
Vertical	1.318990399±0.011	1.362913213±0.017	1.85315114±0.01

4.5 Horizontal flows

4.5.1 Capacitive signal characteristics for horizontal flow patterns

Flow regimes classification and void fraction results were obtained in Chapter 2.6. In this section, typical flow patterns for horizontal flows and corresponding capacitance signals will be discussed. Visualization and classification of flow regimes in shown in Figure 34. Flow regimes for mass flux from 40 to 150 kg/m^{2}s are shown. Mass flux of 150 kg/m^{2}s is to show the trend of flow patterns developing and not tested in this study. Data are drawn in three geometries which represent different flow patterns: Δ-slug flow, □-stratified-wavy flow and ◊-annular flow. Capacitive signals for mass flux of 80 kg/m^{2}s condition is discussed. For the other two mass flux conditions, the results are similar only with different flow pattern transition vapor qualities.

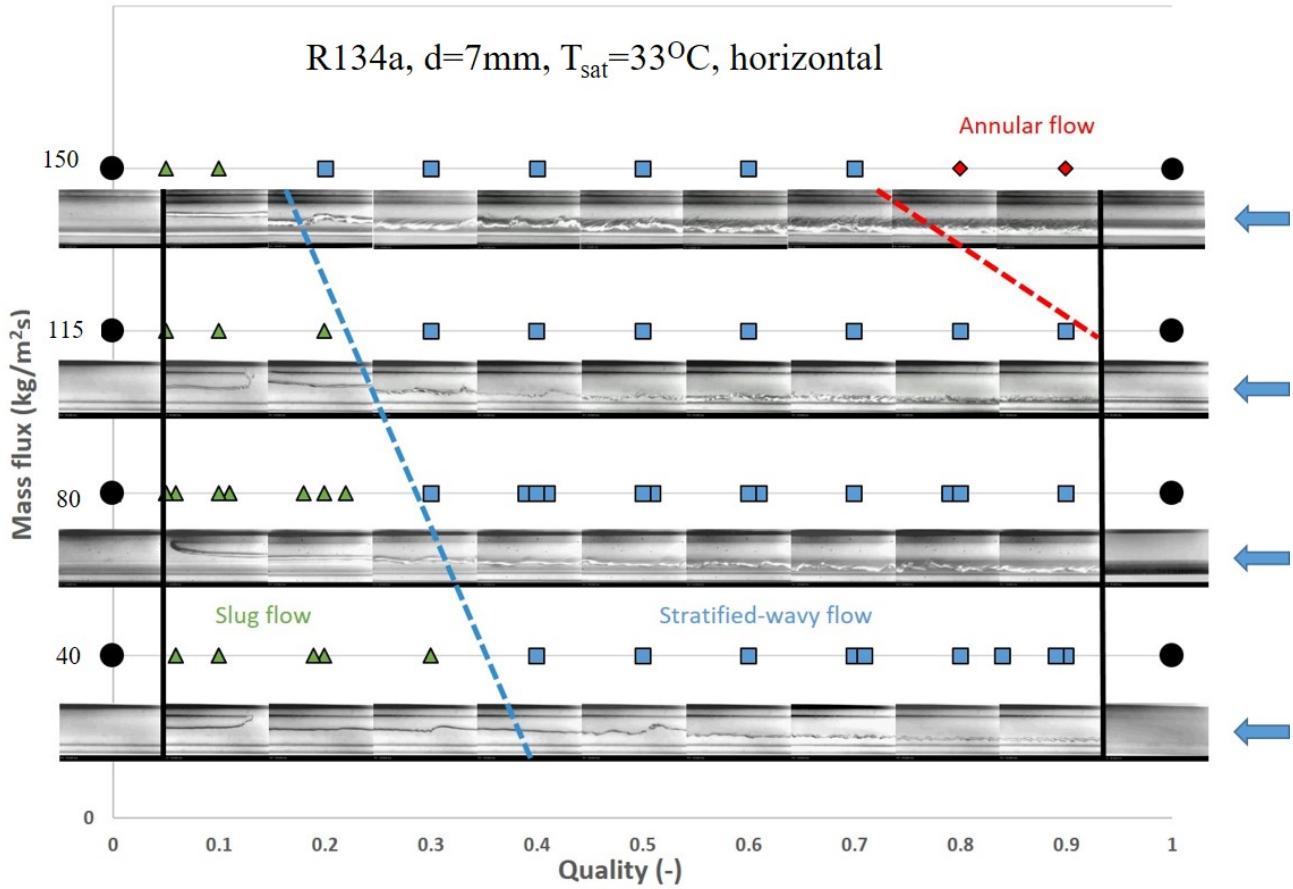

Figure 34 Visualization and classification of flow regimes for horizontal flow

Visualization and full signal map for horizontal flow with mass flux equals 80 kg/m^{2}s are shown in Figure 35 and Figure 36. For this mass flux, two major flow patterns are observed: slug flow (quality from 0.1 to 0.2) and stratified-wavy (quality from 0.3 to 0.9) flow. Visualization results show that vapor slugs which are usually near the top of tubes appear at relatively low qualities zone. As the vapor quality increases, more vapor slugs appears with higher frequency. The length of liquid bridges between vapor slugs becomes smaller. When the vapor quality comes around 0.3, liquid bridges break down and the liquid and vapor interface which is very wavy appears in the middle. The interface has a trend of becoming smoother as the quality increases. When the quality equals to one, nearly no liquid refrigerant appears in the test section. In Figure 35, slug flow patterns are in the red box and stratified-wavy flow patterns are in the blue box. In Figure 36, the full signal map (Normalized signals vs. time) with qualities from 0 to 1 is shown. Following results can be obtained with this map:

The value of normalized time-averaged signals decreases as vapor qualities increase. This is because the dielectric constant of liquid phase is bigger than that of vapor phase. As the vapor qualities increase, more vapor appears in the cross-sectional area, which results in smaller averaged signals.

In this map, basically two signal patterns (in the red box and the blue one) can be distinguished. The signals in the red box have the large oscillation amplitude and concentrate at two major levels: the top and the middle. The singles in the blue box have smaller oscillation amplitude. They are more stable and oscillates at one major level. The two signal patterns are exactly corresponding to the two flow regimes observed in the visualization results. Characteristics for slug flow and stratified-wavy flow is going to be discussed.

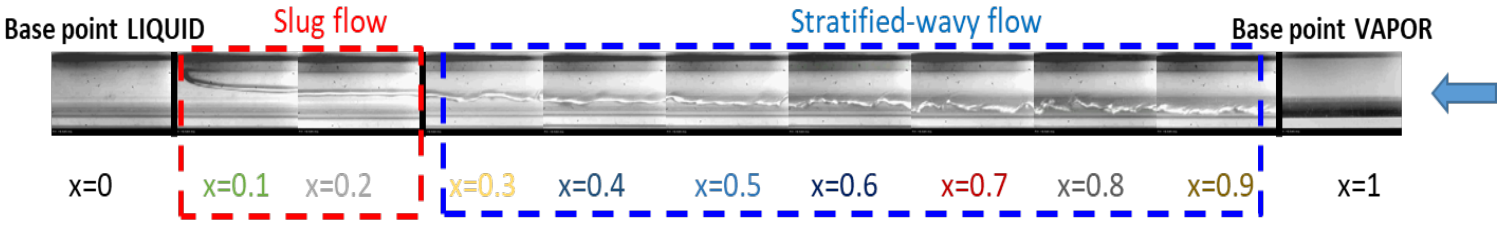

Figure 35 Visualization for horizontal flow with mass flux = 80 kg/m^{2}s

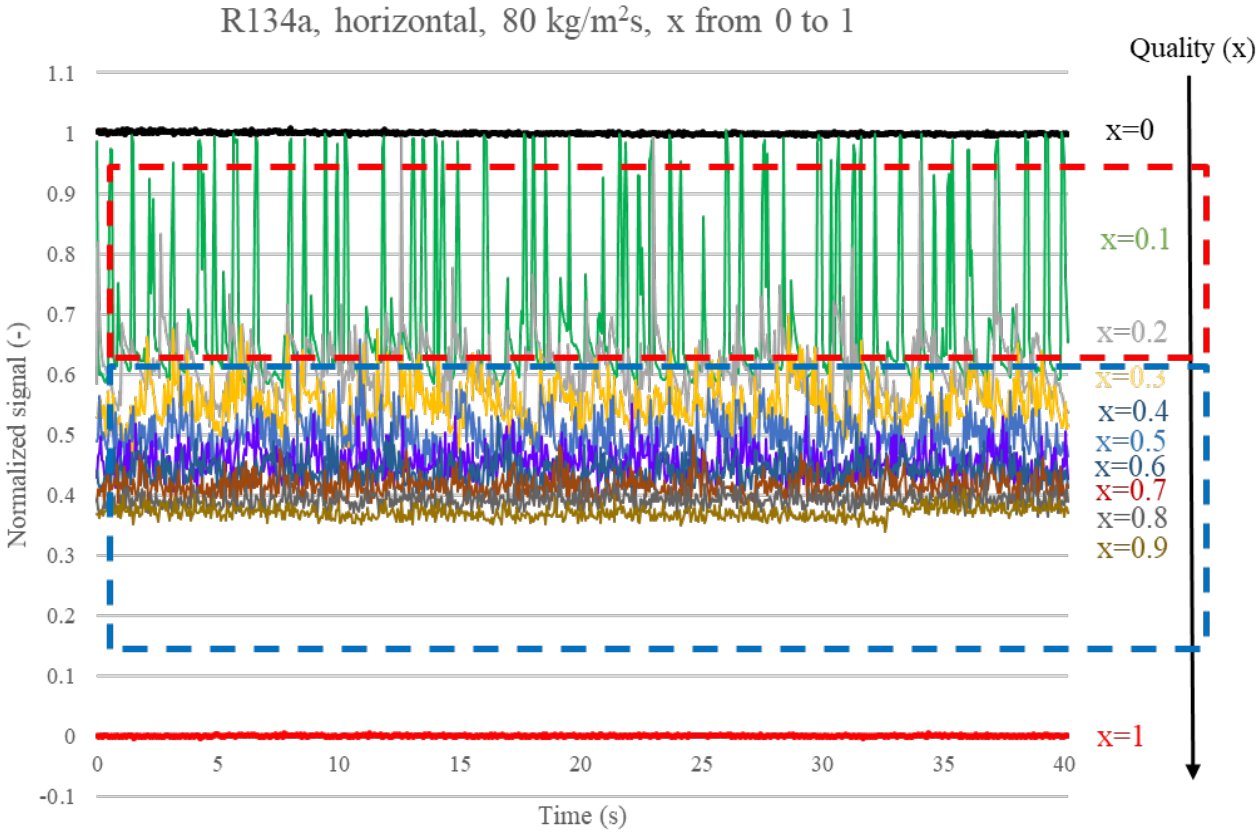

Figure 36 Full signal map for quality from 0 to 1 for mass flux = 80 kg/m^{2}s

Slug flow

Figure 37 shows the normalized signals of the flow with quality equals to 0.1. The signals concentrate at two major levels: one at the top and the other one in the middle. When the liquid bridges come into the sensor (liquid phase is filled in the entire cross-sectional area), the singles jumps to 1. When vapor slugs come into the sensor, the signals stay at the lower level. Figure 38 shows the PDE for x=0.1. Two peaks which represent dominant signal values are shown in this diagram. The first one is around one and the second is around 0.65. Hence, for slug flows for horizontal configuration, the normalized capacitive signals show two major concentration with large oscillation amplitude: one is near one and the other near 0.6.

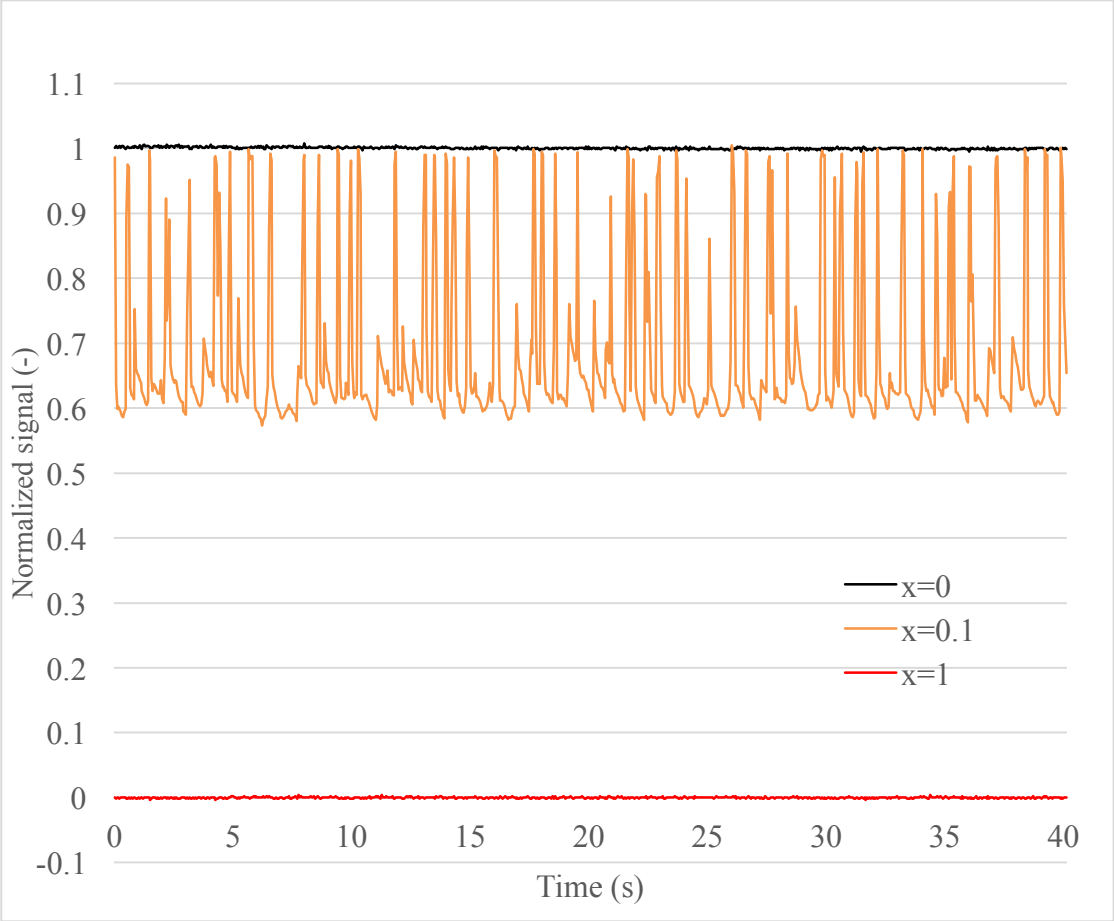

Figure 37 Normalized signals for x=0.1 and two base points

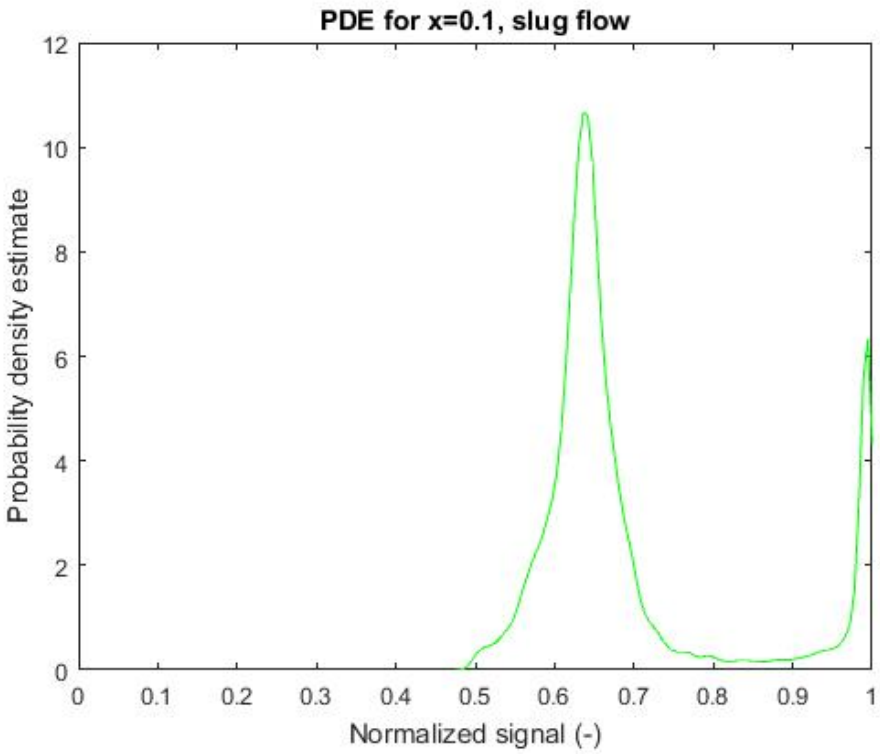

Figure 38 PDE for x=0.1

Stratified-wavy flow

Figure 39 shows the normalized signals of the flow with quality equals to 0.5. Unlike the signals for x=0.1, they only concentrate at one major level. Signals fluctuate at a relatively stable state and no huge oscillations are observed. For stratified-wavy flow in the visualization results, the interface between liquid phase and vapor phase is relatively constant with periodic waves. Figure 40 shows the PDE for x=0.5. Only one peak which represents dominant signal values is shown in this diagram. Hence, for stratified-wavy flows for horizontal configuration, the normalized capacitive signals show one major concentration with small oscillation amplitude.

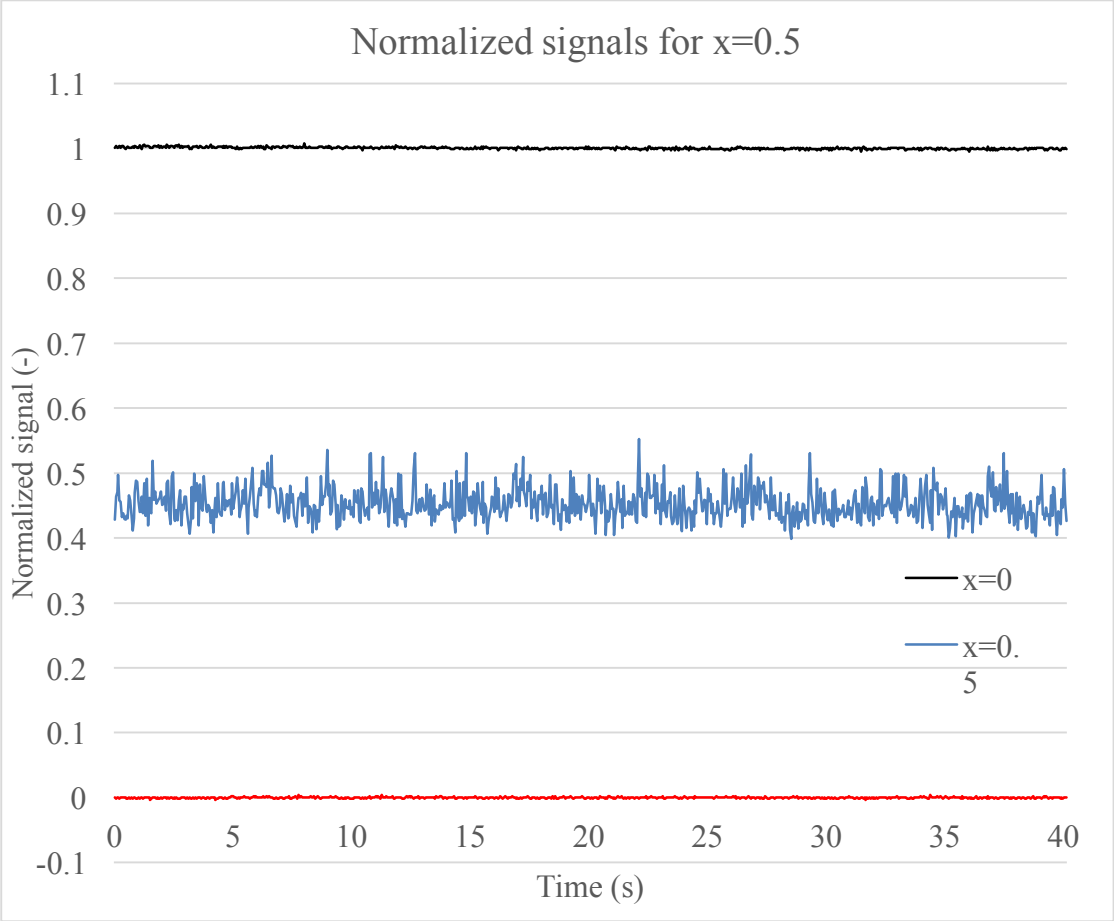

Figure 39 Normalized signals for x=0.5 and two base points

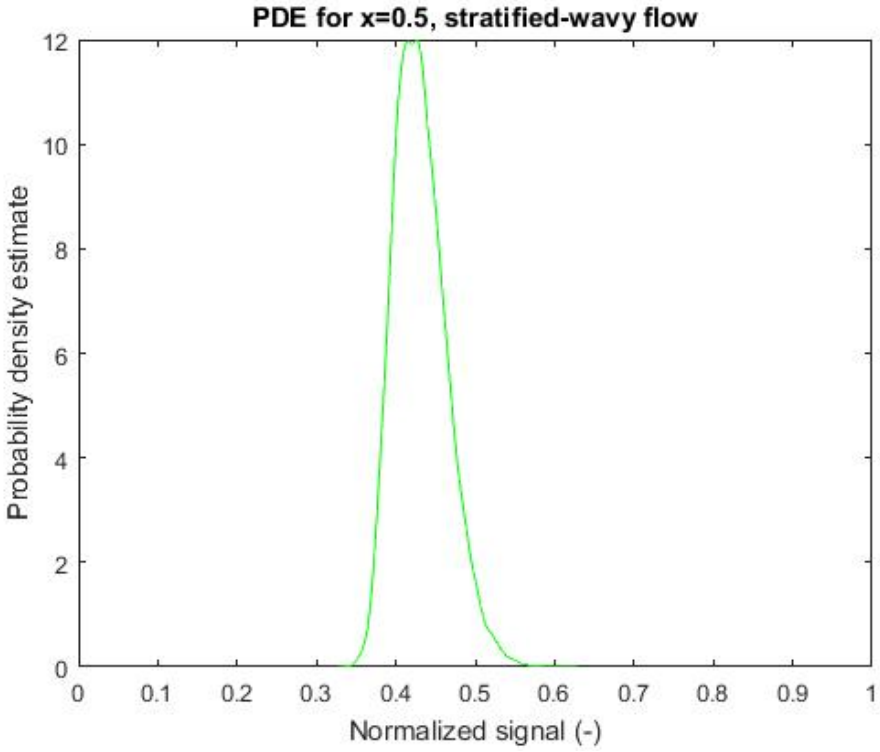

Figure 40 PDE for x=0.5

Conclusions

In this mass flux range (40-115 kg/m^{2}s) for horizontal flows, two major flow patterns are observed: slug flow and stratified-wavy flow. With the capacitive signals, different flow patterns can be characterized by normalized signals and PDE. Flow patterns can be more complicated out of this mass flux range and more statistical signal analysis is need to be proposed in further studies.

4.5.2 Comparison between signals obtained from electrodes with different length for horizontal flows

No open literature uses smaller sensors with two-concave-plate configuration and compare the signal among electrodes with different lengths. The sensors can be utilized in many other applications where the space is limited if sensors with smaller electrodes can work as functionally as ones with longer electrodes. For example, void fraction along headers in microchannel heat exchangers acts a crucial role in refrigerant charge prediction and refrigerant misdistribution improvement. Capacitance sensors can then be used between tubes along headers to measure local void fraction. In this section, capacitive signals from three pairs of electrodes with different axial

length of one inner diameter (D), 2D/3 and D/2 are tested. Both flow regime characterization and void fraction measure measurements are compared among the electrodes.

Flow pattern characterization comparison

Figure 41 and Figure 42 show the signals comparison among electrodes with different axial length. Two vapor quality conditions (x=0.1-slug flow and x=0.5-stratified-wavy flow) are shown here and the comparison results are similar to signals of other qualities. In both conditions, all of the three pairs of electrodes can show the similar patterns. For x=0.1 (slug flow), all of the three series of signals show two major concentrations: one is near the unity and the other is in the middle. As discussed before, this signal pattern characterizes the vapor slugs and liquid bridges passing through the sensor, which are characteristics belong to slug flows. For x=0.5 (stratified-wavy flow), all the series of signals have a smaller oscillation amplitude and only one concentration level. This signal pattern is the characteristics of stratified-wavy flows. Hence, the three pairs of electrodes with different axial lengths can characterize flow regimes in this mass flux range.

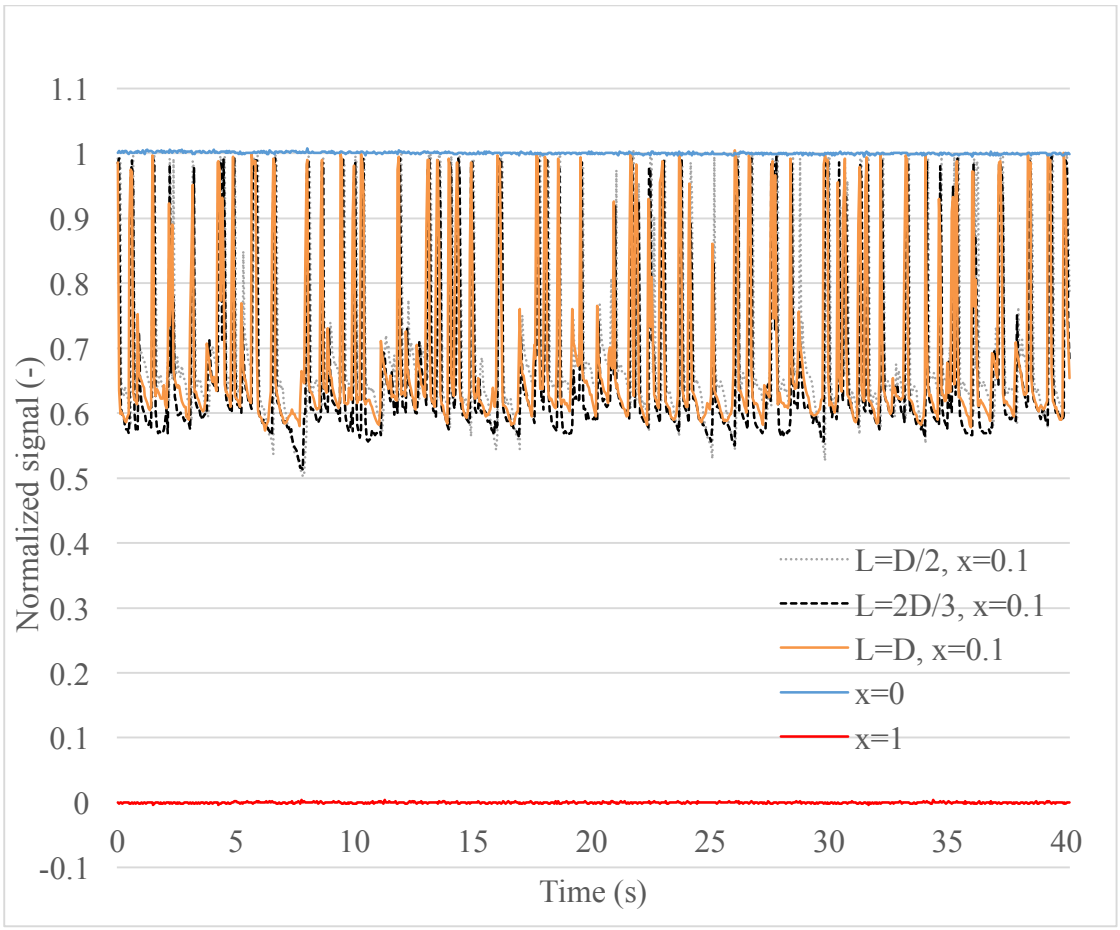

Figure 41 Capacitive signals of electrodes with different axial length for x=0.1 (slug flow)

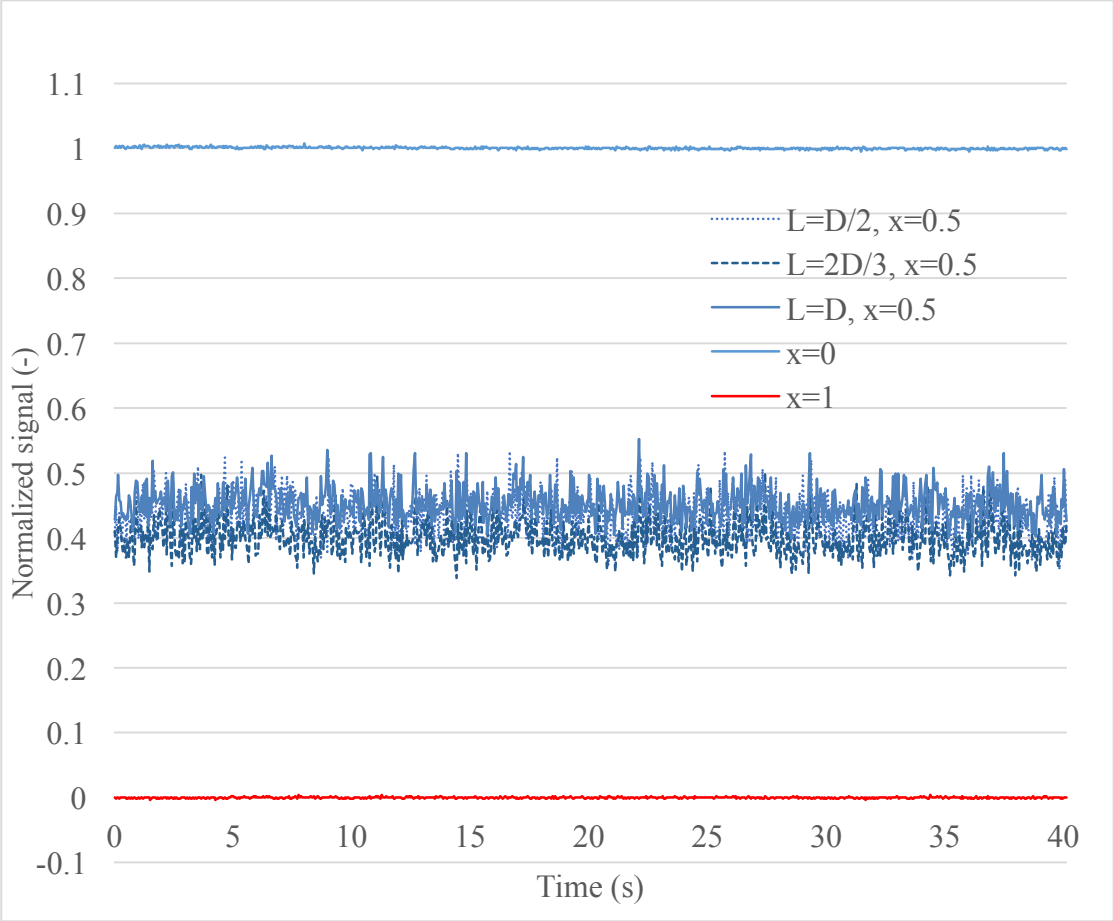

Figure 42 Capacitive signals of electrodes with different axial length for x=0.5 (stratified-wavy flow)

Void fraction calibration and measurement comparison

Figure 43 through Figure 45 show the comparison of signals obtained from electrodes with different axial length corresponding to the measured void fraction. All the three mass flux conditions are compared. Three series of signals have the same trend. When the electrodes with different axial lengths measure the same void fraction and flow regime, the values of normalized time-averaged single are nearly the same among these three pairs of electrodes. The signal values from electrodes with length of D/2 is overlapping those of D. However, the signal valves of electrodes with length of 2D/3 is a little bit smaller than those from the other two pairs. This may due to the configuration of the electrodes or instrumental errors. The pair of electrodes with 2D/3 axial length locates in the middle, where more guarding electrodes that are connected to the ground are on both sides. This may reduce the values of signals.

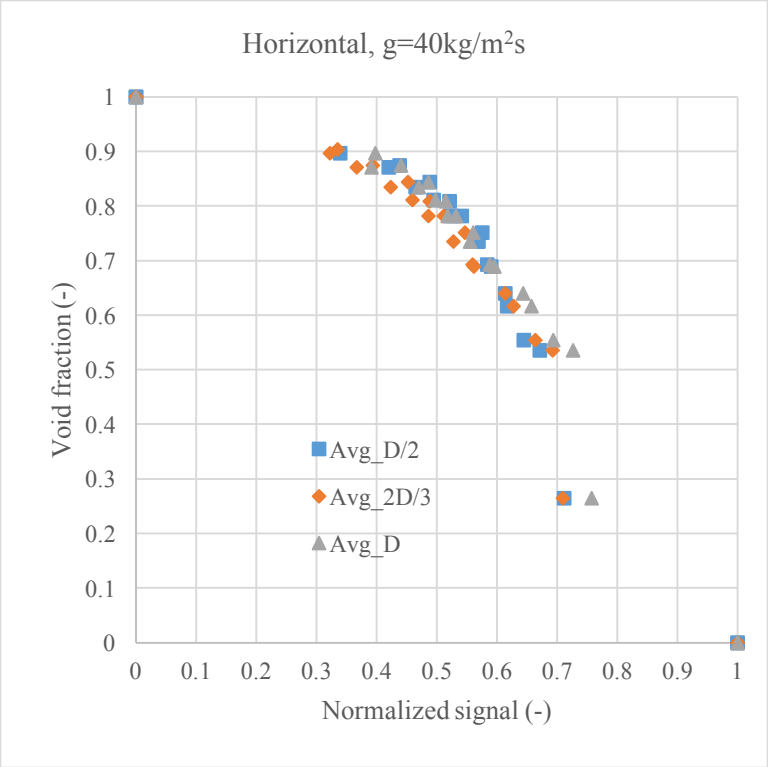

Figure 43 Signal comparison between electrodes widths: D/2, 2D/3, D (Horizontal, g=40kg/m2s)

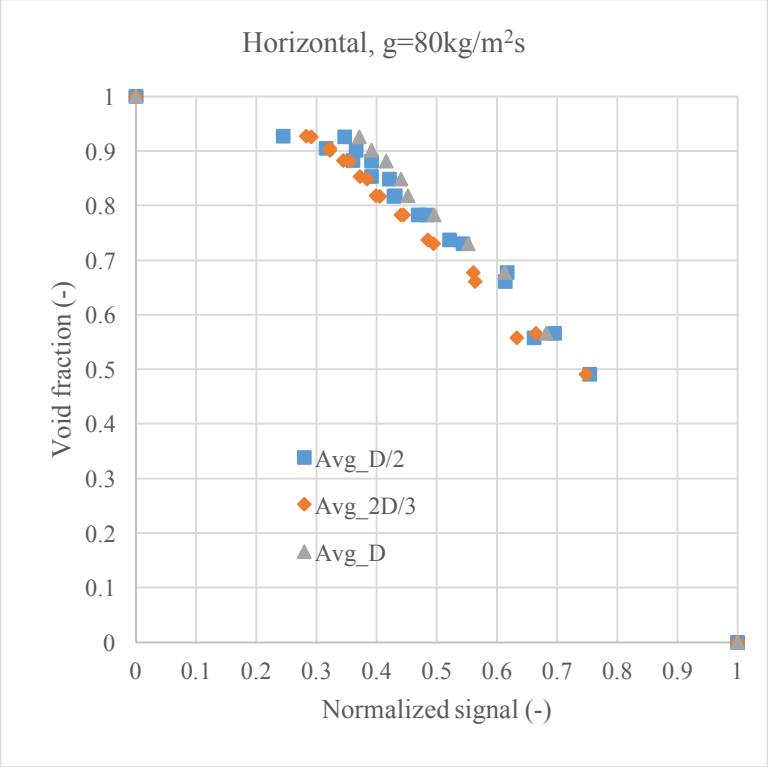

Figure 44 Signal comparison between electrodes widths: D/2, 2D/3, D (Horizontal, g=80kg/m2s)

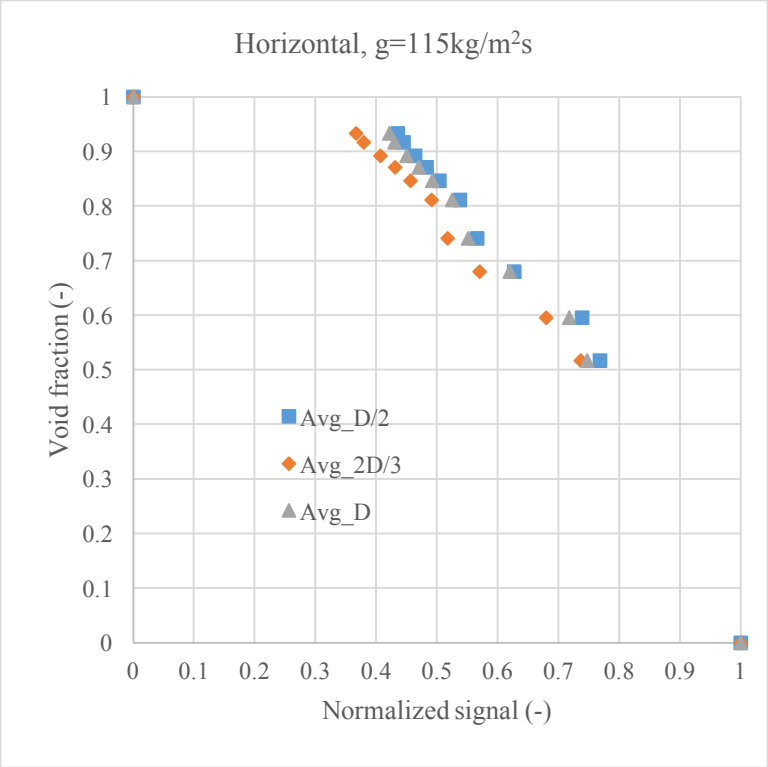

Figure 45 Signal comparison between electrodes widths: D/2, 2D/3, D (Horizontal, g=115kg/m2s)

Conclusions

From the discussion above, both flow patterns characterization and void fraction measurement are compared among the series of signals from three pairs of electrodes with different axial lengths. The results shows that for horizontal configuration and in this mass flux range, the signals don't depend on the axial length of electrodes. Hence, narrower electrodes can be used.

4.5.3 Calibrated correlations for void fraction measurement in horizontal tubes

Due to the non-uniform electric field between two electrodes, the capacitive signals are dependent on both void fraction and phase distribution. Hence, the correlation between time-averaged signals and void fraction are not linear. To measure refrigerant two-phase flow void fraction, the capacitance senosr must be calibrated first.

In this study, quick closing valves are used to get void fraction results. The calibration curve show the relation between normalized capacitive signal and void fraction for horizontal flow in this mass flux range. Figure 46 shows the calibrated curve for horizontal flows at low mass flux. Two flow pattern regions and three mass flux are included in this map. With this curve, sensors with the same

configuration can be utilized to measure void fraction in horizontal flows with R134a in this mass flux range.

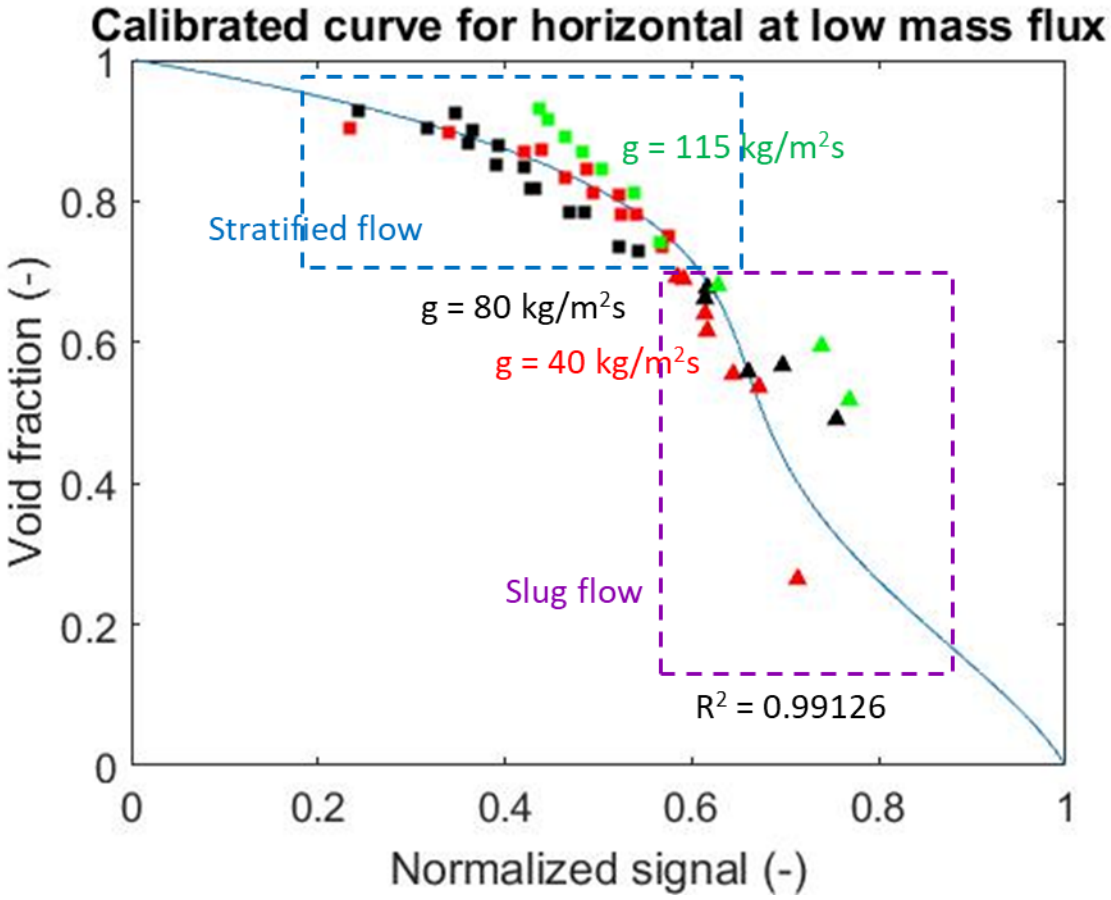

Figure 46 Calibrated curve for horizontal flow at low mass flux

4.6 Vertical flows

4.6.1 Capacitive signal characteristics for vertical flow patterns

Flow regimes classification and void fraction results for vertical flows were obtained in Chapter 2.6. In this section, typical flow patterns for upwards vertical flows and corresponding capacitance signals will be discussed. Visualization and classification of flow regimes is shown in Figure 47. Flow regimes for mass flux from 65 to 115 kg/m^{2}s are shown. Data are drawn in three geometries which represent different flow patterns: Δ-slug flow, □-churn flow and ◊-annular flow. Capacitive signals for mass flux of 80 kg/m^{2}s condition is discussed. For the other two mass flux conditions, the results are similar only with different flow pattern transition vapor qualities.

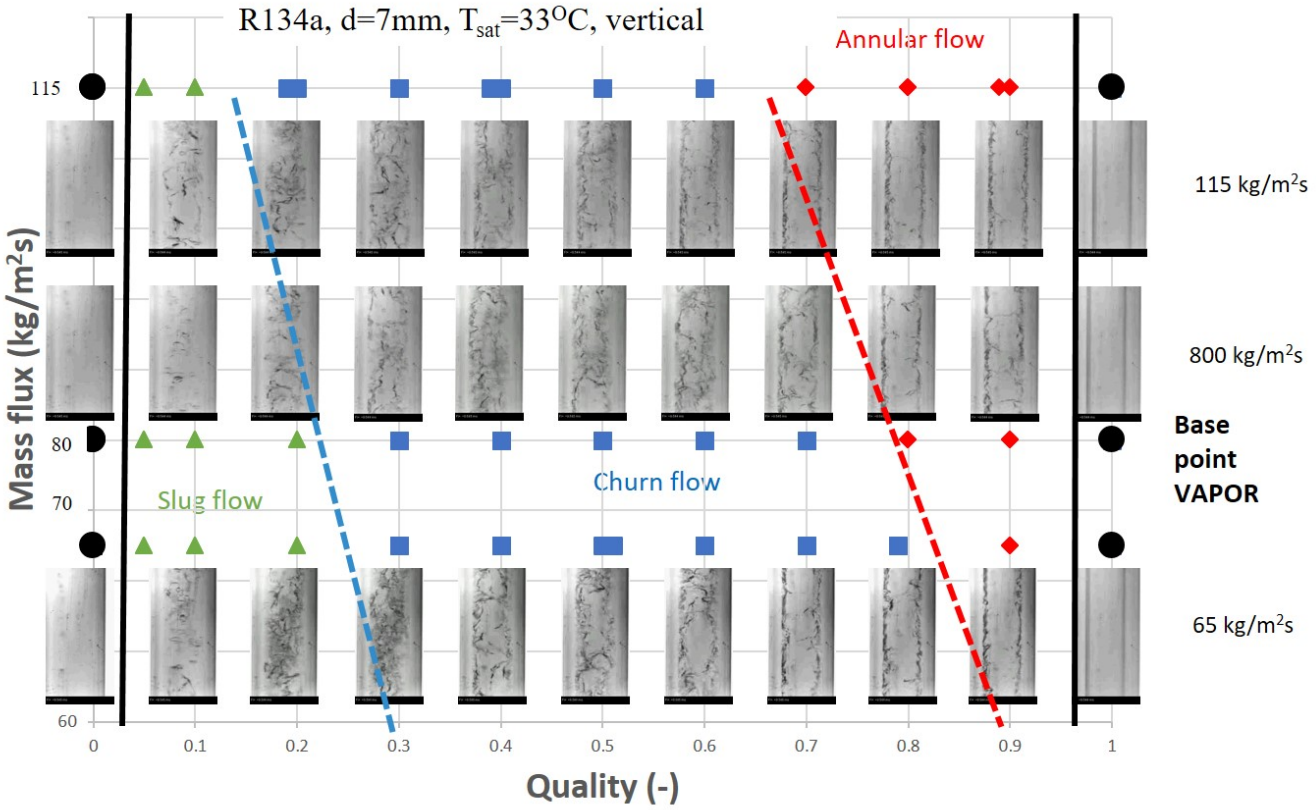

Figure 47 Visualization and classification of flow regimes for horizontal flow

Visualization and full signal map for upwards vertical flow with mass flux = 80 kg/m^{2}s are shown in Figure 48 and Figure 49. In this mass flux range, three major flow patterns are observed: slug flow (quality from 0.1 to 0.2), churn flow (quality from 0.3 to 0.7) and annular flow (quality from 0.8 to 0.9) flow. Visualization results show that vapor slugs appear at relatively low qualities zone. Different from slug flows in horizontal tubes, the vapor slugs concentrate in the middle of tubes. This is because that the direction of gravity relative to the flows is different. When the vapor quality comes around 0.3, the liquid bridges between vapor slugs break down. The flow pattern becomes more chaotic and the interface gets more blurry. It can be seen that liquid goes up and then sometimes down. When the test condition approaches to higher vapor qualities, the flow pattern becomes more stable. Vapor flows in the central core of the tube with liquid along the wall. As the vapor quality increases to one, no liquid appears in the test section. In Figure 48, three different colored boxed separate these three flow patterns from observation. In Figure 49, the full signal

map (Normalized signal vs. time) with qualities from 0 to 1 is shown. Following results can be obtained with this map:

Similar to the horizontal configuration, the value of normalized time-averaged signals decreases as vapor qualities increase.

In this map, three signal pattern can be distinguished. The signals in the red box have the large oscillation amplitude and concentrate at two major levels: the top and the middle. The singles in the brown box have much smaller oscillation amplitude. They are more stable and oscillates at one major level. For the signals in the blue box, though oscillate at one major level, the amplitude is bigger than that of signals in the brown box. The three signal patterns are exactly corresponding to the three flow regimes observed in the visualization results. Characteristics for these three flow patterns are going to be discussed.

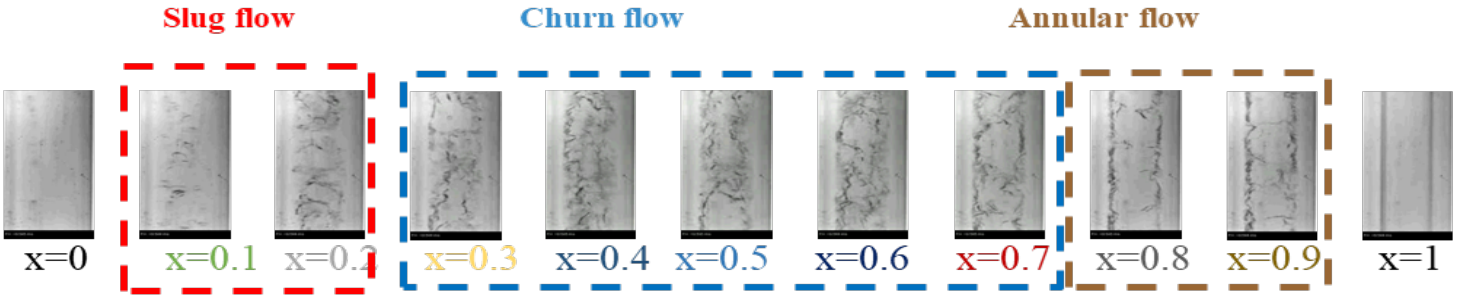

Figure 48 Visualization for upwards vertical flow with mass flux = 80 kg/m^{2}s

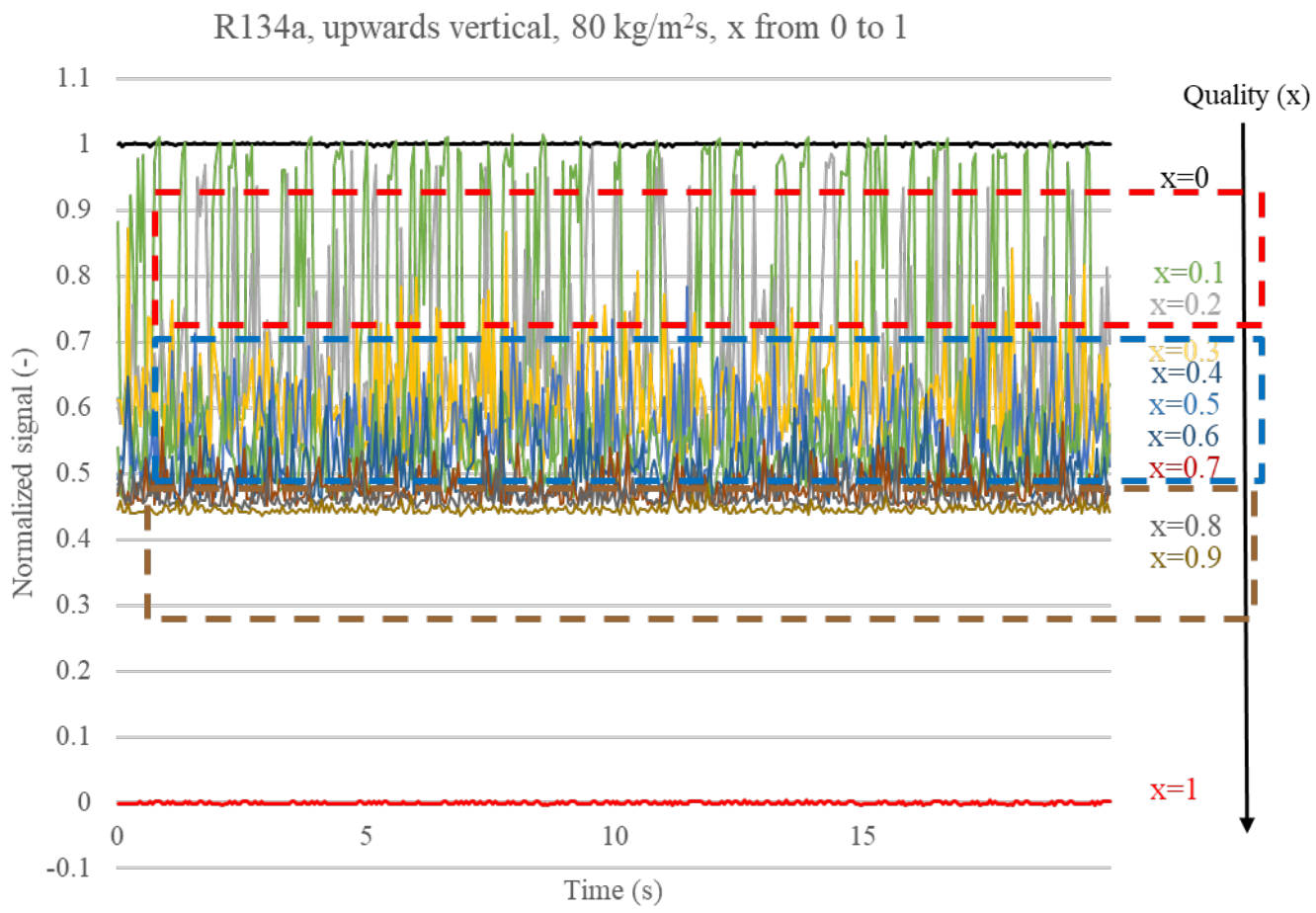

Figure 49 Full signal map for quality from 0 to 1 for mass flux = 80 kg/m^{2}s

Slug flow

Figure 50 shows the normalized signals of the flow with quality equals to 0.1. The signals concentrate at two major levels: one at the top and the other at the middle. This signal pattern is similar to that of slug flows in horizontal tubes. When the liquid bridges come into the sensor (liquid phase is filled in the entire cross-sectional area), the singles jumps to 1. When vapor slugs come into the sensor, the signals stay at the lower level. Figure 51 shows the PDE of signals for x=0.1. Two peaks which represent dominant signal values are shown in this diagram. The first one is around one and the second is around 0.55. This is the signal characterization of slug flows for upwards flows.

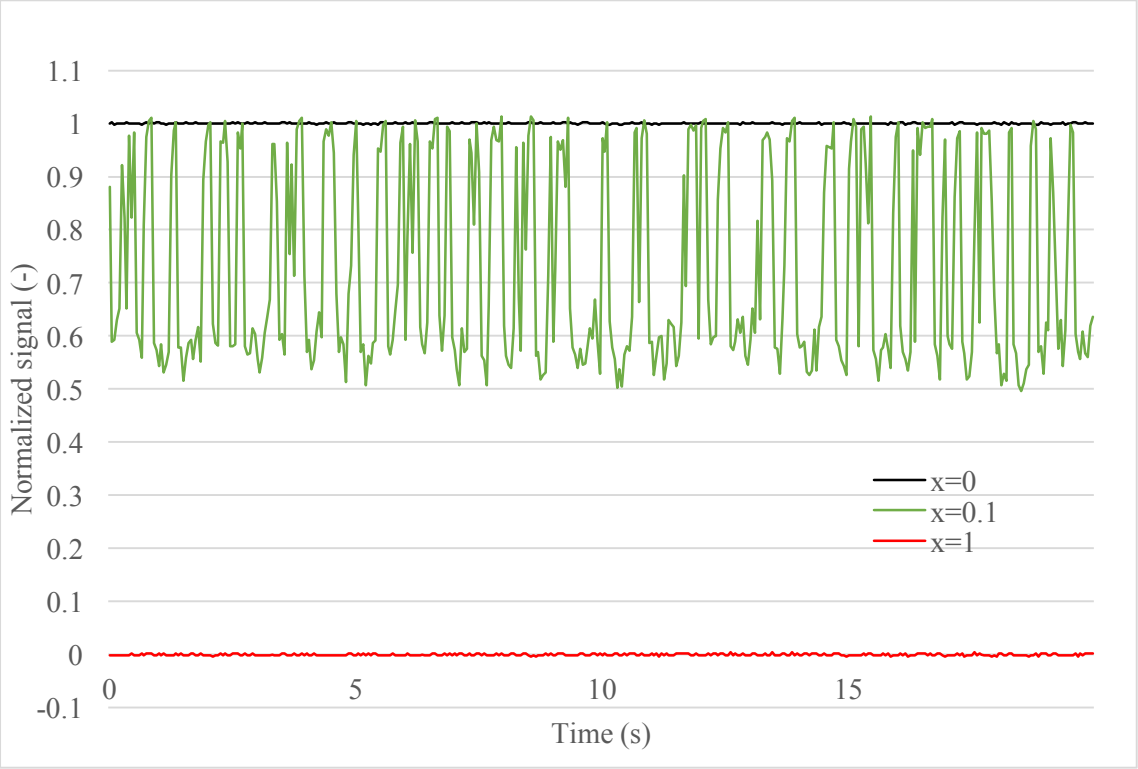

Figure 50 Normalized signals for x=0.1 and two base points

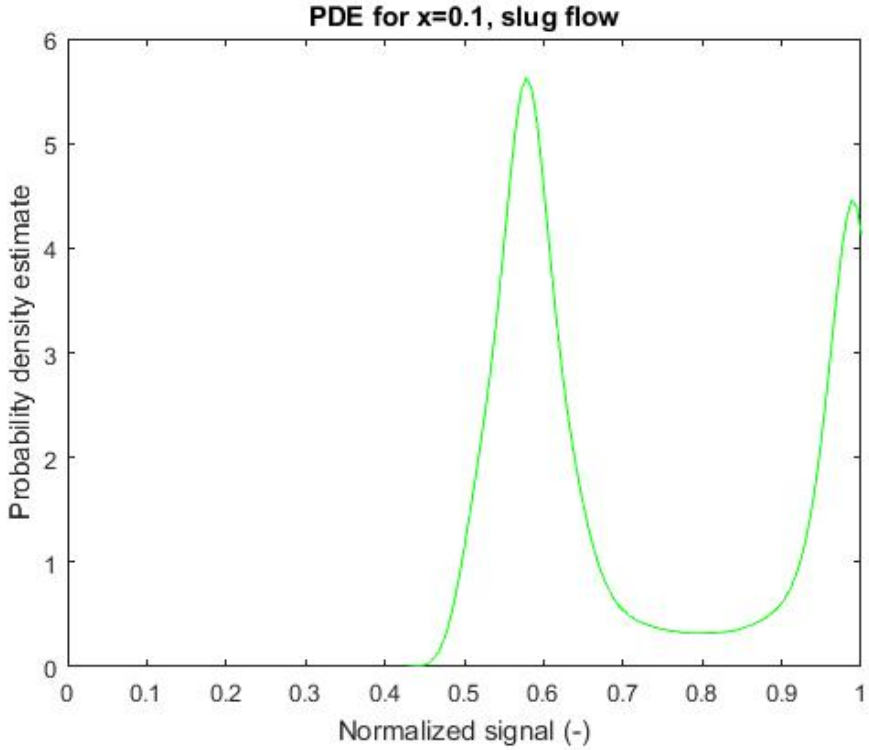

Figure 51 PDE for x=0.1

Annular flow

Figure 52 shows the normalized signals of the flow with quality equals to 0.8. Unlike the signals for x=0.1, they only concentrate at one major level. Signals fluctuate at a relatively stable state and no huge oscillations are observed. In the visualization results, liquid flows along the wall of tubes and vapor in the central core. No liquid bridges or huge waves are observed. Figure 53 shows the PDE for x=0.8. Only one peak which represents the dominant signal value is shown in this diagram. This peak has a very small span, which shows the possibility of signals appears around 0.45 is much higher than other ranges. This signal pattern is similar to that of stratified-wavy flow in horizontal tubes with smaller oscillations.

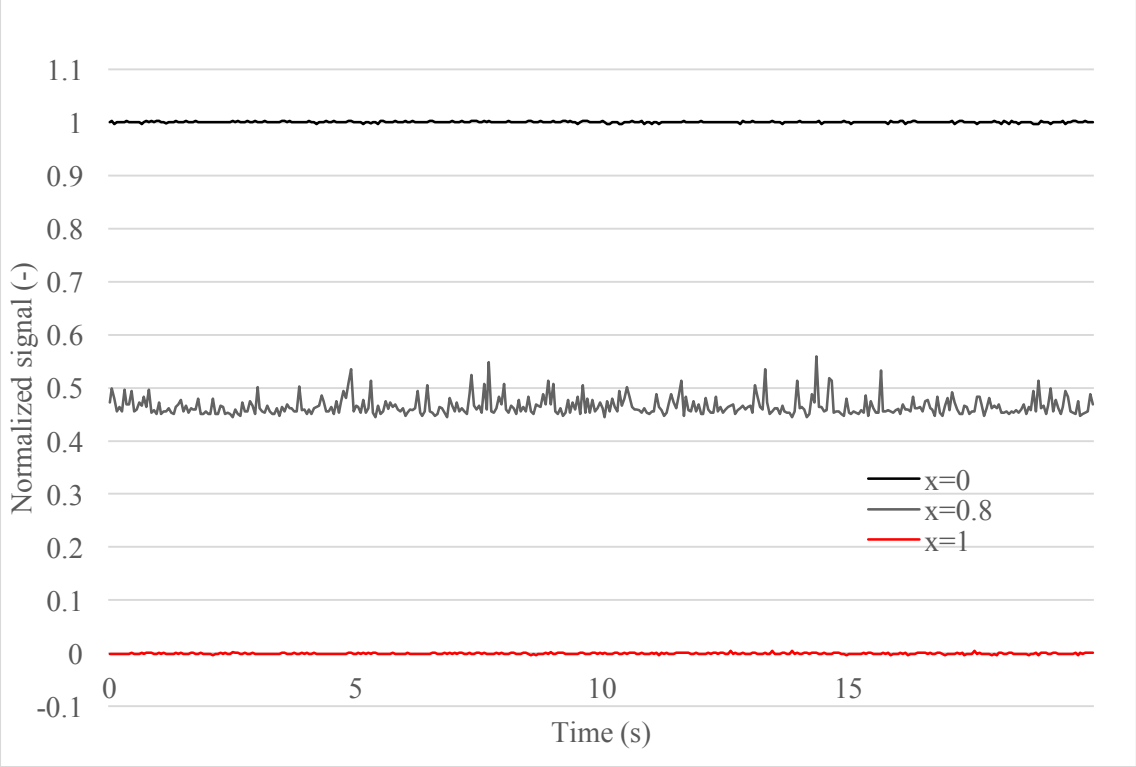

Figure 52 Normalized signals for x=0.8 and two base points

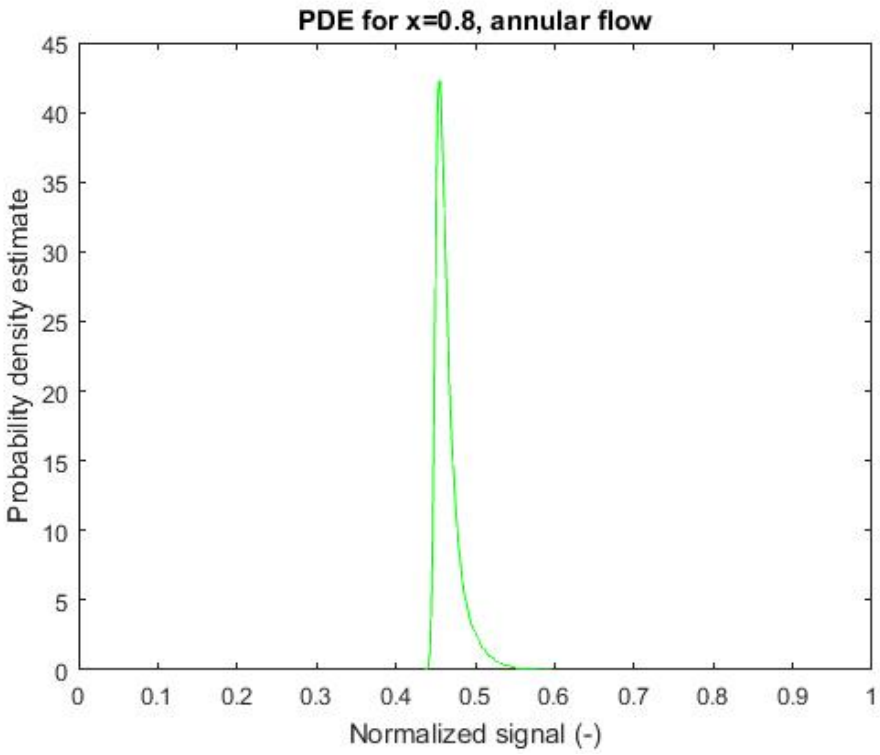

Figure 53 PDE for x=0.8

Churn flow

Figure 54 shows the normalized signals of the flow with quality equals to 0.4. The pattern which is the middle of slug flows and annular flows shows the transition characteristics. Compared with the signals of slug flows, this pattern does not oscillates at two major levels but one. However, it has large amplitude than that of annular flow. Figure 55 shows the PDE for x=0.4. Only one peak which represents dominant signal values is shown in this diagram. The span of the peak is bigger than that of annular flow, which show the possibility of signals appearing in a relatively large range around the 0.55.

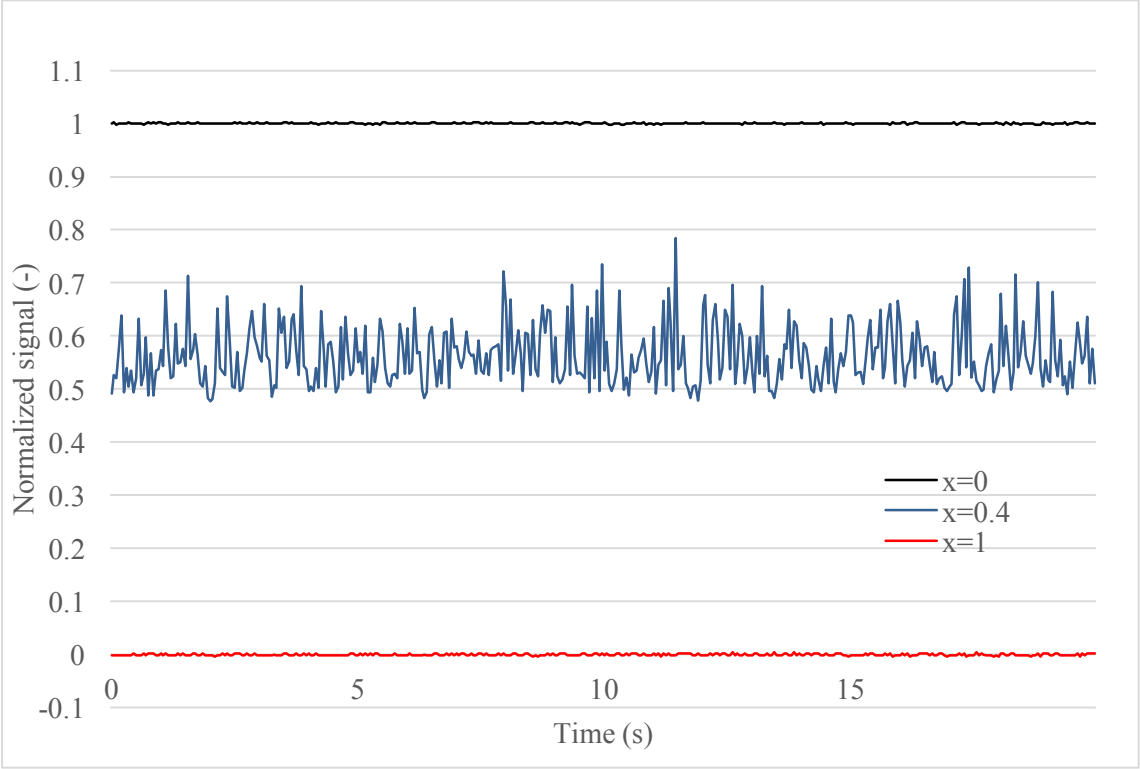

Figure 54 Normalized signals for x=0.4 and two base points

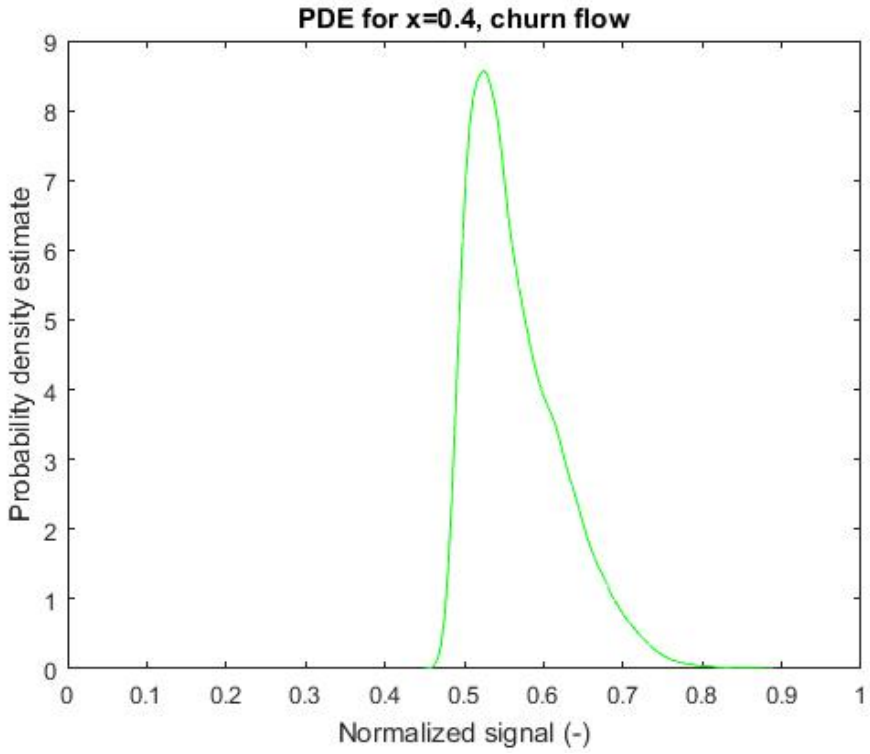

Figure 55 PDE for x=0.4

Conclusions

In this mass flux range for upwards vertical flows, three major flow patterns are observed: slug flow, churn flow and annular flow. With the capacitive signals, different flow patterns can be characterized by normalized signals and PDE. Flow patterns can be more complicated out of this mass flux range and more statistical signal analysis is need to be proposed in further studies.

4.6.2 Comparison between signals obtained from electrodes with different length for upwards vertical flows

Similar to horizontal configurations, the sensor must be calibrated before measuring void fraction due to the non-uniformity of electric fields. In this section, capacitive signals from three pairs of electrodes with different axial length of one inner diameter (D), 2D/3 and D/2 are tested. Both flow regime characterization and void fraction measure measurements are compared among the electrodes.

Flow pattern characterization comparison

Figure 56 through Figure 58 show the signals comparison among electrodes with different axial lengths. The signal patterns for three vapor qualities (x=0.1-slug flow, 0.4-churn flow and 0.8-annular flow) are compared. The signal patterns of electrodes with different axial lengths are similar for these three vapor qualities. For x=0.1 (slug flow), all of the three series of signals show two major concentrations: one is near the unity and the other is in the middle. As discussed before, this signal pattern characterizes the vapor slugs and liquid bridges passing through the sensor, which are characteristics belong to slug flows. For x=0.4 (churn flow) and x=0.8 (annular flow), all the series of signals only have one concentration level. Though the capacitive signals of electrodes with axial length of 2D/3 have smaller value, the pattern keeps constant among others. Hence, the three pairs of electrodes with different axial lengths can characterize flow regimes in this mass flux range.

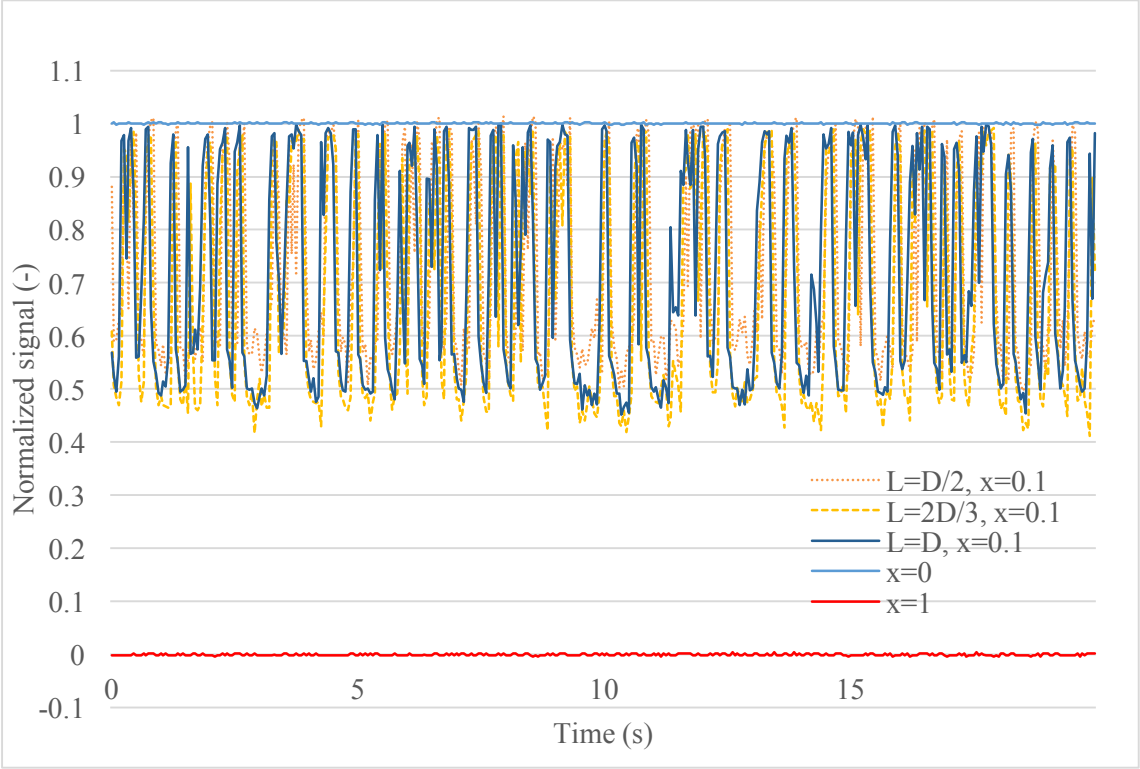

Figure 56 Capacitive signals of electrodes with different axial length for x=0.1 (slug flow)

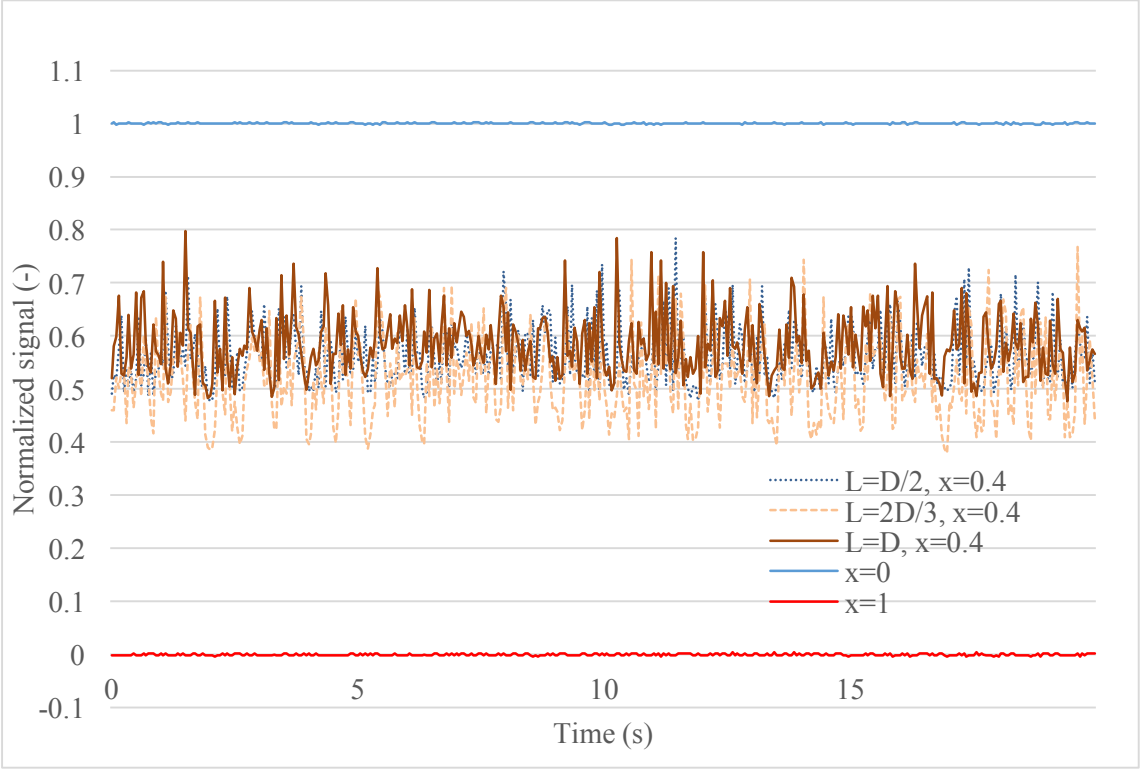

Figure 57 Capacitive signals of electrodes with different axial length for x=0.4 (churn flow)

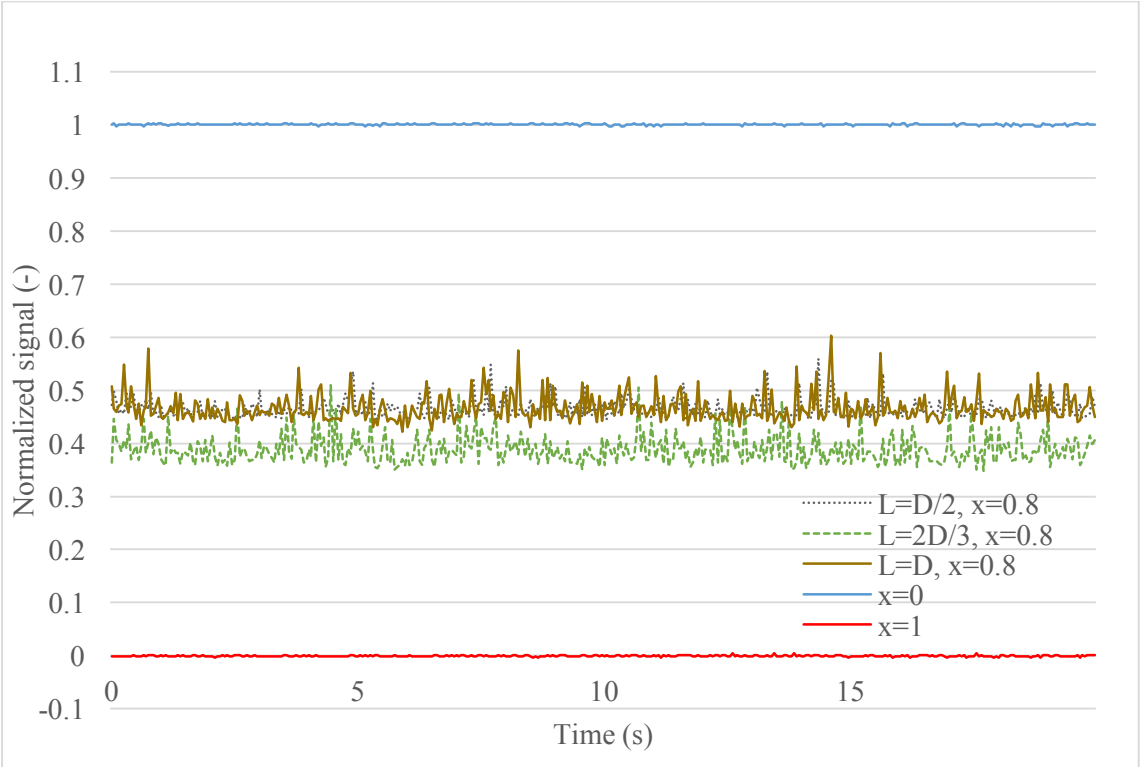

Figure 58 Capacitive signals of electrodes with different axial length for x=0.8 (annular flow)

Void fraction calibration and measurement comparison

Figure 59 through Figure 61 show the comparison of signals obtained from electrodes with different axial length corresponding to the measured void fraction. Three series of signals have the same trend. When the electrodes with different axial lengths measure the same void fraction and flow regime, the values of normalized time-averaged single are nearly the same among these three pairs of electrodes. The signal values from electrodes with length of D/2 is overlapping those of D. However, the signal valves of electrodes with length of 2D/3 is a little bit smaller than those from the other two pairs. This may due to the configuration of the electrodes and instrumental errors like wire connection. The pair of electrodes with 2D/3 axial length locates in the middle, where more guarding electrodes that are connected to the ground are on both sides. This may reduce the values of signals.

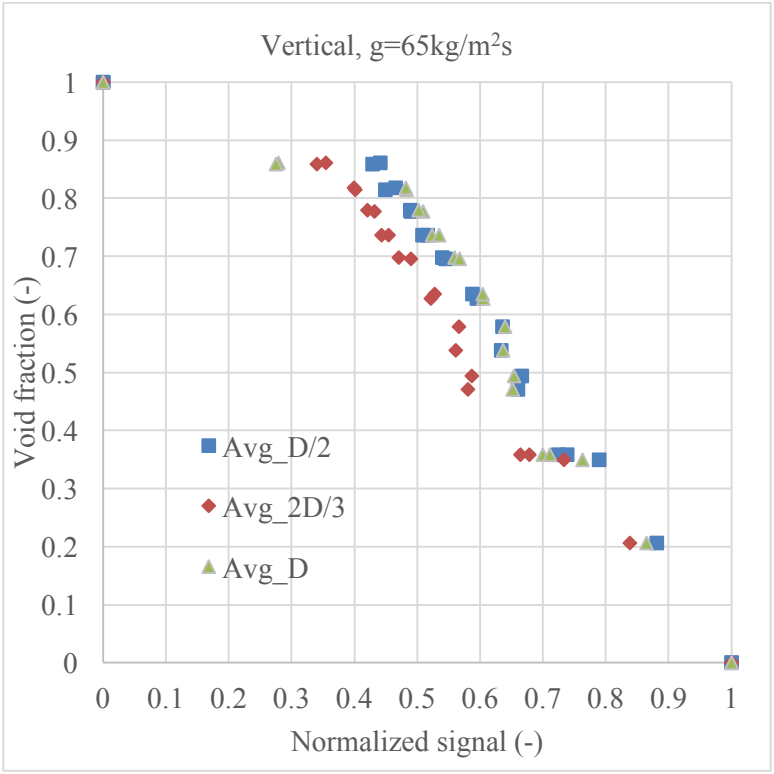

Figure 59 Signal comparison between electrodes widths: D/2, 2D/3, D (Vertical, g=65kg/m2s)

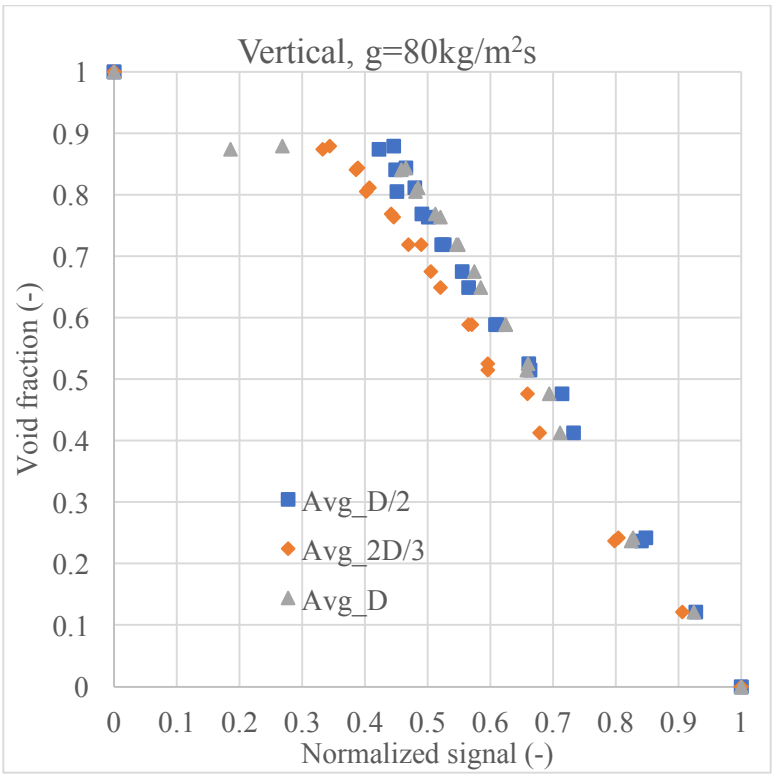

Figure 60 Signal comparison between electrodes widths: D/2, 2D/3, D (Vertical, g=80kg/m2s)

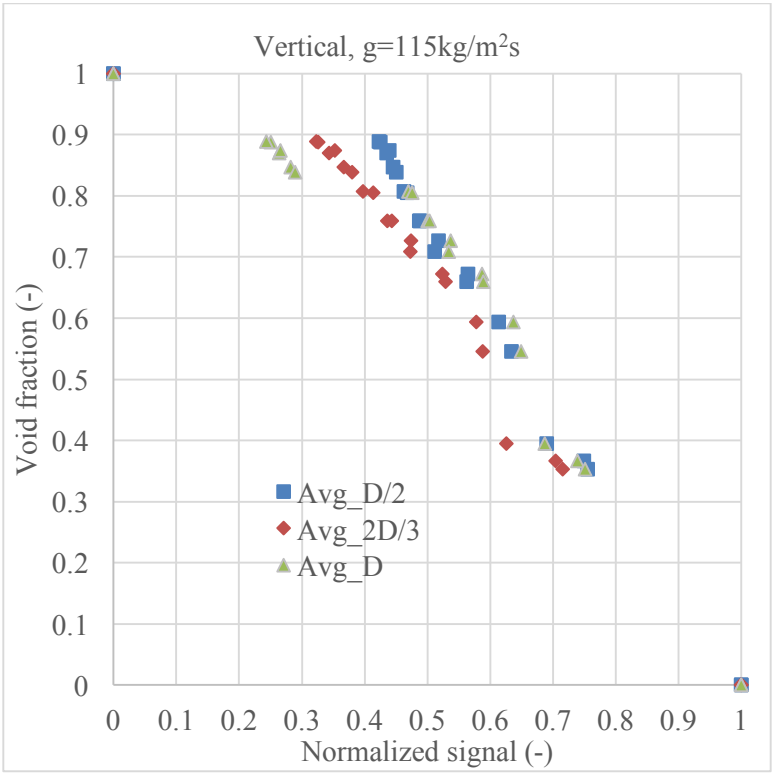

Figure 61 Signal comparison between electrodes widths: D/2, 2D/3, D (Vertical, g=115kg/m2s)

Conclusions

From the discussion above, both flow patterns characterization and void fraction measurement are compared among the series of signals from three pairs of electrodes with different axial lengths. The results show that for vertical configuration and this mass flux range, the signals don't depend on the axial length of electrodes. Hence, narrower electrodes can be used in the further studies to measure void fraction and characterize flow patterns.

4.6.3 Calibrated correlations for void fraction measurement in vertical tubes

Similar to the procedure of calibration of horizontal tubes, quick closing valves are used to get void fraction results. The calibration curve shows the relation between normalized capacitive signal and void fraction for upwards vertical flow in this mass flux range. Figure 62 shows the calibrated curve for vertical flows at low mass flux. Three flow pattern regions and three mass flux are included in this map. With this curve, sensors with the same configuration can be utilized to measure void fraction in upwards vertical flows with R134a in this mass flux range.

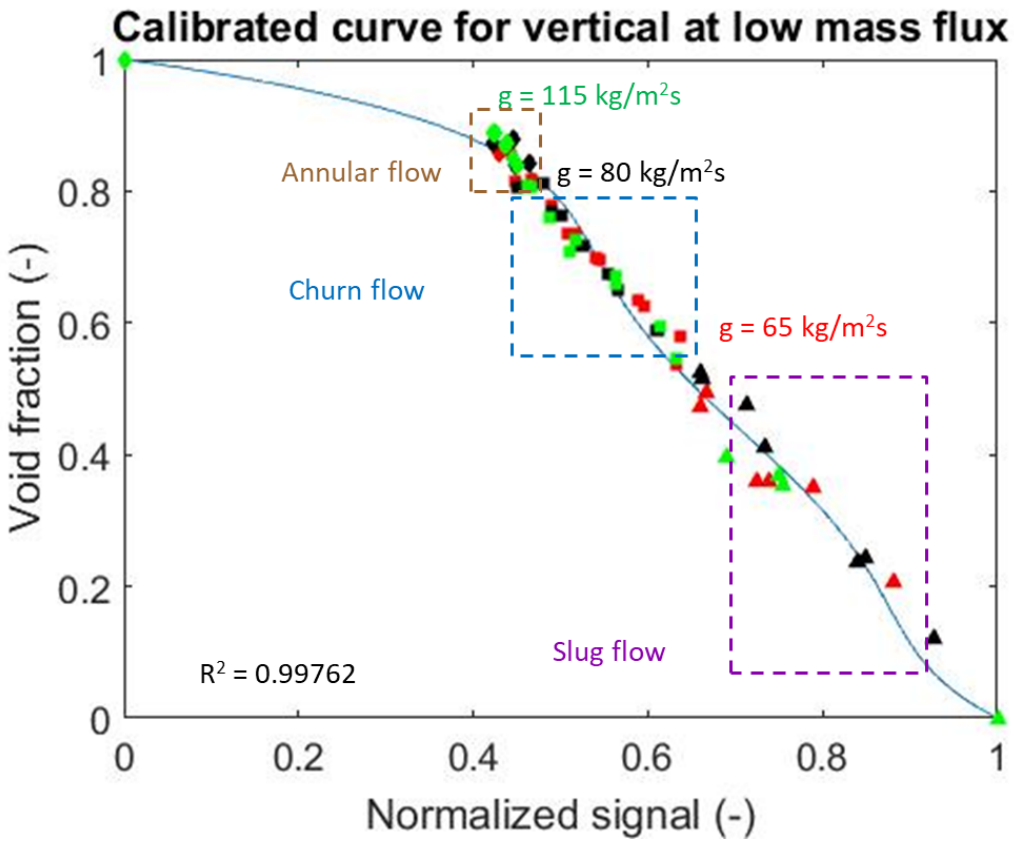

Figure 62 Calibrated curve for horizontal flow at low mass flux

CHAPTER 5 CONCLUSIONS

5.1 Summary

This research is divided into three parts. Void fraction and flow regimes in horizontal and vertical round tubes with R134a in adiabatic conditions and low mass flux is first studied. The second part is the design and building procedures of a capacitive sensor, which is to characterize flow patterns and measure void fraction. The last part is the results of characterizing flow patterns in the first part of this study with capacitive signals and a calibration procedure for void fraction measurement.

For characterizing the flow regime, visualization results are obtained from a high-speed camera. In the low mass flux range, three major flow patterns for horizontal flows and three for upwards vertical flows are observed. The criteria of different flow regimes transition are discussed in the research. For the horizontal flow regimes, the results are compared to the flow regime map from Wojtan-Ursenbacher-Thome [37] and have a relatively good agreement. Some modification of this map is proposed when applying it to predict flow patterns in horizontal flows with R134a in adiabatic conditions and low mass flux range. The void fraction results for both horizontal and vertical flows are presented and compared some widely used correlations. Woldesemayat and Ghajar [22] and Rouhani I [22, 32] correlations give pretty good void fraction predictions for test conditions in this study. For upwards vertical flows, void fraction correlations of Rouhani II [22, 32] and Dix [33] followed by Rouhani I [22, 32] are recommended. The results show that the tube orientation and mass flux have influence on the void fraction. For the same vapor quality, void fraction of higher mass flux flow is larger than that of smaller mass flux flow. Void fraction of upwards vertical flows is smaller than that of horizontal flows at the same vapor quality. Hence, utilizing proper correlations for different experimental conditions is necessary.

In Chapter 3, a capacitive sensor based on the sensor from Canière [45] is designed and further developed. To see the influence of axial length of electrodes and the possibility of utilizing shorter electrodes in applications with space limitation, three pairs with different axial lengths are set in a row. A commercially ready module is presented at the last of this chapter. FDC2214EVM is cheap and easy to use. It has some features like capability to measure small capacitive signals in pF range and good resolutions, which are suitable for this study.

Capacitive sensor signals analysis and sensor calibration for void fraction measurement is discussed in Chapter 4. The visualization and void fraction results are from Chapter 2. Normalized time-averaged signals and PDF are used to characterize flow patterns for horizontal and vertical flows. Due to the low mass flux range, few flow patterns are observed. If mass fluxes are beyond this range, more statistical analysis should be proposed to characterized flow patterns. Both flow pattern characterization and void fraction measurement are compared among three pairs of electrodes with different axial lengths. The results show that signals are independent on the axial length (D, 2D/3 and D/2) of electrodes. This ensure further studies to utilize shorter sensors in many applications, like to measure void fraction along the headers of microchannel heat exchangers. Finally, the calibrated curves of void fraction and normalized signal for both horizontal and vertical tubes are proposed. With these two calibrated cure, sensors with the same design can be utilized directly to measure void fraction in the smooth round tubes.

5.2 Future work

The capacitive sensor has been calibrated for measuring void fraction. Hence, this sensor can be applied to headers of microchannel heat exchangers to measure void fraction between tubes (Figure 63). Validation between the calibration results for smooth tubes and tubes with protrusions is going to be studied first. After validating this, the sensor is to be applied to horizontal and vertical headers. The diameter and length of headers may vary. In addition, void fraction of different shapes of headers, like D-shaped headers are going to be measured. Different refrigerants are also considered to be studied. The calibration procedure must be redone for refrigerant/header shape changes. Correlations of void fraction in headers is going to be proposed.

Figure 63 Headers and headers with capacitive sensors of microchannel heat exchangers

REFERENCES

1. Hurlburt, E. and T. Newell, *Optical measurement of liquid film thickness and wave velocity in liquid film flows.* Experiments in fluids, 1996. **21**(5): p. 357-362.
2. Wujek, S.S., P.S. Hrnjak, and C.J. Seeton. *Online Measurement Techniques for Determining Oil Circulation Rate*. in *ASME/JSME 2007 5th Joint Fluids Engineering Conference*. 2007. American Society of Mechanical Engineers.
3. Xu, J. and P. Hrnjak, *Quantification of flow and retention of oil in compressor discharge pipe.* International Journal of Refrigeration, 2017.
4. Li, J. and P. Hrnjak, *Visualization and quantification of separation of liquid-vapor two-phase flow in a vertical header at low inlet quality.* International Journal of Refrigeration, 2017.
5. Keska, J.K., M.D. Smith, and B.E. Williams, *Comparison study of a cluster of four dynamic flow pattern discrimination techniques for multi-phase flow.* Flow Measurement and Instrumentation, 1999. **10**(2): p. 65-77.
6. Keska, J.K. and B.E. Williams, *Experimental comparison of flow pattern detection techniques for air–water mixture flow.* Experimental Thermal and Fluid Science, 1999. **19**(1): p. 1-12.
7. Abouelwafa, M.S.A. and E.J.M. Kendall, *The use of capacitance sensors for phase percentage determination in multiphase pipelines.* IEEE Transactions on Instrumentation and measurement, 1980. **29**(1): p. 24-27.
8. Kendoush, A.A. and Z.A. Sarkis, *Improving the accuracy of the capacitance method for void fraction measurement.* Experimental thermal and fluid science, 1995. **11**(4): p. 321-326.
9. Ahmed, W.H. and B.I. Ismail, *Innovative techniques for two-phase flow measurements.* Recent Patents on Electrical & Electronic Engineering (Formerly Recent Patents on Electrical Engineering), 2008. **1**(1): p. 1-13.
10. Geraets, J. and J. Borst, *A capacitance sensor for two-phase void fraction measurement and flow pattern identification.* International Journal of Multiphase Flow, 1988. **14**(3): p. 305-320.
11. Elkow, K.J. and K.S. Rezkallah, *Void fraction measurements in gas-liquid flows using capacitance sensors.* Measurement Science and Technology, 1996. **7**(8): p. 1153.
12. Jaworek, A., A. Krupa, and M. Trela, *Capacitance sensor for void fraction measurement in water/steam flows.* Flow Measurement and Instrumentation, 2004. **15**(5): p. 317-324.
13. Jaworek, A. and A. Krupa, *Gas/liquid ratio measurements by rf resonance capacitance sensor.* Sensors and Actuators A: Physical, 2004. **113**(2): p. 133-139.
14. Jaworek, A. and A. Krupa, *Phase-shift detection for capacitance sensor measuring void fraction in two-phase flow.* Sensors and Actuators A: Physical, 2010. **160**(1): p. 78-86.
15. Canière, H., et al., *Horizontal two-phase flow characterization for small diameter tubes with a capacitance sensor.* Measurement Science and Technology, 2007. **18**(9): p. 2898.
16. Canière, H., et al., *Capacitance signal analysis of horizontal two-phase flow in a small diameter tube.* Experimental Thermal and Fluid Science, 2008. **32**(3): p. 892-904.

17. Canière, H., et al. *Capacitance Sensor Design For Refrigerant Two ‐ Phase Flow Characterization*. in *AIP Conference Proceedings*. 2007. AIP.

18. Thome, J.R., *Engineering data book III.* Wolverine Tube Inc, 2004. **2010**.

19. Kim, N.-H., D.-Y. Kim, and H.-W. Byun, *Effect of inlet configuration on the refrigerant distribution in a parallel flow minichannel heat exchanger.* International journal of refrigeration, 2011. **34**(5): p. 1209-1221.

20. Lee, J.K., *Two-phase flow behavior inside a header connected to multiple parallel channels.* Experimental Thermal and Fluid Science, 2009. **33**(2): p. 195-202.

21. Vijayan, P., et al., *An assessment of pressure drop and void fraction correlations with data from two-phase natural circulation loops.* Heat and Mass Transfer, 2000. **36**(6): p. 541-548.

22. Woldesemayat, M.A. and A.J. Ghajar, *Comparison of void fraction correlations for different flow patterns in horizontal and upward inclined pipes.* International Journal of Multiphase Flow, 2007. **33**(4): p. 347-370.

23. Butterworth, D., *A comparison of some void-fraction relationships for co-current gas-liquid flow.* International Journal of Multiphase Flow, 1975. **1**(6): p. 845-850.

24. Bankoff, S.G., *A variable density single-fluid model for two-phase flow with particular reference to steam-water flow.* Journal of Heat Transfer (US), 1960. **82**.

25. Hughmark, G.A., *Holdup in gas liquid flow.* Chem. Eng. Progr, 1962. **58**: p. 62-65.

26. Armand, A.A., *Resistance during the movement of a two-phase system in horizontal pipes*. 1959.

27. Massena, W., *Steam-water Pressure Drop and Critical Discharge Flow-A Digital Computer Program*. 1960, General Electric Co. Hanford Atomic Products Operation, Richland, Wash.

28. Zuber, N. and J.A. Findlay, *Average Volumetric Concentration in Two-Phase Flow Systems.* Journal of Heat Transfer, 1965. **87**(4): p. 453-468.

29. Ishii, M., *One-Dimensional Drift-Flux Model and Constitutive Equations for Relative Motion Between Phases in Various Two-Phase Flow Regimes, ANL Rep, 77, p. 40.* 1977.

30. Lockhart, R. and R. Martinelli, *Proposed correlation of data for isothermal two-phase, two-component flow in pipes.* Chem. Eng. Prog, 1949. **45**(1): p. 39-48.

31. Godbole, P.V., C.C. Tang, and A.J. Ghajar, *Comparison of void fraction correlations for different flow patterns in upward vertical two-phase flow.* Heat Transfer Engineering, 2011. **32**(10): p. 843-860.

32. Rouhani, S.Z. and E. Axelsson, *Calculation of void volume fraction in the subcooled and quality boiling regions.* International Journal of Heat and Mass Transfer, 1970. **13**(2): p. 383-393.

33. Dix, G.E., *Vapor void fractions for forced convection with subcooled boiling at low flow rates*. 1971: University of California, Berkeley.

34. Nicklin, D., *Two-phase flow in vertical tube.* Trans. Instn. Chem. Engrs., 1962. **40**: p. 61-68.

35. Klein., S.A., *EES – Engineering Equation Solver.*

36. Welford, A. and J. Brebner, *Introduction: an historical background sketch.* New York, 1980.

37. Wojtan, L., T. Ursenbacher, and J.R. Thome, *Investigation of flow boiling in horizontal tubes: Part I—A new diabatic two-phase flow pattern map.* International Journal of Heat and Mass Transfer, 2005. **48**(14): p. 2955-2969.

38. Canière, H., et al., *Probabilistic mapping of adiabatic horizontal two-phase flow by capacitance signal feature clustering.* International Journal of Multiphase Flow, 2009. **35**(7): p. 650-660.

39. Jassim, E.W., T. Newell, and J. Chato, *Probabilistic flow regime map modeling of two-phase flow*. 2006, Air Conditioning and Refrigeration Center. College of Engineering. University of Illinois at Urbana-Champaign.

40. Xiao, J. and P. Hrnjak, *A new flow regime map and void fraction model based on the flow characterization of condensation.* International Journal of Heat and Mass Transfer, 2017. **108**: p. 443-452.

41. Drahoš, J.í. and J. Čermák, *Diagnostics of gas—liquid flow patterns in chemical engineering systems.* Chemical Engineering and Processing: Process Intensification, 1989. **26**(2): p. 147-164.

42. De Kerpel, K., et al., *Flow regime based calibration of a capacitive void fraction sensor for small diameter tubes.* International Journal of Refrigeration, 2013. **36**(2): p. 390-401.

43. De Kerpel, K., et al., *Calibration of a capacitive void fraction sensor for small diameter tubes based on capacitive signal features.* Applied Thermal Engineering, 2014. **63**(1): p. 77-83.

44. Olivier, S.P., et al., *The influence of inclination angle on void fraction and heat transfer during condensation inside a smooth tube.* International Journal of Multiphase Flow, 2016. **80**: p. 1-14.

45. Canière, H., *Flow Pattern Mapping of Horizontal Evaporating Refrigerant Flow Based on Capacitive Void Fraction Measurements (Ph. D. thesis) Ghent University.* Ghent University, 2010.

46. Feja, S., *Measurement of electrical properties of refrigerants and refrigerant–oil mixtures.* International Journal of Refrigeration, 2012. **35**(5): p. 1367-1371.

47. Sedrez, P.C. and J.R. Barbosa, *Relative permittivity of mixtures of R-134a and R-1234yf and a polyol ester lubricating oil.* International Journal of Refrigeration, 2015. **49**(Supplement C): p. 141-150.

48. dos Reis, E. and L. Goldstein, *A procedure for correcting for the effect of fluid flow temperature variation on the response of capacitive void fraction meters.* Flow Measurement and Instrumentation, 2005. **16**(4): p. 267-274.

49. ASHRAE, *2013 ASHRAE Handbook - Fundamentals (I-P Edition)*. 2013, American Society of Heating, Refrigerating and Air-Conditioning Engineers, Inc.

50. Haynes, W.M., *CRC handbook of chemistry and physics*. 2014: CRC press.

51. Lowe, D. and K.S. Rezkallah, *A capacitance sensor for the characterization of microgravity two-phase liquid-gas flows.* Measurement Science and Technology, 1999. **10**(10): p. 965.

52. Shu, M.T., C.B. Weinberger, and Y.H. Lee, *A simple capacitance sensor for void fraction measurement in two-phase flow.* Industrial & Engineering Chemistry Fundamentals, 1982. **21**(2): p. 175-181.

53. *Rogers Corporation ULTRALAM® 3000 Liquid Crystalline Polymer Circuit Material Double-Clad Laminates data sheet*.

54. TI. *FDC2214 with Two Capacitive Sensors Evaluation Module*. [cited 2017 Oct. 28]; Available from: http://www.ti.com/tool/FDC2214EVM.

55. Olivier, S., et al., *Measured void fraction and heat transfer coefficients during condensation.* Sort, 2015. **100**: p. 250.

APPENDIX A ORIGINAL DATA

Table 9 G=40kg/m^{2}s, horizontal, vapor quality vs. void fraction

x	α	x	α
0	0	0	0
0.06	0.5078	0.06	0.2538
0.1	0.5538	0.1	0.5352
0.2	0.6158	0.19	0.6391
0.3	0.692	0.3	0.6892
0.4	0.7512	0.4	0.7343
0.5	0.7813	0.5	0.7813
0.6	0.809	0.6	0.8105
0.7	0.8444	0.71	0.8349
0.84	0.8742	0.8	0.8706
0.9	0.9043	0.89	0.8972
1	1	1	1

Table 10 G=80kg/m^{2}s, horizontal, vapor quality vs. void fraction

x	α	x	α	x	α
0	0	0	0	0	0
0.11	0.4033	0.05	0.4812	0.06	0.4948
0.18	0.6208	0.1	0.5573	0.11	0.5659
0.3	0.7273	0.2	0.6609	0.22	0.6777
0.39	0.7653	0.3	0.7367	0.3	0.7296
0.51	0.8075	0.4	0.783	0.41	0.783
0.61	0.8539	0.5	0.817	0.5	0.8185
0.7	0.8804	0.6	0.8529	0.6	0.8489
0.8	0.9052	0.7	0.8822	0.7	0.8808
0.9	0.9305	0.8	0.9043	0.79	0.9008
1	1	0.9	0.9273	0.9	0.9257
0.05	0.5042	1	1	1	1

Table 11 G=115kg/m^{2}s, horizontal, vapor quality vs. void fraction

x	α
0	0
0.05	0.5078
0.1	0.5952
0.2	0.6795
0.3	0.7406
0.4	0.8105
0.5	0.8459
0.6	0.8711
0.7	0.8916
0.8	0.9167
0.9	0.9326
1	1

Table 12 G=65kg/m^{2}s, vertical, vapor quality vs. void fraction

x	α	x	α
0	0	0	0
0.05	0.3491	0.05	0.2064
0.1	0.3589	0.1	0.359
0.2	0.4709	0.2	0.4938
0.3	0.5783	0.3	0.5376
0.4	0.6269	0.4	0.6345
0.51	0.6981	0.5	0.6956
0.6	0.7363	0.6	0.7363
0.7	0.777	0.7	0.7795
0.79	0.8151	0.79	0.8177
0.9	0.8608	0.9	0.8583
1	1	1	1

Table 13 G=80kg/m^{2}s, vertical, vapor quality vs. void fraction

x	α	x	α
0	0	0	0
0.05	0.237	0.05	0.2423
0.1	0.4761	0.1	0.4128
0.2	0.5246	0.2	0.5145
0.3	0.5886	0.3	0.5887
0.4	0.6752	0.4	0.6489
0.5	0.7185	0.5	0.7184
0.6	0.7685	0.6	0.7634
0.7	0.8049	0.7	0.8117
0.8	0.8405	0.8	0.8431
0.9	0.8735	0.9	0.8786
1	1	1	1

Table 14 G=115kg/m^{2}s, vertical, vapor quality vs. void fraction

x	α	x	α
0	0	0	0
0.05	0.367	0.05	0.3526
0.1	0.3466	0.1	0.3949
0.19	0.5453	0.2	0.5938
0.3	0.6719	0.3	0.6598
0.4	0.7269	0.39	0.709
0.5	0.7591	0.5	0.7591
0.6	0.8075	0.6	0.8049
0.7	0.8473	0.7	0.838
0.8	0.8703	0.8	0.8736
0.89	0.8872	0.9	0.8888
1	1	1	1

Table 15 Void fraction vs. normalized signal of electrodes with different lengths, horizontal, G=40kg/m^{2}s

Quality (x)	Void fraction	Avg_D/2	Avg_2D/3	Avg_D
0	0	1	1	1
0.1	0.5543	0.644438894	0.66323178	0.693442513
0.2	0.6163	0.617165855	0.627804219	0.657149774
0.3	0.692	0.584196358	0.559906204	0.588203065
0.4	0.7512	0.575412142	0.547134659	0.560786156
0.5	0.7812	0.541284382	0.511416215	0.531693962
0.6	0.8089	0.521560425	0.48794442	0.514487507
0.7	0.8442	0.48780599	0.452412303	0.485791952
0.84	0.8739	0.437899367	0.393432363	0.440013022
0.9	0.904	0.233789322	0.335254254	0.153284222
1	1	0	0	0
0	0	1	1	1
0.06	0.2641	0.711993237	0.709764711	0.757172918
0.1	0.5358	0.670613607	0.691887178	0.7260223
0.19	0.6394	0.613554955	0.613401531	0.643308096
0.3	0.6894	0.589961419	0.561876626	0.596054586
0.4	0.7344	0.568542748	0.527506946	0.555059875

0.5	0.7812	0.523886925	0.485938487	0.51794023
0.6	0.8104	0.494164684	0.459068984	0.497243819
0.71	0.8348	0.464397193	0.423431431	0.470303755
0.8	0.8704	0.420013842	0.367363959	0.391079844
0.89	0.8969	0.338985439	0.32213171	0.398157554
1	1	0	0	0

Table 16 Void fraction vs. normalized signal of electrodes with different lengths, horizontal, G=80kg/m^{2}s

Quality (x)	Void fraction	Avg_D/2	Avg_2D/3	Avg_D
0	0	1	1	1
0.05	0.4909	0.754368311	0.74774045	0.679611383
0.1	0.5577	0.661058651	0.633015826	0.573379236
0.2	0.6611	0.613352578	0.56410077	0.530973382
0.3	0.7368	0.520851326	0.484863294	0.344204008
0.4	0.783	0.469362018	0.440188152	0.2720155
0.5	0.8169	0.428548091	0.405438725	0.238240407
0.6	0.8528	0.39157481	0.372474364	0.211351354
0.7	0.882	0.360811179	0.345105009	0.187930631
0.8	0.9041	0.315716112	0.3218782	0.169996421
0.9	0.9272	0.24410949	0.282565563	0.153553266
1	1	0	0	0
0	0	1	1	1
0.11	0.5662	0.695957245	0.664764559	0.681738524
0.22	0.6777	0.617212249	0.560899971	0.613026283
0.3	0.7296	0.543554735	0.494851729	0.552300625
0.41	0.783	0.484156765	0.444720538	0.495864204

0.5	0.8184	0.431006608	0.398429382	0.452041593
0.6	0.8488	0.420877414	0.384060819	0.439847585
0.7	0.8807	0.39192177	0.355335249	0.415957634
0.79	0.9006	0.365759804	0.321985647	0.391430052
0.9	0.9256	0.346284294	0.291809796	0.371356609
1	1	0	0	0

Table 17 Void fraction vs. normalized signal of electrodes with different lengths, horizontal, G=115kg/m^{2}s

Quality (x)	Void fraction	Avg_D/2	Avg_2D/3	Avg_D
0	0	1	1	1
0.05	0.5171	0.768291316	0.73656603	0.747098449
0.1	0.5954	0.739019628	0.680467434	0.718418991
0.2	0.6796	0.627707304	0.57056748	0.619700703
0.3	0.7406	0.566606279	0.517531221	0.550988409
0.4	0.8104	0.538172337	0.490923796	0.525026135
0.5	0.8457	0.503875623	0.456476329	0.492512898
0.6	0.8711	0.4827749	0.431829171	0.470863976
0.7	0.8914	0.463515349	0.406997528	0.450373607
0.8	0.9164	0.444857702	0.379334354	0.43057592
0.9	0.9323	0.435513259	0.367275662	0.422161761
1	1	0	0	0

Table 18 Void fraction vs. normalized signal of electrodes with different lengths, vertical, G=65kg/m^{2}s

Quality (x)	Void fraction	Avg_D/2	Avg_2D/3	Avg_D
0	0	1	1	1
0.05	0.3492	0.790018148	0.733792449	0.762753895
0.1	0.359	0.724014339	0.664588776	0.700133056
0.2	0.471	0.660100316	0.580455155	0.652153135
0.3	0.5783	0.636222992	0.566091709	0.640076989
0.4	0.6269	0.59460267	0.52149932	0.604940464
0.51	0.6981	0.540078452	0.470674322	0.559531709
0.6	0.7363	0.50843573	0.44288289	0.523226971
0.7	0.777	0.490391296	0.431949136	0.509140803
0.79	0.8151	0.449221441	0.401344109	0.482981613
0.9	0.8608	0.441215717	0.354531312	0.279598629
1	1	0	0	0
0	0	1	1	1
0.05	0.2066	0.881085793	0.838003896	0.864485907
0.1	0.359	0.739000041	0.678952699	0.710860917
0.2	0.4938	0.666314077	0.58679704	0.654418138
0.3	0.5376	0.633524443	0.561482674	0.637200348

0.4	0.6345	0.588191992	0.528184082	0.603758091
0.5	0.6956	0.545369712	0.490460031	0.567927367
0.6	0.7363	0.516966699	0.454034913	0.534667756
0.7	0.7795	0.489026312	0.420800557	0.502683345
0.79	0.8177	0.465976589	0.399535437	0.481814924
0.9	0.8583	0.429162356	0.340371023	0.275316594
1	1	0	0	0

Table 19 Void fraction vs. normalized signal of electrodes with different lengths, vertical, G=85kg/m^{2}s

Quality (x)	Void fraction	Avg_D/2	Avg_2D/3	Avg_D
0	0	1	1	1
0.05	0.237	0.840876382	0.797838316	0.824742521
0.1	0.4761	0.71415276	0.659019965	0.694286929
0.2	0.5246	0.661044123	0.595972974	0.660429336
0.3	0.5886	0.608301555	0.565724256	0.624690409
0.4	0.6752	0.555133976	0.505070806	0.574667282
0.5	0.7185	0.521930848	0.49004238	0.545397948
0.6	0.7685	0.490500981	0.441444379	0.512220414
0.7	0.8049	0.451200379	0.401725554	0.480203097
0.8	0.8405	0.449075246	0.386087398	0.458510263
0.9	0.8735	0.422805026	0.332020175	0.185324719
1	1	0	0	0
0	0	1	1	1
	0.1213	0.927745097	0.905677905	0.92455817
0.05	0.2425	0.847944145	0.804185097	0.827907549
0.1	0.4128	0.732879405	0.678755698	0.7109791
0.2	0.5145	0.662831169	0.596007282	0.657904977

0.3	0.5887	0.611631142	0.570399738	0.624501374
0.4	0.6489	0.564882063	0.520648248	0.584821765
0.5	0.7184	0.526367561	0.469120026	0.549319084
0.6	0.7634	0.501032309	0.445508705	0.520666876
0.7	0.8117	0.479478609	0.407497986	0.484309878
0.8	0.8431	0.465218467	0.388937521	0.464945622
0.9	0.8786	0.445516392	0.343919689	0.268163551
1	1	0	0	0

Table 20 Void fraction vs. normalized signal of electrodes with different lengths, vertical, G=115kg/m^{2}s

Quality (x)	Void fraction	Avg_D/2	Avg_2D/3	Avg_D
0	0	1	1	1
0.05	0.367	0.749264659	0.704729153	0.738548687
0.2	0.5453	0.633448496	0.58777385	0.648845151
0.3	0.6719	0.564225183	0.524158301	0.586624371
0.4	0.7269	0.517771965	0.473318619	0.536613654
0.5	0.7591	0.488300307	0.435679611	0.500148194
0.6	0.8075	0.462696171	0.396945277	0.469920345
0.7	0.8473	0.445404218	0.367044012	0.282218349
0.8	0.8703	0.435492483	0.343314805	0.263318899
0.9	0.8872	0.424782271	0.325465837	0.250563113
1	1	0	0	0
0	0	1	1	1
0.05	0.3526	0.755272773	0.715114477	0.750939982
0.1	0.3949	0.689856174	0.625305256	0.687210803
0.2	0.5938	0.613908787	0.578307182	0.636563325
0.3	0.6598	0.56227783	0.529311023	0.589162556
0.39	0.709	0.51107629	0.47295918	0.534011959

0.5	0.7591	0.487357351	0.442808514	0.502961716
0.6	0.8049	0.467462389	0.414019922	0.475716093
0.7	0.838	0.449891439	0.37969856	0.289069764
0.8	0.8736	0.438989849	0.352262642	0.265306665
0.9	0.8888	0.422581568	0.322501162	0.243178672
1	1	0	0	0